Non-uniform Resolution and Partial Volume Recovery in Tomographic Image Reconstruction Methods

Munir Ahmad

(June 2009)

Department of Medical Physics and Bioengineering
University College London (UCL), UK

Supervisor
Prof. Andrew Todd-Pokropek

Submitted in partial fulfillment of the requirements of PhD

Declaration by Candidate

I, Munir Ahmad, confirm that work presented in this thesis is my own. Where information has been derived from other sources, I confirm that this has been indicated in the thesis and that it has not been submitted anywhere for any award.

Signature: …………………………………..
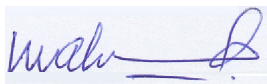
Date: …………………………………….

© **Munir Ahmad**

Abstract

Acquired data in tomographic imaging systems are subject to physical or detector based image degrading effects. These effects need to be considered and modeled in order to optimize resolution recovery. However, accurate modeling of the physics of data and acquisition processes still lead to an ill-posed reconstruction problem, because real data is incomplete and noisy. Real images are always a compromise between resolution and noise; therefore, noise processes also need to be fully considered for optimum bias variance trade off. Image degrading effects and noise are generally modeled in the reconstruction methods, while, statistical iterative methods can better model these effects, with noise processes, as compared to the analytical methods. Regularization is used to condition the problem and explicit regularization methods are considered better to model various noise processes with an extended control over the reconstructed image quality. Emission physics through object distribution properties are modeled in form of a prior function. Smoothing and edge-preserving priors have been investigated in detail and it has been shown that smoothing priors over-smooth images in high count areas and result in spatially non-uniform and nonlinear resolution response. Uniform resolution response is desirable for image comparison and other image processing tasks, such as segmentation and registration. This work proposes methods, based on MRPs in MAP estimators, to obtain images with almost uniform and linear resolution characteristics, using nonlinearity of MRPs as a correction tool. Results indicate that MRPs perform better in terms of response linearity, spatial uniformity and parameter sensitivity, as compared to QPs and TV priors. Hybrid priors, comprised of MRPs and QPs, have been developed and analyzed for their activity recovery performance in two popular PVC methods and for an analysis of list-mode data reconstruction methods showing that MPRs perform better than QPs in different situations.

Table of Contents

Acknowledgement

Dedication

I dedicate my work to my family, my supervisor and my parents. Without their help I might have not been able to complete this work.

Table of Figures

List of Tables

List of Common Acronyms

ACF	Attenuation Correction Factors	28
ART	Algebraic Reconstruction Tomography	18
BPF	Back-projection Filtering	40
CBP	Convolution Back-projection	18
CG	Conjugate Gradient	45
CPs	Combined Priors	74
DRF	Detector Response Function	26
ECT	Emission Computed Tomography	24
FBP	Filtered Back-projection	18
FOV	Field of View	61
DFR	Direct Fourier Reconstruction	18
FST	Fourier Slice Theorem	41
FT	Fourier Transform	41
FWHM	Full Width at Half Maximum	31
GRF	Gibbs Random Fields	54
GTM	Geometric Transfer Matrix	78
HRRT	High Resolution Research Tomograph	135
ICA	Iterated Coordinate Ascent	71
IFT	Inverse Fourier Transform	41
IR	Iterative Reconstruction	18
IRF	Impulse Response Function	59
IRT	Inverse Radon Transform	40
KBL	Kullback Lieber	44
LIR	Local Impulse Response	21
LIR-CRC	Local Impulse Response -	75
LLIR	Linearized Local Impulse Response	60
LLPR	Linearized Local Perturbation Response	75
LMEM	List Mode Expectation Maximization	139
LM-MAP	List Mode Maximum-a-Posterior	142
LOR	Line of Response	24

LSQ	Least Square	44
MAE	Mean Absolution Error	89
MAP	Maximum-a-Posterior	19
MC	Monte-Carlo	36
ML	Maximum Likelihood	46
MLEM	Maximum Likelihood Expectation Maximization	46
ModMRPs	Modified Median Root Priors	74
ModQPs	Modified Quadratic Priors	100
MRF	Markov Random Fields	54
MRI	Magnetic Resonance Imaging	78
MRPs	Median Root Priors	20
MSE	Mean Square Error	89
NonQPs	Non-quadratic Penalties	63
OSL	One Step Late	53
PCCG	Pre-Conditioned Conjugate Gradient	70
PET	Positron Emission Tomography	18
PLEM	Penalized Likelihood Expectation Maximization	19
PMT	Photomultiplier Tubes	25
PSF	Point Spread Function	77
PVC	Partial Volume Correction	76
PVE	Partial Volume Error	20
QPs	Quadratic Priors	19
RSF	Regional Spread Function	121
RT	Radon Transform	33
SPECT	Single Positron Emission Computed Tomography	18
SVD	Single Value Decomposition	38
TV	Total Variation	20
WLSQ	Weighted Least Square	129

List of Common Variables

$\mu(x,y)$	Attenuation coefficient at spatial location (x,y)	28
$f(x,y)$	Object distribution at spatial location (x,y)	28
P_{line}	Survival probability of photons along the line	28
$p_\theta(r)$	Projection at angle θ as a function of radial distance r	33
$\delta()$	Dirac Delta function	
$x,y,b,\theta,x_j,y_i,b_i,\theta_i,x^k$	Vectors x,y,b and angle ϑ with their $j-th$ element and vector x at $k-th$ iteration.	26-35
$H,H_{geom},H^t,h_{ij},H_{ij}$	System matrices with transpose and $ij-th$ element.	35
∇,Δ	Gradient and differential derivatives	46
$L_y^Y(f),p_Y(y\|f)$	Likelihood functions of random variable Y with its realization y and given object vector f. Probability of y given vector f.	46
$E[]$	Expectation operator	46
$\mathbb{R}^n$	n dimensional real numbers space	33
$\lambda,\phi(f)$	Relaxation parameter and energy function.	48
$\bar{Y}$	Mean of a random vector Y	52
l^j	Local impulse response at location of $j-th$ pixel.	61
$F(u,v),P_\theta(r)$	Fourier transforms of functions $f(x,y)$ and $p_\theta(r)$	42

CHAPTER 1

Introduction

Imaging systems are compared to each other by the quality of images they produce. Resolution is one of the common measures of image quality and expresses imaging system's capability to resolve two smallest spatial features. Resolution properties of emission computed tomographic (ECT) imaging systems, such as PET/SPECT, are affected by numerous image-degrading effects, such as non-uniform attenuation, scatter and crystal penetration effects etc. They also include effects originating from general imaging physics to the effects produced by particular image estimator used and by the properties of the object being imaged. These effects force the data from these systems to deviate from simple line integral model, which is generally considered to be an ideal data model. It could have been much easier to specify resolution properties of the reconstructed images, if these effects were spatially-uniform, however, an added complexity is due to their spatial variations. Even, intrinsically space-invariant systems produce images with space-variant characteristics due to these intricacies. All these effects accumulatively degrade the final image quality and induce spatial variance noise and resolution properties.

To optimize resolution recovery, all the above effects need to be addressed by the system and reconstruction model which is commonly applied through the reconstruction method. Therefore, reconstruction method used is very important in deciding for the quality of the reconstructed images. Different reconstruction methods have varying abilities to model these effects. For example, analytical reconstruction methods, such as filtered back-projection (FBP), direct Fourier reconstruction (DFR) or convolution back-projection (CBP), have limited ability in this regard. These methods are generally based on inversion of an analytical formula to describe forward projected data, which is ideally considered to follow a line integral model and ignore any underlying noise processes, hence, their results suffer from severe quantification errors. Simple iterative methods, such as algebraic reconstruction techniques (ART), try to solve the line integral problem, numerically, and their images bear almost same characteristics as of analytical methods. Methods based on data likelihood approach try to model data noise and can easily include

modeling of the system, however, even with accurate modeling reconstruction problem still becomes an ill-posed inverse problem and the resultant images suffer from reconstruction based noise. These methods try to find an image, best fitted to the data information only, which is always noisy; hence, solution image is noisy, though with better quality as compared to the analytical reconstruction methods.

Regularization, which simply means to constrain the solution image by imposing further conditions based on object properties or otherwise, is used to combat this ill-conditioning of the reconstruction problem. Regularized statistical reconstruction methods, such as Penalized-Likelihood (PLEM) or MAP methods, use information based on object properties in addition to the information available in the data, to compensate for noise and better condition the problem. This object *priori* information is introduced in form of a probability distribution function or regularization function and gives user an extra control over quality of the final image. Object properties are based on the images derived from Markov Random Field (MRF) images, which emphasizes on local image smoothness.

Several local regularization priors have been introduced in the literature and smoothness priors, in the form of a Gibbs distribution function of pair wise pixel differences, have been applied extensively. Smoothness priors, most commonly QPs, smooth out salient features of the images and bear anisotropic smoothing behavior. This behavior leads images with non-uniform resolution characteristics, which ultimately makes image comparison or their registration or segmentation process, a complex task. So, inter-modality image comparison becomes problematic. With these priors, reconstructed images consequently may contain deformed regions, where circles appear as ellipses, and will lead to an erroneous diagnosis with hampered quantification. Also, regions appear to have lesser activity due to spill over from high count regions and produce errors in the calculation of estimated tumor volumes. Hence, images with uniform resolution properties across the whole span of the reconstructed images are desirable. Several quadratic and non-quadratic smoothness priors have been introduce for better quality and lesser noisy images as compared to the simple MLEM methods; however, they produce images with space-variant resolution properties and induce asymmetric system responses. It has been shown that these priors have space-variant smoothing characteristics, controlled by shift-variant localized image pixel variance and other physical factors, which are heavier in high activity regions inside the object. These priors work on the concept of local image smoothness and penalize higher pixel differences with stronger force and over-smooth the edges. Non-quadratic prior functions have been proposed for edge preservation, however, with an expense of extra empirical parameters to be tuned and an artifact of induced patchy areas.

Another class of priors, known as edge preserving priors, with two very popular choices of Total Variation (TV) regularization priors and Median Root Priors (MRPs), have been investigated. TV priors work as the irregularity measure of the image, whereas, MRPs try to preserve local mono-tonicity. Both of these concepts are not too different and these priors preserve edges and smooth regions almost equivalently. Unfortunately, these priors do not have their analytical derivatives defined and are not very attractive mathematically, however, their empirical derivatives have been proposed with acceptable results. So far, their use has only been restricted to image reconstruction methods and no attempt has yet been made, as of our knowledge, to develop, analyze and use MRPs to design prior functions in order to achieve uniform reconstructed image resolution. It is very important to have some sort of quantitative measure, for this type of analysis, and comparison of resolution properties of different methods. A simple way is to use Brute force method (defined in the text in Chapter 4) or another option is to use an analytical function, known as local impulse response (LIR), which was initially developed for PLEM methods. These provide us with nice tools to compare system response of some estimator in a local neighborhood of an object of interest. LIR can also help use to design some user defined prior functions in order to obtain predefined desired system responses.

In this work, motivated by the above discussion, we propose a prior design based on MRPs for the compensation of non-uniform reconstructed resolution with MAP estimators. This design is based on both, the nonlinearity of MRPs and certainty based correction method developed for QPs. We comprehensively analyzed resolution characteristics of our proposed priors with a comparison to the results of standard quadratic priors by evaluating impulse responses inside the target object. We also developed a new class of hybrid priors, based on both QPs and MRPs, and have shown that their response is more controllable in sense of uniform reconstructed resolution. An implementation of our priors with real SPECT data has also been presented.

Partial Volume Effect (PVE) is a direct consequence of the limited resolution of imaging systems; hence, any proposed method for the compensation of non-uniform spatial resolution should be analyzed for its activity recovery performance. An implementation of our proposed methods has been presented in two very popular partial volume correction methods to analyze their activity recovery performance. Data are binned or squeezed both in radial and angular directions, in bin mode or histogram data acquisition mode, which leads to a loss of accuracy or at least redundancy. Different attributes related to each event are saved in a long list, in list-mode data acquisition, and provide us a way to exploit full data accuracy. No such effort to use LIR in list-mode reconstruction methods has yet been made, as of our knowledge, to evaluate their resolution characteristics. We have presented

an implementation of our proposed priors in list-mode reconstruction methods with an evaluation of LIR function, appropriately modified for list-mode data. In brief, we may summarize a following hypothesis for our research with aims and objects given;

Hypothesis: Tomographic imaging systems have space-variant response due to spatially varying acquisition and detection physics and produce images with non-uniform resolution characteristics, which can be corrected by modelling emission object constraints in form of a properly designed prior distribution function in MAP estimators, with better activity recovery performance at the same time.

Aims and Objectives: With the above hypothesis given, research work was carried out with the following aims and objectives in mind:

> ➤ *Evaluation of spatially variant system response with different reconstruction methods. These include MAP estimation methods, with popular smoothing priors and further to develop prior functions which may provide better image quality, in the sense of reconstructed resolution, and activity recovery performance [P1, P4, P5].*
>
> ➤ *To analyse comprehensively resolution characteristics of the proposed prior functions, with their implementation in LIR function, and to find some modified prior functions to compensate for spatially non-uniform resolution properties of the reconstructed images. [P4].*
>
> ➤ *Compare resolution properties of proposed priors with standard QPs and TV [P6, P5]. Evaluate activity recovery performance of our developed priors using some robust methods for partial volume correction and compare their performance with that of the standard QPs [P2, P7, P8].*
>
> ➤ *Evaluate resolution characteristics of our proposed prior distribution functions in list-most regularized reconstruction methods to look for any further benefit list-mode data may provide [P1] and to evaluate noise performance as compared to the standard QPs [P3].*

Chapter 2, briefly discusses emission computed tomographic imaging physics and reconstruction methods including a basic discussion of some physical and detector dependent effects which degrade quality of the reconstructed images. We have mentioned some of the basic techniques researchers have previously used to compensate for these effects and to improve resolution and noise characteristics in order to improve quality of

these images. We have briefly given a description of Partial Volume Error (PVE) with a brief derivation of Local Impulse Response (LIR) expression which we have extensively used in our work.

Chapter 3, reviews previous literature, while discussing different reconstruction techniques, image degrading effects, and system models used in MAP and PLEM reconstruction methods, with QPs, MRPs and TV. We have also reviewed different partial volume correction methods used, some standard list-mode reconstruction methods and noise analysis techniques while putting our work in the context of previous efforts, wherever possible.

Chapter 4, describes some experimental methods and setups and designs for the comparison of different algorithms used to improve reconstructed image resolution. We have also proposed some new MRPs based prior functions for the compensation of non-uniform resolution characteristics of the reconstructed images. An implementation of our priors with real data has been presented, too.

Chapter 5, describes an implementation and evaluation of partial volume correction methods including a comparison of our proposed priors with QPs.

Chapter 6, details an implementation of a modified linear impulse response function for list-mode reconstruction methods. We presented results for our proposed priors included in regularized list-mode reconstruction methods, in the context of non-uniform resolution and its compensation methods.

Chapter 7, concludes our results and analyses and proposes few possible extensions of our work as future work. After a list of references we have included copies of some important code used to work our analysis in appendix A.

It is worth mentioning that a vital motivation for this work was the need to develop methods for accurate quantification of reconstructed images for diagnosis and therapy purposes, for example in case of Thyroid diseases.

CHAPTER 2

Background

This work has its overall contribution towards the field of tomographic image reconstruction and general imaging problems, however, its main application relates to an appetite of the medical diagnostic community for better image quality, especially, resolution and signal-to-noise ratio. Emission imaging has lower resolution capabilities, as compared to the transmission imaging, hence, specific background material has been discussed related to emission computed tomography (ECT), though, transmission tomography has also been discussed, wherever feasible.

2.1 Emission Computed Tomography (ECT)

ECT is used in medicine to image functional information about physiological processes in the human body. A small amount of radioisotope is introduced into the body, while attached to some pharmaceutical selective for specific organ via injection or inhalation, and emission data is acquired around the body. Images of the radiotracer distribution are reconstructed, from this data later on, to find concentration of the radiotracer in various parts of body. These images are considered very helpful for medical diagnostics [1;2].

Two most commonly used ECT modalities are Positron Emission Tomography (PET) and Single Photon Emission Computed Tomography (SPECT). Positron emitting radioisotopes, such as F^{18} or C^{11}, are used in PET to generate positrons which travel a short distance before annihilation with an electron, producing two almost collinear and oppositely traveling gamma ray photons. This pair of oppositely moving photons is detected in some surrounding pair of detectors emanating an event along the line joining these two detectors, or the so called line-of-response (LOR), giving an estimate that emission has taken place somewhere along this line [2]. An event will be added, as a coincident event, to the list of detected events, if it falls within a predefined short (~12-20 ns) coincident timing window [2;3]. After collection of data for a large enough number of

LORs, at various angles and radial positions, an image reconstruction algorithm can be applied later on to get an estimated image of the radiotracer distribution.

(a) SPECT Tomography	(b) PET Tomography
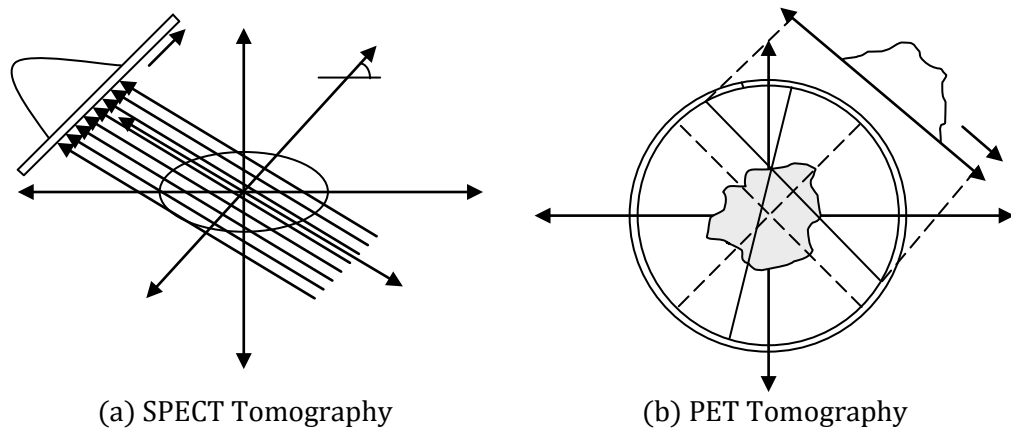
Figure 2.1: Idealized Computed Tomography. (a) In SPECT imaging system, detector rotates around the object and collects emission data for all radial samples. Shown above is a single view taken at a particular angle with x-axis. (b) In PET system, a single view is shown at a specified angle form x-axis. Data for all angles is collected at the same time in PET.

A single gamma ray photon is used to account for an event in SPECT imaging, detected by a single large rectangular crystal scintillation detector (Anger camera configuration) [3]. A collimator is placed in front of the scintillation detector to obtain directional information, so that only gamma rays entering from some known angles can reach the detector. Parallel-hole collimators are the most commonly used collimators, along with other types such as converging, diverging or pinhole collimators. Data for a whole range of angles is collected by rotating a detector around the object to be imaged. In scintillation detectors, scintillating material (for example, Thallium doped Sodium Iodide, NaI(Th)) is optically coupled to a number of Photomultiplier Tubes (PMTs). Scintillation material produces a burst of light-photons when a gamma ray interacts inside it. These light photons are converted into electrical signals by the PMTs. Detection and processing for localization of this signal is achieved by electronic arithmetic circuitry to estimate the LOR along which that gamma ray was traveling [2;4;5].

A simplest detection system may comprise of a small single scintillation detector coupled with a PMT, however, in practice more complex configurations are used. Detector blocks in form of a ring are used in PET system, whereas, Anger camera configuration is used for SPECT scanners with a large detector coupled to a number of PMTs as, shown in Figure 2.2. A rectangular bundle of crystals is coupled optically to four PMTs, in a block detector, in a unique configuration in PET so that event localization can be performed on the basis of signal magnitudes coming out of all four PMTs, coupled to the block as shown in

Figure 2.3. A similar manipulation of the output signal from PMTs in Anger Camera SPECT system is used to define location of the scintillation event inside the crystal.

(a) Ring type PET Detector   (b) SPECT Detector
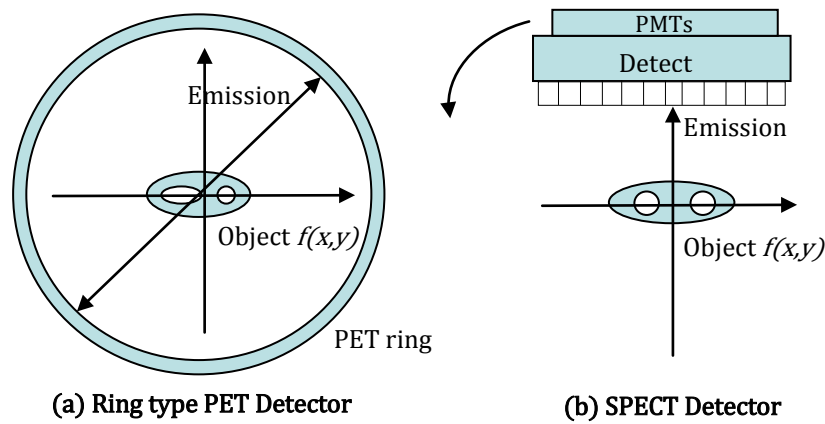
Figure 2.2: PET and SPECT detector configurations, (a) shows a circular ring type PET detector where all angular samples are collected simultaneously and (b) shows an Anger type SPECT detector configuration where detector rotates around the object to get data for different angular samples.

2.2   Image quality degradations

Resolution degradations might have not been an important research issue, if it were possible to localize the event, exactly. In practice, we make a number of assumptions about physical processes involved and the system used. Even scintillation process has a blur due to more than one scintillation interactions inside the crystal for a single decaying gamma ray. There are several other physical effects which complicate localization of events and, hence, degrade image quality [6-8].

2.2.1 Detector Response Effects (DRFs)

Inside a block detector PET system, a single finite sized crystal detector has limited detection accuracy, which is only up to the size of that crystal. Detection efficiency of a single detector depends on its spatial position inside the main detector block and is non-uniform even within that detector. In SPECT Anger camera configuration, localization of an event has a spatial distribution limited by the number of light photons emitted due to the statistical nature of the emission and transmission processes [9;10].

These effects may be summed up as Detector Response Function (DRF) and effectively define sensitivity pattern of the detector system. These sensitivities are non-uniform, even for each individual detector and drifts in PMT response over time is another cause for these

non-uniformities. A periodical normalization scan is necessary to make adjustments for these shifts [11-14]. Variations in detector response also depend on the position of the detector in a ring type PET scanner as all detectors are not necessarily parallel to each other and produce a positional dependency in the detector response.
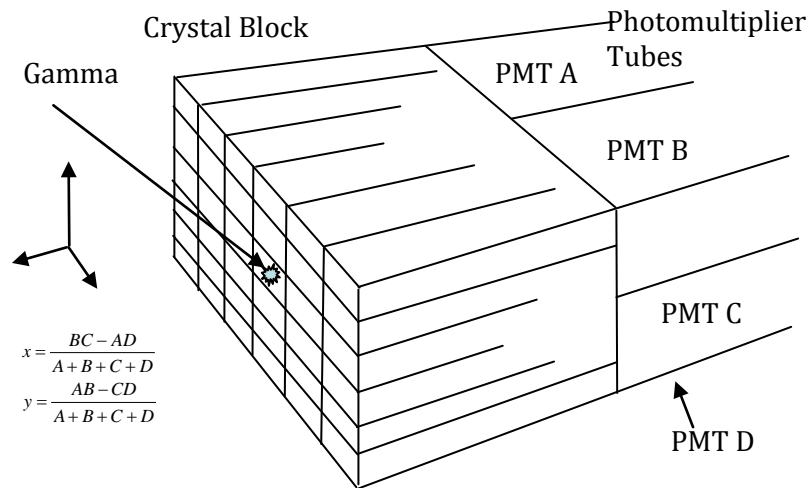
Figure 2.3: Block detector configuration used in PET systems. It also presents how the emission location is calculated based on the strength of the signal from different PMTs.

Depth of gamma ray interaction inside a crystal, as shown in Figure 2.4, also makes positional localization of the scintillation event more ambiguous, which is summed up by another ambiguity in the z-direction for oblique detectors because localization is only performed in a single plane [11]. In SPECT cameras, detector response widens with the distance from the detector surface due to the collimators used to define LORs and is also non-uniform with respect to this distance. Some penetration may also occur through collimator leaves (septas) which causes smoothing of the detector response [10].

2.2.2 Physical Effects

Gamma photons may be scattered out of the detector plane, while passing through the object material, or may be totally absorbed inside the object. Both of these effects are known as attenuation collectively. This effect can be explained by Beer's Law and the probabilities of photons reaching the detector surface can be given by [15],

$$P_{line} = e^{-\int_{Line} \mu(x,y)dxdy} \tag{2.1}$$

In this relation $\mu(x, y)$ is the linear attenuation coefficient of the material, at location (x, y) inside the object $f(x, y)$ integrated, along the *Line*, the line of integration along which gamma ray travels and P_{line} is the survival probability of these photons along that line.

(a) **Angular LOR effect on Point Spread Function**

(b) **SPECT Point Spread Function**
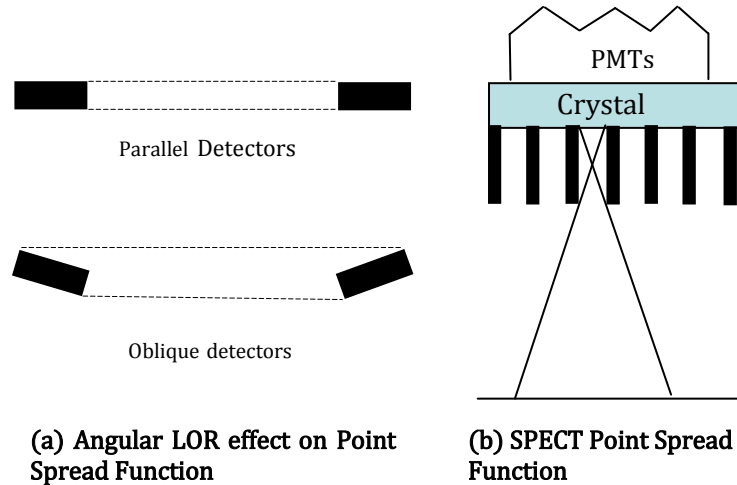
Figure 2.4: (a) Effect of crystal penetration depth and spread of impulse response at an oblique angle in PET system configuration. (b) Spread of response function with distance of the source from detector in SPECT.

For PET scanners, this line of integration or LOR is the line joining both the detectors in a pair where two opposite gamma rays are detector as shown in Figure 2.5. Hence, in PET system attenuation can be included as a ray dependent effect. In SPECT system, depth of interaction inside the object matters because only one gamma ray is used to detect an emission and, LOR for this emission event is defined by the collimator used. In this case, survival probabilities depend on the depth of interaction inside the object and cannot be simply modeled as a ray dependent factor [4;8;15;16].

Gamma ray attenuation can be calculated by obtaining attenuation correction factors (ACF) from the object distribution. Attenuation correction factors are the inverse of the attenuation probabilities along any particular LORs. In PET, several methods have been proposed to determine these factors [8]. Uniform attenuation correction methods, for example, determine the attenuating object boundaries and then use a uniform attenuation coefficient for that region in various directions. These methods ignore underlying non-uniform distribution of the attenuation inside that region. Transmission scan methods are generally used in PET and SPECT to estimate the attenuation map, which defines attenuation coefficients $\mu(x, y)$ at location (x, y) inside the object $f(x, y)$ [15;17]. Different configurations of transmission scan can be opted to estimate the attenuation map and several configurations have been practically used at the same time with the emission scan. A moving point source or a rotating line source is used and then a ratio of a blank to

transmission scan is calculated to estimate the attenuation map and, emission model is modified accordingly in PET systems.
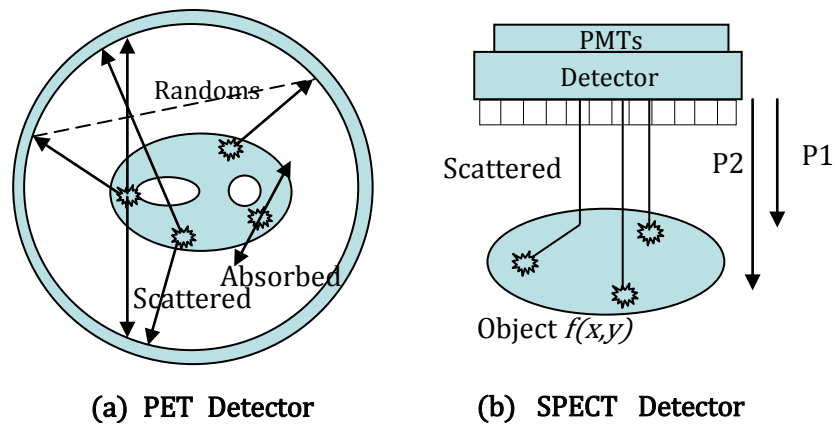
Figure 2.5: Physical effects in PET and SPECT systems, representing attenuation, scatter and random events. Also, the variant effect of attenuation is shown in SPECT, where two events at varying depths, P1 and P2, face different attenuation.

In PET scanners, scattered photons may still be detected if they have not been attenuated completely and will add false information to the detection process, because at the time of detection they might not be moving along the line of their emission [7;18]. In SPECT, they might have not been originated along the line of their detection. These scattered photons can be discriminated on the basis of their energy because mostly they have less energy than their emission energies. Dual or multiple energy window methods have been used to detect these scattered photons which are then subtracted from all the detected events afterwards [9;10]. Practical detectors do not have infinite energy resolution and get a lot many scattered events along with the true detected events. Model based methods have also been devised for scatter correction, however, still a number of scattered events might be detected in addition to the true detection events, so the final reconstructed image is not totally scatter free [19].

PET scanners have another problem of detecting events, known as accidental coincidences, in addition to the attenuation and scattering [20]. If two gamma rays, generated at different locations, reach two different detectors within a time shorter than the coincident timing window of the system, they are regarded as true detection along the line joining those two detectors. They are known as random events which can be estimated in a delayed timing window and can be subtracted later from the total detected events. Background radiation is present everywhere and further contaminates the detection in both PET/SPECT.

2.3   Consequence of Image Degrading Effects and System Model

There are two direct consequences of these image degrading effects including others, i.e. non-uniform reconstructed resolution and partial volume effect which are main focus of this thesis. If these effects are not modeled accurately, reconstructed resolution is limited physically and further becomes non-uniform spatially because these effects are spatially asymmetric. Due to finite resolution recovery, resultant images are prone to partial volume effect (PVE).

2.3.1 Non-uniform Reconstructed Resolution

Quality of images produced by the tomographic imaging systems depends on the above mentioned factors and is, generally, measured in various image quality parameters [21]. There is not a single universal quality measure available which can describe all the images, however, image resolution defined in physical units or in pixels with known pixel size, is the most common index used for this purpose along with noise. Image resolution may, solely, be described in its uniformity and symmetry across the span of the reconstructed images [22-24]. Resolution should be fine (higher) enough to present the smallest features in the image with enough sharpness and it should be uniform (uniformity) or have the same value across the whole image at the same time in all directions (symmetry) [25].

All the factors, discussed above, degrade PET or SPECT system's final response, make it spatially-variant, anisotropic and ultimately degrade quality of the final reconstructed images, produced by these systems, though, other factors such as choice of the image estimator or reconstruction method are also very important [6;24;26-28]. For example, statistical image estimators, based on quadratic priors, induce non-uniform smoothing and, hence, smooth out regions inside the object with varying intensity, producing anisotropic smoothing [26]. This non-uniform smoothing produces non-uniform reconstructed resolution properties in the final image. Anisotropic response of the system will produce shape deformations and will ultimately compromise the quantitation capability of these systems, which is very critical for diagnosis. This will also make various image processing tasks, such as image segmentation, registration and image comparison, difficult and computationally complicated [26;29]. In this work, we have discussed and analyzed tomographic images, with reference to their resolution properties in terms of resolution uniformity and symmetry, produced by various reconstruction methods and have proposed further methods, based on Median Root Based priors (MRPs) for the recovery of the resolution non-uniformity and asymmetry [30]. Another image quality degrading, and

especially quantification influencing factor, which is directly related to the system resolution, is the loss of signal in the form Partial Volume Error (PVE) [31]. PVE is responsible for a direct signal loss in case of objects of a size comparable to the system's reconstructed resolution.

2.3.2 Partial Volume Error (PVE)

Tomographic imaging systems have finite reconstructed resolution and their ability to provide quantitative estimates is limited due to their lower resolution capabilities. Interregional activity contamination might occur among the structures surrounding each other due to limiting power of the system to resolve two small objects across their boundaries [32-35]. The diminishing signal of the true activity for very small regions, within a particular object is also a consequence of the limiting resolution properties [32;36-38]. These effects are collectively known as Partial Volume Effect (PVE). Interregional contamination effect is shown, schematically as a simple example in Figure 2.6. An object partially occupying the smallest detector's sensitive volume, of a tomographic imaging system, produces an apparent reduction in the measured signal. This loss of signal is also known as Partial Volume Effect [39]. It might also occur when the object occupy varying portions of the system's sensitive detection volume at different times or when an object obscures different parts of the detector while being rotated around the object for tomographic data collection.
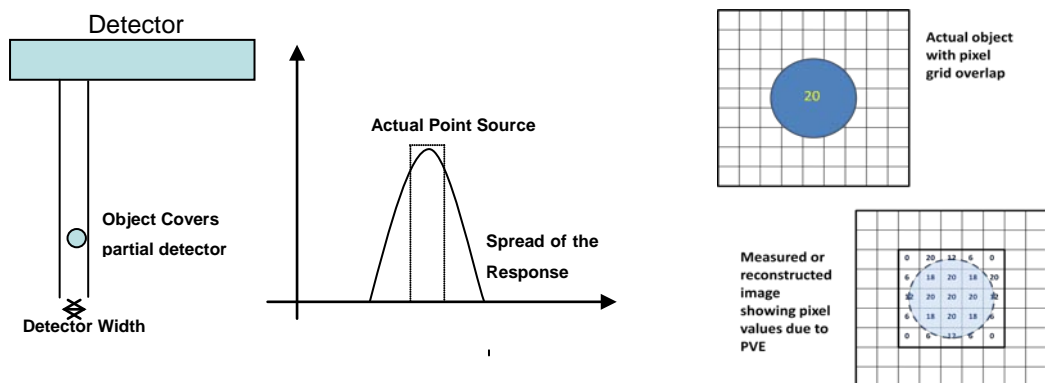
Figure 2.6: Schematic presentation of various causes of PVE, due to point spread function or tissue fraction effect.

PVE creates serious problems for absolute activity measurements in the regions of an image which are comparably smaller than the system's tomographic reconstruction resolution [36]. Regions which are smaller than two to three times of the FWHM of the systems response are severely affected by PVE during activity measurements. PVE

produces errors in quantification of the varying activity concentration levels inside the object [40;41]. Measurements are over or under-estimated, due to spill-over or inter-contamination of the surrounding regional activities, into the concerned region. Main source of error enters into the reconstruction model through the spread of the impulse response function, which is closely related to the systems resolution capabilities [42]. We have compared activity recovery performance of various reconstruction algorithms, including various priors in MAP estimators, in this work, to assess capabilities and improvements which different prior functions may offer to select for the best prior distribution function [31].

In next sections, we briefly introduce mathematical background of data acquisition, modeling and formulation of the tomographic image reconstruction problem with various methods to solve it, either in its analytical or discrete form while considering their advantages and disadvantages related to their resolution and noise properties and their ability to control these properties in the final reconstructed images.

2.4   Data Acquisition Modeling

Ideally, in 2D PET, data acquisition can be described as a line or strip integral model of the acquisition of gamma rays coincident events. Two gamma rays traveling and being detected along a line, joining the two small detectors, within a small coincident timing window (generally of 12-20 ns), generate a coincident event as depicted in Figure 2.7 [2]. Theoretically, number of all such collected events along a particular LOR, accumulatively, will be proportional to the total amount of radiotracer concentration present along that LOR, if not corrupted by various physical effects, such as attenuation, scatter and accidental coincidences etc. Number of counts along each LOR, and all the LORs put together, make up the acquired data which is further divided into parallel set of LORs along various angles in PET and are, generally, represented as a sinogram image, in 2D, because a single point will traverse a sine curve in the sinogram space [4;43;44].

We need to mathematically model the acquired data in order to formulate our tomographic image reconstruction problem, and further to solve it [45]. Forward modeling is defined as describing mathematical models to relate the measured quantities to the unknown quantities of interest [46-48]. It is a mathematical mapping, based on some underlying physical theory, from the input space to those values in the data space, which we are able to measure through our system. Main objective of a forward model is to make ourselves be able to generate data which are as likely as possible to the observed data, if the unknown quantities were known.
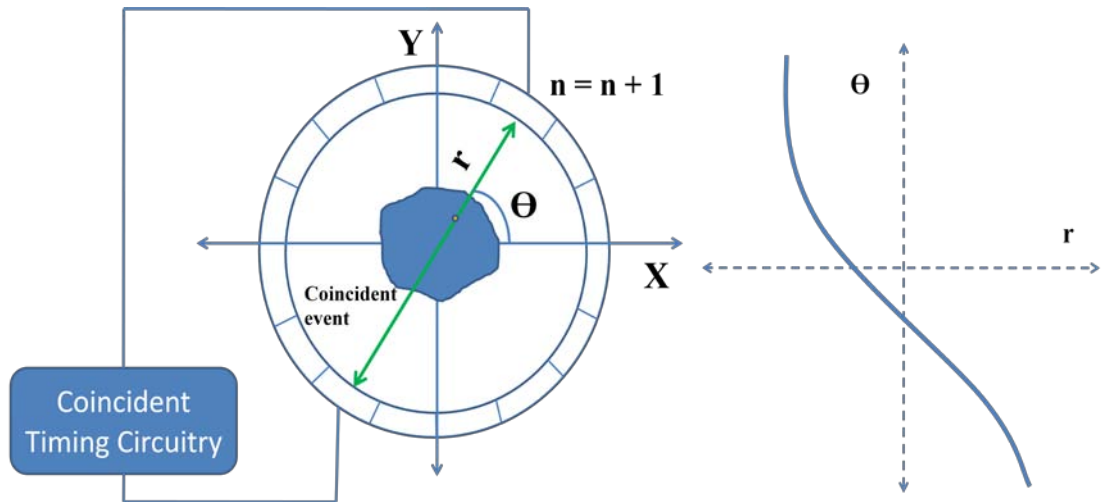
Figure 2.7: (left) Data acquisition modeling for PET system depicting an emitted pair of the photons being detected at angle Θ with the X-axis. The counter is incremented at the bin where this event is detected. (right) Sinogram of a single hot spot in field of view is shown to traverse a sine curve in the sinogram space.

This forward mapping may be linear or non-linear and, hence forward problems could be of several types, depending on the nature of the object and data representations, which could be continuous or discrete or both [46].

2.4.1 Continuous-Continuous Model

Measurements of tomographic imaging system may be considered as ideal projections of the object distribution onto a detector continuum, as shown in Figure 2.8. A set of LORs is shown with a generic simplified continuous model. Let $f(x, y)$ denotes[1] an object distribution function defined over $\mathbb{R}^2$. Assume $p_\theta(r)$ represents an ideal projection of the object intensity, as a function of radial distance r at an angle θ, and is related to the object as a line integral along the line $L(r, \theta)$ in polar coordinates in 2D as follows,[1]

$$p_\theta(r) = \int_{Line(r, \ \theta)} f(x, y) ds$$

$$p_\theta(r) = \iint_{-\infty}^{\infty} f(x, y) \delta(x \cos\theta + y \sin\theta - r) dx dy \qquad (2.2)$$

A complete collection of all projections around the object $\{p_\theta(r) : \theta \in [0, \pi], r \in -\infty, \infty$ is known as its Radon Transform [45].

---

[1] $f(x, y)$ is assumed to be the object centered at origin along x *and* y axis in real 2D space. Distance r is generally considered from origin on 1D line, and in real practice considered to be bounded by object support.
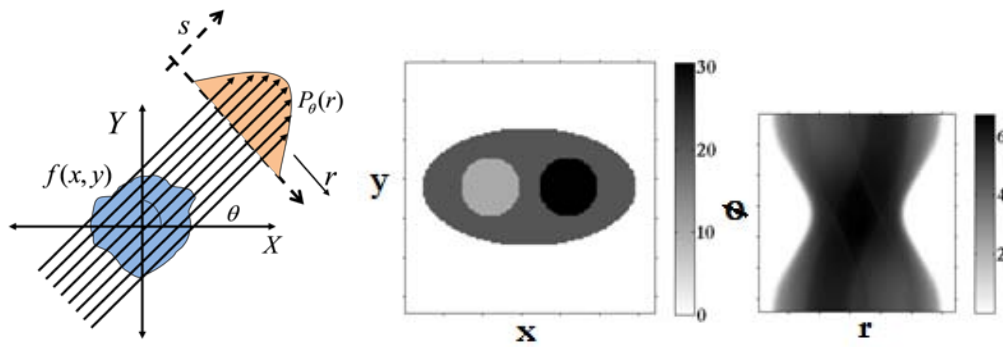
Figure 2.8: Depiction of mathematical data acquisition modeling with projections shown at an angle for ideal projections and object with its sinogram.

This data is also known as a sinogram in tomographic imaging terms, because shape of single point projections, collectively, resembles a sine curve. An object, with its Radon transform, is shown in the Figure 2.8, for continuous variables. Equation (2.2) presents the case when absorption properties of the object to the radiation are not modeled. If we include attenuation into the above model, as shown in equation (2.3), it is known as Attenuated Radon Transform (AtRT), for which it is difficult to find an analytical inverse, which has been discovered by Novikove R. [80].

$$p_\theta(r) = \int_{Line\,(r,\ \theta)} f(x,y)e^{-\int \mu(s)ds}\,ds \tag{2.3}$$

In this relation $\mu(s)$ is the non-uniform attenuation coefficient of the object, integrated along the line of emission and is a gamma ray energy dependent parameter. These coefficients are commonly used as a-prior information obtained by carrying out a transmission scan first. Though, continuous model is useful for simplified theoretical analysis of the problem, we can only measure a finite number of data points with real systems, and so, continuous models are always an idealization. Also, because computer implementation is necessarily purely discrete, so reconstruction problem is implemented in discrete form.

2.4.2 Discrete-Discrete Model

A finite set of measurements are, commonly, obtained from a system that makes measurements on a continuous object distribution function. This invites for a semi-discrete

or continuous-discrete modeling of the problem. However, real systems provide discrete measurements along some discrete detector array and, similarly, object distribution may also be represented in discrete parameterization form. Discrete-discrete modeling of the object distribution and the system output helps in reducing data storage and its manipulation by computers. Data discretization is normally decided by the design physicist or design engineer and is very often oversampled with a multi-index set of numbers which are a pair of numbers for 2D and a triplet for 3D data. For idealized system, data can be represented in discrete form as a set of equations for simplicity [46;47;49],

$$y = Hf + b \tag{2.4}$$

Here, H is the system matrix or forward matrix, which linearly relates the object represented in discrete vector form as f and the measurement vector represented in discrete form as y. Vector b is the noise vector which includes noise from various sources such as background or electronic noise.

2.5   Tomographic Imaging System Model

Linear transformation operator $H = \{h_{ij}, i = 1,..,M, j = 1,..,N \}$, with N number of object pixels and M number of LORs, in equation (2.3), describes a physical transformation from object space to the data space. Quantitative PET image reconstruction using statistical techniques requires a system model that represents the probability of detecting an emission from each image pixel at each detector-pair. By accurately modeling these probabilities we can maximize resolution recovery by minimizing spatial distortions which are mainly a result of simplified assumptions about the system and the process. Operator H, which is also known as the system matrix, may be factorized as a product of independent contributions from system's geometry, attenuation effect, positron range, detector blurring effects and detector sensitivity etc. [23;50]. This matrix is generally huge and, although factorization can drastically reduce its size, it also introduces over-simplifications at the same time, because the whole matrix cannot be expressed, in the general case, as a product of diagonal matrices [23]. Mumcugulo et. al. (1997), introduced a simple factorization scheme to include various physical and detector based image degrading effects into the system matrix, as given below, which has also been used by many others researchers [6;28;51;52].

$$H = H_{sens} \, H_{atten} \, H_{scatt} \, H_{geom} \tag{2.5}$$

In this relation, H_{geom} is a $M \times N$ matrix with each $(i, j) \, th$ element equal to the probability of a photon pair produced at the $j - th$ pixel reaching the $i - th$ detector pair without passing through any attenuating or scattering medium and with perfect photon pair co-linearity. H_{scatt} is an $M \times M$ matrix and models the effects of photon non-co-linearity, inter crystal scattering and crystal penetration. These factors ultimately produce blurring in the detector response. H_{atten} is a diagonal $M \times M$ matrix having attenuation correction factors on its diagonal which can be computed in a usual way from the ratio of blank to transmission scan. H_{sens} is again a $M \times M$ matrix and may include radially varying geometric efficiencies due to the ring structure, detector pair geometric efficiencies due to non-parallel detector surfaces and dead time etc.

It should be noted that this factorization scheme is not unique and researchers have used other schemes too [24;154]. For example, Fessler and Rogers [24] have used only two factors where one matrix holds ray dependent factors, such as attenuation, and the other matrix hold voxel based factors, such as scatter etc. These factorized matrices operate one by one on the data to correct for certain physical or detector based effects similar to that of back projection operator; hence, their various combinations produce ignorable differences. For example, diagonal matrix, H_{atten} containing attenuation coefficients in the above relation may be applied before or after the scattering matrix H_{scatt}, because its operation will correct for the attenuation experienced by the gamma ray events being registered. However, once results are obtained with a particular factorization scheme, the order may be retained for consistency, because matrix multiplication is not commutative.

Geometric elements of the system matrix can be calculated analytically or by simulation. Analytically, these elements can roughly be approximated by the intersection length of a zero width line that connects the pair of detectors with each pixel or voxel or may be evaluated using some interpolation method [11;53]. A more accurate approach, for 2D, involves calculation of the area of intersection between a pixel and the strip of response or, in 3D, volume of intersection between voxels and the tubes-of-response [54]. Multiple ray tracing methods have also been proposed in 3D to combat the complexity of calculations of the volume of intersection and properties of the crystal [55]. Figure 2.9, elaborates this idea for a single column of the pixels array and an LOR at angle θ.
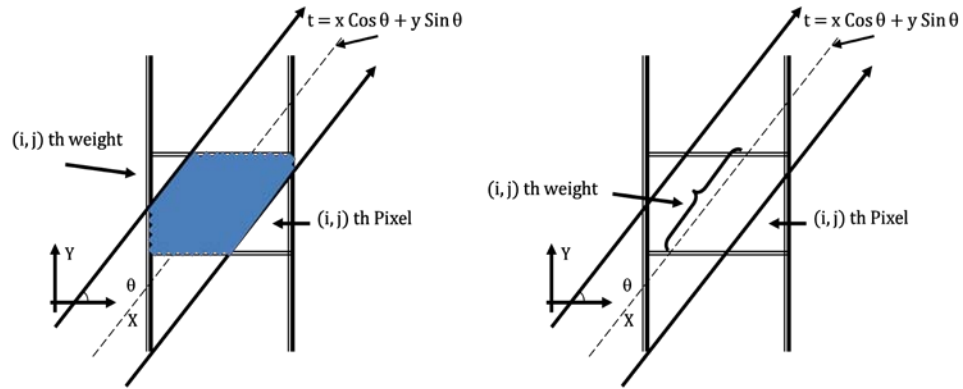
Figure 2.9: (left) Intersection area of LOR and a single pixel, giving probability of an emission from that pixel and detected in the same LOR. (right) Intersected length of the central line of LOR beam within a pixel, estimates an element of the system matrix.

An inefficient, though very simple, way to evaluate these probabilities is to compute intersection lengths for each pixel and for each ray line in sequence. Siddon (1985), devised an efficient method to take into account only those pixels which are intersected by a particular LOR, to calculate these probabilities for CT imaging [53;56]. There are several new variations developed for this method [57-59]. Spatially variant response models can be calculated by measurements based on point-source acquisitions at varying locations inside the field of view or by simulation [60;61]. Monte Carlo (MC) simulation of the system matrix elements, which allows incorporation of the model of the most relevant physical effects involved, is another choice and different PET or SPECT dedicated Monte Carlo simulation codes are available for this purpose [62]. Pre-reconstruction calculation of the system matrix elements is a valid approach for any specific device, except for the object-dependent effects, such as scatter and attenuation in the source distribution [63;64].

A fully 3D system matrix may contain trillions of elements and imposes restrictions on computing and storage demands, even in case of pre-calculated matrices. Luckily, geometric system matrix is highly sparse and in general having very few non-zero elements, whereas this sparseness can be exploited to reduce its size [64]. However, inclusion of scatter into the system matrix reduces its sparseness a lot. Physical processes such as positron range, non-collinearity of the emitted gammas or scatter in crystal are generally neglected in order to speed up the reconstructions, while compromising their accuracy [65]. For the same reason of simplicity and speed, we also used a system matrix in our analysis, which is mainly comprised of geometric system elements while other factors are ignored. However, for the sake of generality, we included attenuation in our non-uniform resolution compensation analysis.

2.6 Reconstruction Problem Formulation – Discrete Version

In its discrete form, data are usually assumed to be an ordered vector with m number of components and denoted by $y = \{y_i\}_{i=1}^m \in \mathbb{R}^m$. Object distribution may also be assumed to consist of an ordered set of multi-indexed numbers with n components denoted by $x = \{x_j\}_{j=1}^n \in \mathbb{R}^n$. Mathematical modeling of the imaging system implies the use of equations which describe propagation of radiations emitted by the object and detected by a series of detectors [66]. If $f(x,y)$ is a function of space variables and denotes properties of the object, a transform mapping this function onto the sampled values of the exact radiations (radiations before detection), denoted by vector y can be expressed as follows,

$$y_i = \left(Hf(x,y)\right)_i + b_i \; with \; H_{ij} \geq 0.$$
$$for \; i = 1, \dots, M \; and \; j = 1, \dots, N$$

(2.6)

Here, H could be a discrete or semi-discrete mapping, sometimes referred to as operator, and $b = \{b_i\}_{i=1}^m$ is a vector representing background noise. The mapping or transforming matrix H represents the imaging system and the condition $H_{ij} \geq 0$ means that matrix elements are non-negative. This operator is also known as forward model which is towards the noiseless data $\breve{y} = Hf$ and vector $b = y - \breve{y}$ is the noise term. It is easier to solve the noiseless forward problem, however, the noise term makes the problem highly ill-conditioned and, to invert it, is very difficult [67].

2.6.1 Tomographic Reconstruction as an Inverse Problem

Almost always, we want to use this forward model H and the observed noisy data y to make inference on the unknown quantity of interest f: This is the inversion problem [46;48;49]. Image reconstruction, where we try to estimate source distribution inside the object being imaged using data acquired by an imaging system, is an example of an inverse problem in its mathematical formulation [66;68]. For tomography systems, this matrix is generally very sparse, though of very large size, and its condition number, which is a ratio of the largest to the smallest singular values, is very large [69].

Inverse problems are almost always ill-posed in Hadamard sense, which means that the solution of the problem may not exist, not unique or may not continuously depend on the data [70]. First two conditions are to make sure that inverse of the transform is well defined and whole data space is domain of the inverse transform. Requirement of

continuous dependence of the solution image on the data is a necessary but not sufficient condition for stability of the solution. Hadamard went on to define a problem to be ill-posed, if it does not satisfy all the above three conditions. So an ill-posed problem is one, where, an inverse does not exist, because, the data is outside the range of H, or the inverse is not unique because more than one image is mapped on to the same data, or because an arbitrarily small change in the data can cause an arbitrarily large change in the image [70]. Simplest way to solve this problem is to mathematically invert it.

2.6.1.1 Direct Matrix Inversion

The ill-conditioning of the reconstruction problem is due to very small singular values of H, which can be observed if we replace H by its Singular Value Decomposition (SVD); or $H = U\Sigma V^t$, where U and V are unitary matrices and Σ is a diagonal matrix composed of singular values. Least square solution, for noiseless data will become $\check{f}_{LSQ} = V\Sigma^{-1}U^t\check{y} = \sum_{i=1}^{N} \frac{1}{\sigma_i} u_i^t \check{y} v_i$. Here, u_i and v_i are the *ith* column of matrices U and V. Clearly, for very small singular values σ_i, the solution will become unstable [67]. For a brief analysis we may observe that in case of a well-posed problem, relative error propagation from the data to the solution is controlled by the condition number. If Δy is a variation in y and Δf, the corresponding variation in f then,

$$\frac{\|\Delta \boldsymbol{f}\|}{\|\boldsymbol{f}\|} \leq cond(H)\frac{\|\Delta \boldsymbol{y}\|}{\|\boldsymbol{y}\|}, \tag{2.7}$$

and, for linear forward problems,

$$\boldsymbol{cond}\,(\boldsymbol{H}) = \|\boldsymbol{H}\|\|\boldsymbol{H^{-1}}\|$$

Since, the fractional error in f equals the condition number multiplied by the fractional error in y; smaller values of condition number for matrix H are desirable [67;71;72]. If $cond(H)$ is not too large, the problem is considered to be well-conditioned and the solution is stable with respect to small variations in the data. Otherwise, the problem is said to be ill-conditioned. It should be noted that the above relation is only valid for square matrices for the purposes to calculate matrix inverse.

Direct inversion is not very popular due to ill-conditioned reconstruction problem because it is not straight forward to include regularization explicitly. Even very small ill-conditioned matrix will require regularization for stable solutions. Similarly, for very large

matrices inversion is not very efficient and requires large memory space to hold the matrices involved. Hence, factorization is used to reduce the problem size and its complexity in iterative manner, though large memory requirements may still slow down or hinder the numerical evaluations [48;67;69;72].

2.6.2   Solving the Inverse Problem - Reconstruction Methods

A concept of well-conditioned problems, as discussed above, is lesser distinct than the concept of well-posed problems. Most correctly stated, inverse problems turn out to be ill-posed or at least ill-conditioned due to very high condition number of the inverse operator; any attempt to solve it by simple analytical inversion methods fails, though there are some simplified inversion techniques available such as DFR or FBP. However, meaningful information can be gained from ill-posed inverse problems, even though they cannot be strictly inverted. Mathematical theory of regularization or theory of generalized inverses, which is an extension of the theory of the Moore-Penrose inverse of a matrix, is usually applied to investigate problems that are not well posed [73]. Classical Tikhonov regularization is a well developed theory for linear ill-posed problems with a key idea to approximate a discontinuous operator with its continuous approximate functionals [71;74]. For linear ill-posed inverse problems, with compact linear forward transformation, Singular Value Decomposition (SVD) can be used to find the inverse transformation. However, for ill-posed problems, solution gets unstable for very small eigenvalues as discussed above. Inverse transformation can be regularized by limiting the smallest singular values. A filter factor, where filtering is introduced as a type of implicit regularization, can be included to set very small singular values equal to zero. Various types of filter factors such as Truncated SVD Filter, Tikhonov Filter or Exponential Filter have been proposed [67]. Variation regularization and regularization by defining some prior function in MAP estimators are different options to define explicit regularization functionals. Generally available mathematical tools for such inverse problems are either the deterministic regularization theory or the probabilistic Bayesian inference and estimation theory [60;74-77]. Filter factor has the least control on the reconstructed resolution which mainly depends on the properties of the filter chosen and it is also very difficult to choose a cut-off value.

Analytical reconstruction of images, from tomographic data, means to obtain function $f(x, y)$ by inverting analytical equation (2.2) assuming continuous variables given in the relation. These types of methods are known as direct or Analytical Reconstruction Methods [78]. They are considerably faster as compared to the iterative reconstruction methods,

where a discrete representation of the object is being estimated using some estimation algorithm from a discrete data vector using some underlying forward model. However, some of the iterative algorithms involve evaluation of certain analytic inversion formulae, too [56;79].

2.7 Analytical Reconstruction Methods

In tomographic imaging, data are ideally considered to be line integrals with the sum of all line integrals together known as Radon Transform (RT) of the emission or absorption properties of the object being imaged. An explicit analytical inversion formula is required to recover the object distribution from the data i.e. to determine $f(x, y)$ from the measurements of its transform $p_\theta(r)$. Radon (1970), found an explicit formula for the inversion of ordinary Radon Transform [45]. Analytical reconstruction methods are intrinsically very fast as compared to their companion iterative reconstruction methods. Historically, derivation of the generalized exponential Radon transform was found by Tretiak and Metz and further explicit formula for the inversion of the attenuated Radon transform was discovered by Novikov [80;81]. Slightly later, Frank Natterer supplied a simpler proof of Novikov's formula [80;82]. If attenuation of the object can be approximated as uniform attenuation with defined contour the attenuated Radon transform reduces or simplifies to the exponential Radon transform with some inversion formulas given in [83]. Below we briefly describe Novikov's formula with inverse Radon transform.

2.7.1 Inverse Radon Transforms (IRT)

The basic mathematical problem of both emission and absorption tomography is to reconstruct a distribution function $f(x, y)$ from the knowledge of its Radon transform or $\mathcal{R} = p_\theta(r)$ as given by equations (2.2) and (2.2A). For emission data, without considering attenuation, Radon transform of the object $f(x, y)$ over real space $\mathbb{R}^2$ may be written for $r \, \epsilon \, \mathbb{R}$ and $\theta \, \epsilon \, (0, 2\pi)$ as,

$$p_\theta(r) = \mathcal{R}f(r, \theta) = \int_{\mathbb{R}^2} f(x, y)\delta\big((x, y).\theta^\perp - r\big)dxdy \,.,$$

In this equation $\theta^\perp = (-\sin\theta, \cos\theta)$ and $\theta' = (\cos\theta, \sin\theta)$, for $\theta \, \epsilon \, (0, 2\pi)$. For inverse Radon transform we need to define the Hilbert transform of a function $u(t)$ as follows with its integral representing a Principal value integral,

$$Hu(t) = \frac{1}{\pi} \oint_{\mathbb{R}} \frac{u(s)}{t-s} ds \qquad (2.8)$$

With this definition, the function $f(x,y)$ can be reconstructed using inverse of its Radon transform $\mathcal{R}f(r,\theta)$ as follows,

$$f(x,y) = \frac{1}{4\pi} \int_0^{2\pi} \left(H \frac{\partial}{\partial r} \mathcal{R}f(r,\theta) \right) ((x,y).\theta^\perp, \theta) d\theta \qquad (2.9)$$

This is the well known Radon inversion formula to evaluate $f(x,y)$ from its Radon transform [45]. However, if attenuation is included then forward transform is called the attenuated Radon transform (AtRT) and evaluation of its inverse become complex. An inversion formula for the AtRT has been discovered by Novikov where attenuation is considered with emission data. Novikove's formula may briefly be described in terms of a feasible function and its Hilbert transform. Say, $f(x,y)$ is a transferable function and $g = \mathcal{R}_a f$. The AtRT $\mathcal{R}_a f(r,\theta)$ may be defined as,

$$\mathcal{R}_a f(r, \theta') = \int_{Line\ l} e^{-D_a(x,y,\theta^\perp)dl} f(x,y) dxdy$$
$$D_a(x,y,\theta^\perp) = \int_0^\infty \mu(x,y,\theta')dl \qquad (2.10)$$

For $\mu = 0$, $\mathcal{R}_a$ is usual Radon transform. In emission tomography, $f(x,y)$ represents the emission distribution and $\mu(x,y)$ denotes the attenuation distribution, whereas, problem is to recover $f(x,y)$ from AtRT with known attenuation map. A relevant formula is called the inverse Radon transform. Let us define a function h,

$$h = \frac{1}{2}(I + iH)\mathcal{R}_a, \qquad (2.11)$$

where, H is the Hilbert transform defined in equation (2.8). Then Novikov's inversion formula may be given as,

$$f(x,y) = -\frac{1}{4\pi} \Re e \; div \int_{S^1} \theta' e^{-D_a(x,y,\theta^\perp)} \left(e^h He^{\bar{h}} \breve{g} \right)(\theta',(x,y).\theta')d\theta' \qquad (2.12)$$

With $\breve{g}(r,\theta') = \mathcal{R}_a f(-r,-\theta')$. This relation can be used to find inversion of attenuated Radon transform for which full proof may be sought in [80;82]. By manipulating various arrangements of the Radon transform in Cartesian or polar coordinates, several simpler inversion schemes for the RT are available. These are simpler in implementation as compared to the fully analytical inversion formulae. Few popular schemes are DFR based on Fourier Slice Theorem (FST), Back-projection Filtering (BPF) based on linograms and FBP based on Fourier Slice Theorem [84-87].

2.7.2 Direct Fourier Reconstruction (DFR)

Fourier Slice Theorem may be summarized as; "The 1D FT of parallel projections of an object $f(x,y)$, taken at an angle θ_i, gives a slice of the 2D FT of the object, $F(u,v)$, subtending an angle θ_i with the u axis" [85]. Using Fourier Slice Theorem, in DFR method, 2D Fourier Transform of the object $f(x,y)$ is obtained by plotting *1D* Fourier transform of its projections $p(r,\theta)$, for a range of angles θ, onto a polar grid and then converting this polar grid into a Cartesian grid by interpolation, known as gridding process. Object $f(x,y)$ can be recovered by *2D* inverse Fourier transform (IFT), however, the gridding process amplifies noise at higher frequencies.
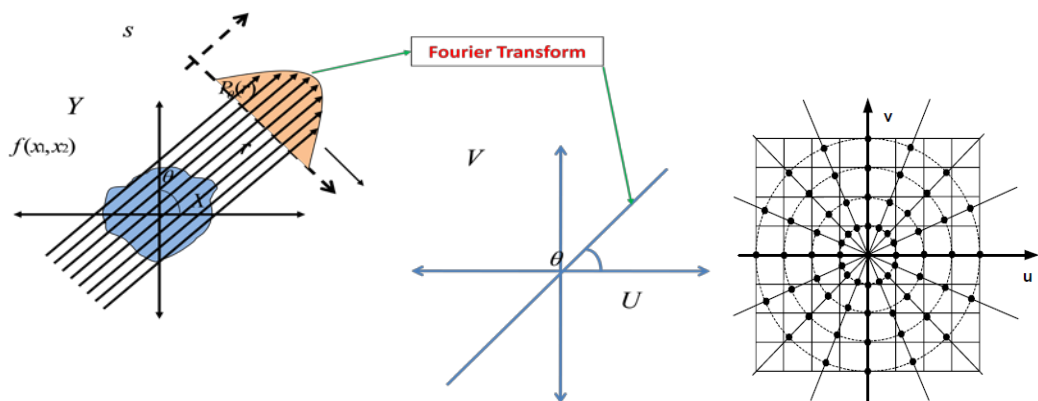
Figure 2.10: Depiction of Fourier Slice Theorem (FST). Fourier reconstruction (FR) generates values on a polar grid.

In BPF, projections are backprojected and then filtered with a cone filter, whereas, cone filter has the same issue of amplifying high frequency noise components. An

unbounded spatial support requirement for the linogram, even for a finite support object, is a practical difficulty of this method [86-88].

2.7.3 Inversion by Filtered Back-projection (FBP)

In BPF, support of the linograms must be truncated, in practice, to a finite size for implementation and computer storage purposes, which can cause problems with the de-convolution step. A larger support increases computational costs of both the back-projection step and the 2D FFT operations used for the cone filter. The Filtered-Back-projection (FBP) reconstruction algorithm largely overcomes this limitation [84;87;89;90]. The FBP method requires only 1D FT and then 2D FT $F(u, v)$ in Fourier variables u and v can be used to recover the object $f(x, y)$ in Cartesian coordinates x and y by its conjugate operator Inverse Fourier Transform (IFT) as follows,

$$f(x, y) \;=\; \int_{-\infty}^{\infty} \int_{-\infty}^{\infty} F(u, v) e^{i2\pi(xu+yv)} \, dv du \qquad (2.13)$$

By changing from Cartesian coordinates (u, v) to Polar coordinates (r, θ), where $u = r \cos \theta$ and $v = r \sin \theta$ and $dudv = \begin{vmatrix} \frac{\partial u}{\partial r} & \frac{\partial u}{\partial \theta} \\ \frac{\partial v}{\partial r} & \frac{\partial v}{\partial \theta} \end{vmatrix} dr d\theta = r dr d\theta$, and by substituting these values in the above equation (2.13) we get,

$$f(x, y) = \int_{0}^{2\pi} d\theta \int_{0}^{\infty} F(r \cos \theta, r \sin \theta) e^{i2\pi r (x \cos \theta + y \sin \theta)} \, r dr$$

Using Fourier Slice Theorem, and by replacing 2D FT with 1D projections of the object being imaged, we would get,

$$f(x, y) = \int_{0}^{2\pi} d\theta \int_{0}^{\infty} P_\theta(r) e^{i2\pi r (x \cos \theta + y \sin \theta)} \, r dr$$

$$= \int_{0}^{\pi} d\theta \int_{0}^{\infty} P_\theta(r) e^{i2\pi r (x \cos \theta + y \sin \theta)} \, r dr$$

$$+ \int_{0}^{\pi} d\theta \int_{0}^{\infty} P_{\theta+\pi}(r) e^{-i2\pi r (x \cos \theta + y \sin \theta)} \, r dr$$

And using symmetry property of the projections in case of parallel geometry about the π line we get,

$$f(x,y) = \int\limits_{0}^{\pi} d\theta \int\limits_{-\infty}^{\infty} P_\theta(r)|r|e^{i2\pi r(x\cos\theta + y\sin\theta)} dr \qquad (2.14)$$

The inner integral is Inverse Fourier transform of the filtered version of projections $P_\theta(r)$ at angle θ by a filter having a frequency domain response of $|r|$ and is called "filtered projections". If we substitute $Q_\theta(x\cos\theta + y\sin\theta) = \int_{-\infty}^{\infty} P_\theta(r)|r|e^{i2\pi r(x\cos\theta + y\sin\theta)} dr$ then object $f(x,y)$ can be recovered or reconstructed by simple back-projection of these filtered projections at all angles as follows,

$$f(x,y) = \int\limits_{0}^{2\pi} Q_\theta(x\cos\theta + y\sin\theta)\, d\theta$$

This smearing back or back-projection method of the filtered projections to retrieve the object distribution is known as Filtered Back-projection and this equation states that the reconstructed image of the object $f(x,y)$ at point (x,y) is a summation of all the filtered projections passing through that point. Figure 2.11, presents images reconstructed by FBP of a Shepp-Logan phantom with different number of projections [88;91]. These images clearly show that quality of reconstructed images heavily depends on various parameter values, for example number of projections in this case. Analytical reconstruction methods are very fast as compared to the iterative methods and have strong mathematical theory behind their derivation, however, they assume data to be a simple line integral model which is not real, and it is not simple to include various image degrading effects into the system model [23;60;79;92-94]. Also, they ignore any statistical nature of the counting process and any underlying noise distribution or the non-negativity condition of the counting systems; hence, their reconstructed images bear inferior bias and variance properties. For better resolution and noise properties, and better resolution control, statistical iterative methods are preferred over them [10;12;34;39;95].
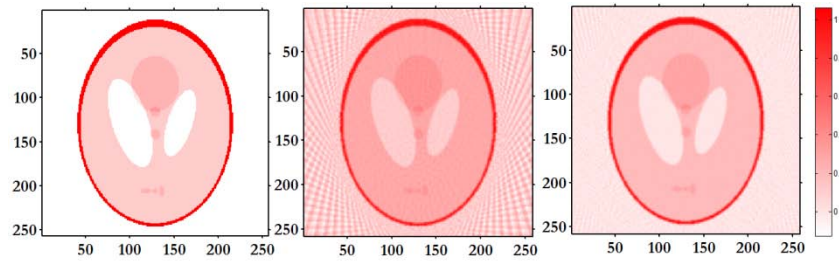
Figure 2.11: Effect of number of projections on the FBP reconstructed images. False reconstructed activity in the form of streaks is reduced by increasing the number of projections however is not eliminated.

2.8 Iterative Reconstruction (IR)

Tomographic image reconstruction problem is, generally, solved in its discrete form, with finite dimensions; however, even in this form the problem is ill-conditioned due to incomplete data and noise. Iterative reconstruction methods assume object parameterization, as a set of unknowns, by assigning some initial value to them and then try to find a better fitted image update, iteratively, based on some compromise between the estimated projections and the true projection values.

2.8.1 Linear Least Square Reconstruction (LSQ)

Deterministic methods may be used to solve this problem without formulating any, explicit, probabilistic model. An estimate of the reconstructed image may be obtained by defining a mismatch between observed data and an output of a theoretically defined model, generally known as the Least Squares Estimate (LSQ) [66;67;96].

$$\hat{f}(x,y) = \underset{f}{\mathrm{argmin}} \|y - H(f)\|^2 \tag{2.15}$$

This solution is very simple and easily interpretable[2]. It is a solution to the set of linear equations $y = Hf$, noticeably only considering the data and ignoring the noise altogether. Possible variations of the above formulation could possibly be Weighted Least Square (WLS) solution, L_p Norm solution or Kullback-Leibler (KBL) mismatch solution etc. This approach works well for well-behaved problems in Hadamard sense; however, it fails to provide a satisfactory solution, if the problem is ill-conditioned or ill-posed. In tomographic imaging, the solution may not exist, not unique, or most commonly, it may depend discontinuously on the data and will simply be very sensitive to errors or noise which may

---

[2] $\hat{f}$ with cap means estimated value of the variable object from noisy measurements.

drive it unpredictably. This, generally, happens if the range of the forward data operator is not closed and its inverse is not defined everywhere in the data space [46;67-69;72].

2.8.2 Algebraic Reconstruction Methods (ARM)

Another approach to find a best solution to the set of linear equation $y = Hf$, is to set up algebraic equations for the unknowns, in terms of the measured projection data with some defined compromise between measured and the calculated projections. These methods are commonly referred to as algebraic reconstruction techniques (ART) and try to find the final solution in an iterative process [56;56;85;97-99].

$$y_i = \sum_{j=1}^{N} h_{ij} f_j \quad i = 1, \dots, M \text{ and } j = 1, \dots N \tag{2.16}$$

Here y_i is the $i - th$ data bin, h_{ij} is the contribution from the $j - th$ pixel to the $i - th$ data bin and f_j is the $j - th$ unknown parameter to be evaluated. Flow of the algorithm is such that the current estimates are compared with the measured projections, instead of back-projecting the average ray value as in FBP, and the resultant is used to modify the current estimate, thereby creating a new updated estimate. The reconstruction process starts with an initial estimate of the object values and tries to drag the updated projection estimates nearer to the true projections, with proceeding iteration number. For very large number of pixels and projection rays, an iterative method to solve above system of linear equations is known as the Kaczmarz method [85;92].

$$f_j^{k+1} = f_j^k + \lambda. (y_i - \sum_{j=1}^{N} h_{ij} f_j) / \sum_{j=1}^{N} h_{ij} \tag{2.17}$$

This is an equation to update value of the $j - th$ unknown or pixel at each iteration and is the well-known additive form of the algebraic reconstruction technique (ART) algorithm where second term, on the right, is a correction factor for $i - th$ ray. Here λ is a relaxation parameter which controls the correction step.

2.8.3 Conjugate Gradient Method (GC)

Another example of such kind of iterative algorithm, where solution is iteratively searched for, using some criteria on the comparison of the data and estimated solution and

then modifying the solution image accordingly, is called the gradient algorithm, or steepest-descent algorithm. Every new estimate of the image is found by adding some vector indicating the new direction vector, chosen to be opposite to the local gradient weighted by a coefficient representing the step length. Convergence of this algorithm highly depends on the choice of this coefficient, however, gradient direction is only the locally best direction and, hence, the algorithm is not very efficient. In an efficient version of this algorithm, known as the Conjugate Gradient (CG) algorithm, the p^k vector indicates a direction towards a combination of the direction of the current gradient and a gradient found at the previous iteration. Mathematically, this algorithm can be given as below followed by Polak-Ribiere CG method [100],

$$f^{k+1} = f^k + \alpha_k p^k \qquad (2.18)$$

Every new estimate of image f^{k+1} is found by adding some vector indicating the new direction vector p^k, which will be [100],

$$p^k = q^k + \gamma_k p^{k-1} \qquad (2.19)$$

With,

$$\alpha_k = \underset{\alpha}{\text{argmin}}\ \varphi(f^k + \alpha p^k)$$
$$\gamma_k = \begin{cases} 0, & k = 0 \\ \dfrac{(g^k - g^{k-1}, q^k)}{(g^{k-1}, q^{k-1})} & k > 0 \end{cases} \qquad (2.20)$$

Where $g^k = -Gradient(Objective\ function\ of\ f^k)$ to be maximized and $q^k = \boldsymbol{M}g^k$, with $\boldsymbol{M}$ as the pre-conditioner used to speed up the convergence rate by reducing the ill-conditioning. However, these algorithms may generate negative values in the reconstructed images, because of its mathematical formulation and one need to be very careful in choosing parameter values [100;101].

2.8.4 Maximum Likelihood Expectation Maximization (MLEM)

In tomographic imaging systems, measurements are subject to variations due to the Poisson probabilistic phenomena of the radioactive disintegrations and consequently every dataset realization y corresponds to a particular measurement. In the framework of linear set of equations if we do not take into account the probabilistic nature of the phenomena, $\hat{f}$ is a particular solution corresponding to that particular measurement y. MLEM algorithm

tries to find a general solution as the best estimate $\hat{f}$, with the maximum likelihood (ML) as the criterion that can produce the given data y [91;102;103]. Poisson law is, generally, used to evaluate the probability of mean detected events count given the mean number of disintegrations. Thus, an iteration of the algorithm is divided in 2 steps: in the expectation step (E step), which means a formulation expressing the likelihood of any reconstructed image given the measured data, and in the maximization step (M step), to find the image that has greatest likelihood to give the measured data. EM algorithm can be visualized as a set of successive projections and back-projections. However, MLEM algorithm has notoriously slow speed of convergence and may require up to 200 iterations or more to converge [90;95;104].

In statistical approach, assuming that we know the probability density $p(y|f)$ of the data y given the object density f in parametric form, image reconstruction problem becomes a parametric estimation problem i.e. estimation of a realization of the unknown object f corresponding to a data realization y. For maximum likelihood (ML) estimation, the likelihood of the data y, given image f, may be written as,

$$L_y^Y(F = f) = p_Y(y|f) \tag{2.21}$$

ML estimation is based on a two-steps-operation, which alternates between calculating conditional mean of the data likelihood, using data y and the current estimate of the object $\hat{f}^k$, where k is the iteration number, and then maximizing this quantity with respect to the object $\hat{f}^k$,

$$
\begin{aligned}
E - Step: \quad & Q\big(\hat{f}|\hat{f}^k\big) = \mathrm{E}\big[\ln L_y^Y(f)|y, \hat{f}^k\big] \\
M - Step: \quad & \hat{f}^{k+1} = \underset{f \in R^n}{\mathrm{argmax}}\, Q\big(\hat{f}|\hat{f}^k\big)
\end{aligned} \tag{2.22}
$$

Here, $\hat{f}^k$ is the object estimate which maximizes the likelihood function at the $k - th$ iteration with an assumption that this function is convex itself and has a maximum defined. In tomographic imaging, likelihood function is a product of large number of factors, so it is convenient to maximize its logarithm, as shown in the above relation, which will have the same maxima. Alternatively, for a negative-logarithmic expression, being strictly convex and with A and B as suitable constants, whose values depend on the noise distribution assumed, we may have a minimization problem as follows

$$\hat{f} = \underset{f \in R^n}{\mathrm{argmin}}\{-A \ln L_y^Y(f) + B\}, \hat{f} \geq 0 \tag{2.23}$$

In case of additive Gaussian white noise, this functional becomes equivalent to the Least Square approach as follows [66;101],

$$\hat{f} = \underset{f \in R^n}{\mathrm{argmin}} \|Hf + b - y\|, \hat{f} \geq 0 \qquad (2.24)$$

Advantage of the iterative techniques is their flexibility to treat realistic mathematical models of the measurements.
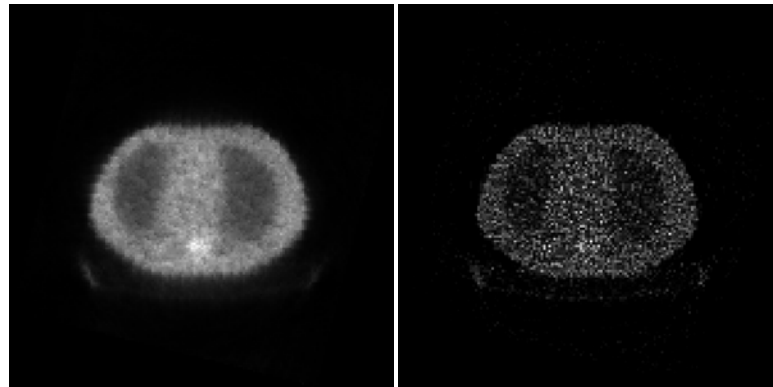
Figure 2.12: Image reconstructed using 10 iterations (left) and 100+ iterations (right) of Maximum Likelihood Image reconstruction clearly show reconstruction based noise with increasing iteration numbers.

They allow not only to account for the attenuation of radiation, but also to correct for image degradation factors, such as collimator blurring and photon scattering in SPECT [29;52;60;61;91;93;94;102;105]. Though, elegant in its mathematical formulation, iterative estimation problem is ill-conditioned due to a very high condition number of the matrix H for Poisson noise distribution. Due to this ill-conditioning of the problem, reconstructed images become too noisy and bear reconstruction induced noise known as *checkerboard noise,* since many components of the minimum are zeros [20;102;106;107]. This ill-posed problem is a starting point of the so called *Tikhonov regularization* theory [46;67;108;109]. MLEM method is capable of modeling various image degrading effects. However, because they only incorporate information available in the data and do not consider any object properties, their resultant solution images bear poor noise and resolution properties. It should also be emphasized that, with non-negativity constraint, it is not easy to treat the problem with standard regularization theory. However, regularization approach is used to overcome this problem by constraining the problem to the strictly positive solutions and additional information about the object is used to limit the solution image set [93;110;111].

2.9   Regularization

Regularization means application of a key idea to introduce a family of continuous approximations in place of a discontinuous operator [48;75]. It includes use of some priori information on the solution, which in Green's words can be put as, "it is indeed hard to imagine knowing nothing about the object" being reconstructed. Regularization is critical for successful statistical modeling of high dimensional noisy data. Regularization could be implemented implicitly or explicitly [66;67]. Some form of regularization, such as some bounds on the solution image, in form of a filter-factor to zero very small singular values or by stopping at early iterations to cease very small oscillations near convergence, is implied implicitly without explicitly defining a regularization term. Whereas, the generalized explicit form of the regularized solution, in a sense of least squares solution for example, is generally defined as [66;74],

$$\hat{f}(x,y) = \underset{f(x,y)}{\operatorname{argmin}}\{\|y - H(f)\|^2 + \lambda\varphi(f)\} \qquad (2.25)$$

Here $\lambda\varphi(f)$ explicitly defines a regularizing term in form of some priori information, known about the object before its reconstruction. This formulation is also known as Tikhonov iterative method (TIM). Here, $\varphi(f)$ is the regularization functional and λ controls trade-off between good data fit and the prior influence. Generally, smoothness imposing functionals in the form of squares of the pixel differences $\lambda(\Delta f)^2$ are used, however, they are known to blur sharp features of the reconstructed images. Some authors have introduced semi-norm of the Total Variation (TV) as the regularizing functional in the context of CT image reconstruction whereas several other prior functionals have been introduced [112;113]. We describe TV regularization below in a brief context.

2.9.1   Total Variation (TV) Regularization

If the image to be reconstructed is defined on a bounded, open and convex region Ω of $\mathbb{R}^2$ such that $f \in L^1(\Omega)$, we set,

$$TV(f) = \int_{\Omega} |\nabla f| \, dx \qquad (2.26)$$

Here, ∇f is the vector of weak partial derivatives of f and is known as weak gradient of f. This functional has been, initially, introduced by Rodin, Osher and Fatemi and further

has been used for various image processing problems [112;114]. Medical images, generally, do not contain very small structures and very small signal oscillations are due to high frequency noise. Also, these images bear visual information such as tumor boundaries as sharp discontinuities and tumor bounded areas as uniform signal regions and both of these should be reconstructed without artifacts. TV regularization scheme appears to be the relevant model for such signals as it recovers piecewise smooth areas without much blurring of the sharp edges [115;116]. TV regularization allows reconstruction of the most regular image, while better conditioning the ill-posed tomographic image reconstruction problem, and constraining it with respect to the TV semi norm, at the same time.

However, in numerical analysis, a problem of singularity arises when non-differentiable argument $|\nabla|$ becomes zero. A suggested way out is a form of relaxation by introducing a relaxation parameter η as follows;

$$TV(f) = \int_\Omega \sqrt{|\nabla f|^2 + \eta}\, dx \qquad (2.27)$$

Here η is a small positive number to avoid singularity in the derivative term. However, problem with this method is a compromise, of the advantage of boundary variation (BV) model of the TV functional, which introduces blurring of the edges in the final image. Other possible proposed methods are computation of TV without any regularization or adjustment of standard gradient descent algorithms to sub-gradient. In our work, we adopted a numerical scheme introduced in literature and computed $TV(f)$ with discrete approximation [112;113],

$$TV(f) = \sum_{ij=2}^{N} \sqrt{\left(f_{ij} - f_{i-1j}\right)^2 + \left(f_{ij} - f_{ij-1}\right)^2 + \eta} \qquad (2.28)$$

Here f_{ij} represents the $ij - th$ pixel within a 2D image. Various kinds of regularization functions are used to make the problem less ill-conditioned and to constraint the final solution towards less noisy and more acceptable versions.

The prior formulation, given in equation (2.25), provides a solution using some approximate operators, which are mainly evaluated using data, without considering statistical properties of the emission process. Whereas, it is much better to discuss the solution, with some uncertainties and confidence levels defined, because nature of the counting statistics is stochastic and various noise models should be included. Hence, it is

appropriate to deal with the regularized reconstruction problem in probabilistic framework instead of deterministic approach [46;60;69;76;77].

2.10 Probabilistic Formulation of Reconstruction Problem

Real systems produce data, which is a sampled output of an imaging system, with some discrete parameterization, including noise as a random process. Tomographic imaging system's measurements could be thought of as a realization of a random variable obeying some specific distribution law [46;66;69;72]. We discussed earlier that a direct inversion approach or solution of the linear system of equations, in least square sense, does not provide a satisfactory solution due to implied assumptions about the system or the physical processes, whereas, considering statistical properties of the counting data, it is quite natural to use statistical approach. Deterministic estimation methods are generally used to solve the problem of object estimation in image reconstruction, where, deterministic methods are those which try to estimate the solution image only on the basis of the measurements and no other information, such as noise present in the data, is considered for this reason. However, simple measurement based data space is always associated with an orthogonal null space, which makes the problem highly ill-conditioned. Bayesian approach is used to overcome this problem of noise and additional information about the object is used to limit the solution image set [65;76;77].

2.10.1 Bayesian Approach for Image Reconstruction

In essence, Bayesian approach assumes that the solution image is a random identifiable ensemble selection from a set of similar solution images reconstructed by the identical procedure [66;77;117]. In this way, some further information may be reconstructed about the object in the null space and thus may lead to an artifacts reduction. The Bayesian approach allows prior information about the reconstructed object to estimate the null-space components of the solution, whereas, several types of priori information can be incorporated. It is generally accepted that, without considering any additional information about the object being reconstructed, formulation of the reconstruction problem is highly ill-posed, as the case in ML estimation, where, we only use information about the data noise and try to estimate the unknown object from this data only. This additional information may be in form of some prescribed bounds on the solution or its derivatives [105].

These constraints may include early iteration stopping or post-reconstruction filtering the ML solution after convergence, which comprises of some sort of implicit regularization. However, we may use information given about some statistical properties of the object explicitly, which may be known before hand. If the object being reconstructed is assumed to be a realization of a random object, probability density of the data, $Y = y$ given a realization of the object $F = f$, given as $p(y|f)$ will have a different interpretation in the form of conditional probability of the random variable Y given the realization f of the random object F or $p_F(Y = y|F = f) = p_F(y|f)$. Additional information about the object is introduced in form of some probability density function of the object. This is generally known as the *prior probability density* and its given distribution is known as the *prior distribution,* because it is assumed to be known before acquisition of the data [66]. If the prior density is represented by $p_F(f)$ then the joint probability density of the random variables Y *and* F is given by,

$$p_{FY}(f,y) = p_Y(Y = y|\mathrm{F} = f)p_F(f)$$

Using Bayes formula, we obtain conditional probability density of the random object F, for a given realization of $Y = y$,

$$p_F(f|y) = \frac{p_{FY}(f,y)}{p_Y(y)} = \frac{p_Y(y|f)p_F(f)}{p_Y(y)} \tag{2.29}$$

This is also known as the posteriori conditional probability density of the object given the measurement y in terms of the conditional probability of y given f and a priori probability distributions of f and y separately. Here $p_Y(y)$ is the normalizing factor assumed to be constant, and,

$$p_Y(y) = \int p_{FY}(f,y)df$$

The a-posteriori probability density of F given f may be rearranged as,

$$P_y^F(f) = p_F(f|y) = p_Y(y|f)\frac{p_F(f)}{p_Y(y)} = L_y^Y(f)\frac{p_F(f)}{p_Y(y)}$$

Here $L_y^Y(f)$ is the likelihood function, whereas, a maximum-a-posteriori (MAP) estimate of the unknown object, obtained after considering data and the prior, maximizes this joint probability density function,

$$\hat{f} = \operatorname*{argmax}_{f \in R^n} P_y^Y(f) = \operatorname*{argmax}_{f \in R^n} \left\{ L_y^Y(f) \frac{p_F(f)}{p_Y(y)} \right\} \ with \ f \geq 0$$

It should be noted that if data is complete, then prior knowledge is useless, however in case of noisy data or incomplete data, as in image reconstruction problem, the prior information may be as much worthy as the data itself, for a feasible solution. Taking logarithm of the MAP density function, the log-posterior functional, ignoring $p_Y(y)$ would become [105;111;117],

$$\hat{f} = \operatorname*{argmax}_{f \in R^n} \{ \log P_y^Y(f) \} = \operatorname*{argmax}_{f \in R^n} \left\{ \log \left(L_y^Y(f) \right) + \log p_F(f) \right\} \qquad (2.30)$$

For optimization, above mentioned MAP formulation is derived with respect to the current pixel f_j and its derivative is set equal to zero to find the iterative update equation for estimated maxima,

$$\frac{\partial}{\partial f_j} \left\{ \log \left(L_y^Y(f|y) \right) + \log p_F(f) \right\} = 0$$

In case of Poisson noise distribution, with noiseless mean measurement vector given by $\bar{Y}_i = \sum_{j=1}^N H_{ij} f_j \ for \ i = 1,..,M$ and with constant data vector y, the Likelihood function will be $L_y^Y(f|y) = \prod_{i=1}^M e^{-\bar{Y}_i} \frac{(\bar{Y}_i)^{y_i}}{y_i!}$ and log-likelihood of the MAP estimate in this case,

$$Q(f) = \log \left(L_y^Y(f|y) \right) + \log p_F(f) = \sum_{i=1}^M \{ y_i \log \bar{Y}_i - \bar{Y}_i - y_i! \} + \log p_F(f)$$

For optimization, we need to equate the derivative to zero,

$$\frac{\partial}{\partial f_j} \sum_{i=1}^M \{ y_i \log \bar{Y}_i - \bar{Y}_i - y_i! \} + \frac{\partial}{\partial f_j} \log p_F(f) = 0$$

Solution of this equation must satisfy Kuhn-Tucker's optimality conditions of the problem for all $j = 1, .., N$, which are as follows [66],

$$\frac{\partial Q}{\partial f_j} \geq 0, \forall j$$

$$f_j \frac{\partial Q}{\partial f_j} = 0, \forall j$$

By substituting value of Q in 2nd condition we get,

$$f_j \left\{ -\sum_{i=1}^{M} \frac{y_i}{H_{ij} f_j} H_{ij} + \sum_{i=1}^{M} H_{ij} + \frac{\partial}{\partial f_j} \log p_F(f) \right\} = 0$$

$$f_j \left\{ \sum_{i=1}^{M} H_{ij} + \frac{\partial}{\partial f_j} \log p_F(f) \right\} = f_j \sum_{i=1}^{M} \frac{y_i}{H_{ij} f_j} H_{ij}$$

This relation can be rearranged to find an update equation for the optimal image estimate as follows with non-negativity condition for $\hat{f}$ still holding,

$$\hat{f}_j^{k+1} = \frac{f_j^k}{\left\{ \sum_{i=1}^{M} H_{ij} + \frac{\partial}{\partial f_j} \log p_F(f^k) \right\}} \sum_{i=1}^{M} \frac{y_i}{H_{ij} f_j^k} H_{ij} \qquad (2.31)$$

$$f_j \geq 0, for\ all\ j$$

Numerically, this equation does not have a closed form solution, however, Green proposed to use the EM algorithm for MAP estimation problem, where image update at the previous iteration is used to evaluate derivative of the prior term instead of the unknown object values and named this algorithm as One-Step-Late (OSL-MAP) algorithm [105;111;118].

2.10.2 Modeling the Priors Distribution

Model of the prior is a critical choice for the MAP estimation and is often chosen to be a markov random field (MRF) in form of Gibbs distribution function due to its simplistic application in image estimation problems. Single pixel mean and variance can be set, however, it will not present image properties in a local neighborhood. Gibbs functions have simple mathematical form and can capture local image properties. In MRF, image pixels and measurement bins are considered to be random variables and according to the Hammersly-

Clifford theorem an MRF is defined as a random field, on a lattice, if and only if, its probability distribution function corresponds to a Gibbs function [117;119]. The prior, in Bayesian approach, is generally modeled as a Gibbs distribution function, because, it provides a powerful mathematical tool to model the underlying spatial correlations of the source locations [111;120].

The probability density function for an MRF can be expressed in Gibbs form as follows,

$$p_F(f) = Ce^{-\beta V(f)} = Ce^{-\beta \sum_{N_b} V(f)} \tag{2.32}$$

Here C is the normalizing constant for the distribution, $V(f)$ is defined as the energy function because it captures relative energy of pixels in a small neighborhood in some mathematical formulation, and β is the hyper-parameter whose values define influence of the prior [121;122]. Energy functions are generally defined in a local neighborhood N_b of a pixel of interest, because they defined the energy distribution in a local neighborhood. Values of the parameter β are critical in defining final nature of the image estimate and will determine tradeoff between bias and variance of the resulting estimate. For example, large β values will produce smoother estimates with higher bias, while small values allow the estimate to approach the typically high variance solution near to its ML estimate [109].

MAP image priors have a locally finite support in a small neighborhood. Gibbs random fields (GRF) will have this property, which is computationally very attractive and may be presented as follows,

$$p(f_i|f_j, i \neq j) = p(f_i|f_j, j \in N_b)$$

Various energy functions $V(f)$ have been suggested in literature. A wrong choice of the energy function may lead to unacceptable results; therefore, one must be very careful in choosing these functions. Convex energy functions are desirable for stability and computational simplicity of the solution. A discussion of Markov random fields for MAP tomographic estimation is found in [123-125].

2.10.2.2 Quadratic (QPs) and Non-Quadratic Priors

A very common choice for the potential function is, a Gaussian MRF, which works upon square of the difference of neighboring pixels about a pixel of interest [125;126]. This choice can be expressed in the form of a prior distribution around a particular pixel f_j as follows,

$$V(f_j) = \frac{1}{2}(\Delta f_j)^2 \quad where \ \Delta f_j = (f_j - f_k) \quad \quad for \ j = 1, \dots, N \ and \ j \neq k \ and \ k \in N_b \tag{2.33}$$

Here, Δf_j represents the difference of two pixel values in a small neighborhood and, commonly, a first order (with four pixels around the centre pixel) or a second order (with eight neighboring pixels around the center pixel) pixel neighborhood is used [77;96;105]. Pixel values are penalized with reference to this difference in pixel values.

Salient image features, such as edges, are discouraged in the final image estimate due to square of the pixel differences. Huber's energy function is an example of such functions, where a threshold T parameter has been introduced to benefit edges, having pixel differences above the threshold passing through the prior without being penalized. Huber's potential function is defined as [127],

$$V(f_j) = \begin{cases} (\Delta f_j)^2 & for \quad |\Delta f_j| \leq T \\ 2T|\Delta f_j| - T^2, & for \quad |\Delta f_j| > T \end{cases} \tag{2.34}$$

Another function has been proposed by Green [105],

$$V(\Delta f_j) = 2T^2 \log \cosh\left(\frac{\Delta f_j}{T}\right) \tag{2.35}$$

Here T is a threshold value for the maximum edge pixel differences.
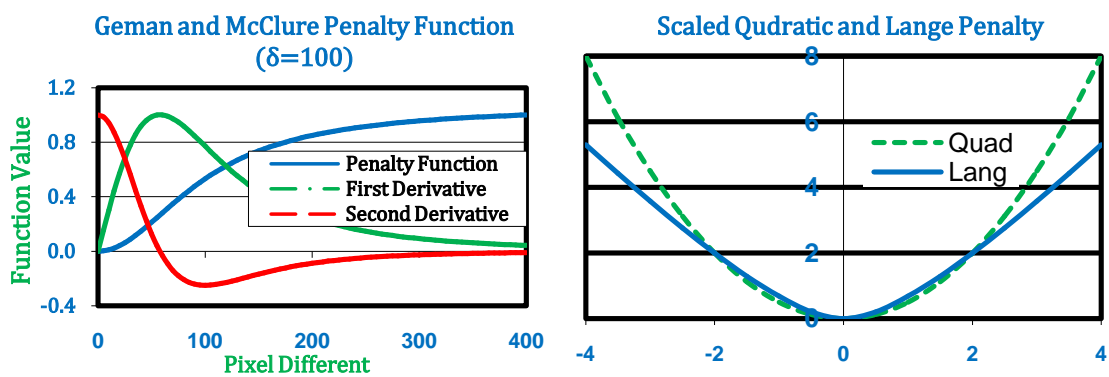
Figure 2.13: Different prior functions with their derivatives.

It is to be noted that these functions, though take care of the edges empirically, have a problem of additional parameter tuning. Also, MAP optimization problem with EM algorithm does not have a closed form solution with these prior functions; therefore,

approaches similar to EM, such as Generalized EM (GEM) or One Step Late (OSL) need to be used [77;105;111].

2.10.2.3   Median Root Priors (MRPs)

Median-Root-Priors (MRPs) as proposed by Alenius (1998), are not a full mathematical derivation of the prior distribution or its derivatives due to undefined dependence of median on the local neighborhood, but, has an intuitive resemblance to the priors distribution given by a Gaussian type PDF as follows [128],

$$p_F(f) = Ce^{-\frac{\beta}{2}V(f)} with \, V(f) = \sum_{j=1}^{N_b} \frac{(f_j - M)^2}{M} \, for \, all \, j = 1,2,\dots,N \qquad (2.36)$$

Here, M, are the Gaussian means or hyper-parameters, which depend on a small local neighborhood N_b, around pixel f_j, and need to be evaluated by the median operation as $M = med\{f_k, k \in N_b\}$. Here, log of the prior, or Gibbs type energy function is of simple quadratic form,

$$\log p_F(f) = -\frac{\beta}{2}V(f) = -\frac{\beta}{2}\sum_{j=1}^{N_b} \frac{(f_j - M)^2}{M}$$

and its empirical derivative, defined by Alenius (1998), is as follows [128],

$$\frac{\partial}{\partial f_j}V(f) = \frac{2(f_j - M)}{M}.$$

This derivative has been evaluated at the pixel f_j, while considering M as constant, which is theoretically not true, because dependence of local median is not linear on the neighborhood. It is obvious from the above relation that, when median is the center pixel and varying w.r.t. f_j, the prior vanishes. However, for median to fall upon any other pixel in the neighborhood it is constant for the sake of derivation, hence, mathematically there is no harm in considering median as constant, w.r.t. f_j, for the sake of evaluation of $\frac{\partial M}{\partial f_j}$. A depiction of this empirical description is given in Figure 2.14.

A simple description of MRPs could be that it has a Gaussian like distribution with location of the Gaussian mean as the local median [128]. Theoretical analysis of the MRPs convergence properties is not tractable because of non-availability of its analytical

derivatives. However, practically all the images reconstructed with MAP algorithm using MRPs, do converge, which has also been observed by other researchers [110]. Pixels are only penalized against the local median and not with respect to the pixel differences, when centre pixel value departs from the local median. This encourages the final image estimate towards its locally monotonic version and not its locally smooth version, however, including smoothness as a subset.
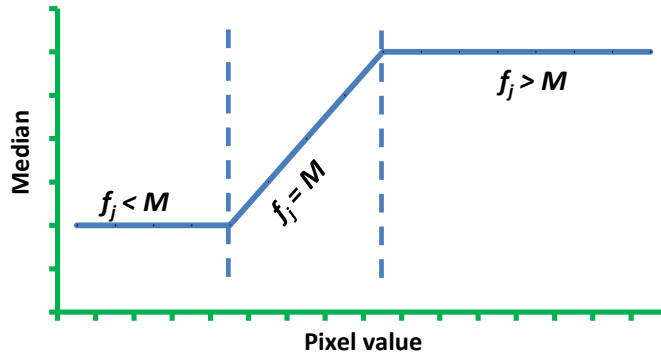
Figure 2.14: An intuitively depicted dependence of median on the pixel value in a small neighborhood. The prior vanishes when median equals center pixel (in between two dashed lines) and it is constant for all other values of median.

It means that pixel values, corrupted by noise, are compared to the local median and left unaltered if they are close enough to the median in which case that pixel is understood as uncorrupted. Noise is generally non-monotonic in a local neighborhood, instead of being locally smooth, and is penalized. Similarly, no special instructions are needed to let the prior behave differently at the edges as median follows the edge, which is equivalent to performing automatic edge preservation [107]. This is different from other quadratic or non-quadratic priors, where they need extra parameters to be tuned for edge height, and let only locally smooth areas pass through them unaltered.

2.10.2.4 One-Step-Late (OSL) Estimation with QPs, MRPs and TV Regularization

Considering OSL algorithm, from section 2.9.1, a formulation of this algorithm may be rearranged as follows,

$$
\begin{aligned}
f_j^{k+1} &= \frac{f_j^k}{\left\{\sum_{i=1}^{M} H_{ij} + \frac{\partial}{\partial f_j} \log p_F(f^k)\right\}} \sum_{i=1}^{M} \frac{y_i}{H_{ij} f_j^k} H_{ij} \\
f_j^{k+1} &= f_j^k f_j^{PRIOR(k)} f_j^{ML(k)}
\end{aligned}
\tag{2.37}
$$

Here $f_j^{ML(k)}$ is the likelihood update term and $f_j^{PRIOR(k)}$ is the prior update term of the $j-th$ pixel, at the $k-th$ iteration, and for QPs [105],

$$f_j^{ML(k)} = \sum_{i=1}^{M} \frac{y_i}{H_{ij} f_j^k} H_{ij}$$

$$f_j^{QP(k)} = \frac{1}{\left\{\sum_{i=1}^{M} H_{ij} + \beta \sum_{l=1}^{N_b} (f_j - f_k)\right\}}$$

(2.38)

Similarly, for Median Root Priors (MRPs), we have [107],

$$f_j^{ML(k)} = \sum_{i=1}^{M} \frac{y_i}{H_{ij} f_j^k} H_{ij}$$

$$f_j^{MRP(k)} = \frac{1}{\left\{\sum_{i=1}^{M} H_{ij} + \beta \dfrac{f_j - M}{M}\right\}}$$

(2.39)

It should be noted that, for the sake of derivation, M has been considered constant with respect to the pixel f_j. In case of TV regularizing functional, we will get [112],

$$f_j^{ML(k)} = \sum_{i=1}^{M} \frac{y_i}{H_{ij} f_j^k} H_{ij}$$

$$f_j^{TV(k)} = \frac{1}{\left\{\sum_{i=1}^{M} H_{ij} + \beta C(f) f^k\right\}}$$

and,

$$C(f) = \int_{\Omega} \frac{\nabla f_{i-1j} \cdot \nabla f_{ij-1}}{\sqrt{|\nabla f|^2 + \eta}} dx$$

In its discrete formulization, from equation (2.26), $TV(f)$ as an irregularity measure of the image along with its approximate derivative is defined as follows,

$$TV(f) = \sqrt{(f_{ij} - f_{i-1j})^2 + (f_{ij} - f_{ij-1})^2 + \eta}$$

$$\nabla TV(f) = C(f) \cong \frac{2f_{ij} - f_{i-1j} - f_{ij-1}}{\sqrt{(f_{ij} - f_{i-1j})^2 + (f_{ij} - f_{ij-1})^2 + \eta}}$$

(2.40)

We implemented this form of TV regularization function for a comparison of their resolution properties with QPs and MRPs.

2.11 Local Impulse Response Function (LIR)

Stayman and Fessler (1999), have developed an analytical expression for the evaluation of resolution properties of Penalized-Likelihood (PLEM) Reconstruction methods [24;129]. We adopted that LIR expression, for our analysis and comparison of resolution properties of various methods. Below is a brief mathematical derivation of this expression in the context of various prior functions.

The LIR may be defined as the limiting difference of mean reconstruction $\hat{f}(\bar{Y})$ of an image f as a function of noisy measurements mean $\bar{Y}(f)$, and mean reconstruction of its perturbed version $\hat{f}(\bar{Y} + d\delta_j)$, for a specific estimation algorithm, with a perturbation size of d added to the $j - th$ pixel and may be written for the $j - th$ pixel as follows,

$$l^j = \lim_{d \to 0} \left(\frac{E[\hat{f}(\bar{Y} + d\delta_j)] - E[\hat{f}(\bar{Y})]}{d} \right)$$

Here, $E[\hat{f}(\bar{Y} + d\delta_j)]$ is expectation of the estimated perturbed image δ_j is the Dirac impulse at the center of $j - th$ pixel and l^j represents an image of the impulse at the $j - th$ location and may be in a vector form. Taking first-order Taylor approximation about the mean measurement $\bar{Y}(f)$, and ignoring higher order terms, it comes out to be that the ensemble mean of the likelihood based estimators is approximately equal to the value one gets from applying the estimator to the noiseless data [24;106;130-132]. Hence, the above relation becomes,

$$l^j = \lim_{d \to 0} \left(\frac{E[\hat{f}(\bar{Y}) + d\delta_j] - E[\hat{f}(\bar{Y})]}{d} \right)$$

$$= \lim_{d \to 0} \left(\frac{[\hat{f}[\breve{Y} + d\delta_j] - [\hat{f}(\breve{Y})]}{d} \right)$$

$$= \nabla_y \hat{f}\left(\breve{Y}(f)\right) = \nabla_y \hat{f} \cdot \Delta_f \breve{Y}(f) \qquad (2.41)$$

Here $\breve{Y}(f)$ is the noiseless data, $\nabla_y = \left[\frac{\partial}{\partial y_1}, \frac{\partial}{\partial y_2}, \dots, \frac{\partial}{\partial y_M} \right]$ is a vector of partial derivatives and $\Delta_f \breve{Y}(f)$, is variational derivative with respect to the object. For MAP estimators, we have an estimate $\hat{f}$, from equation (2.30) as a maximizer of the posterior objective function in implicit form as follows [133],

$$\hat{f} = \underset{f \in R^n}{\text{argmax}} \, \rho(f, y) = \underset{f \in R^n}{\text{argmax}} \left\{ \log\left(L_y^Y(f)\right) + \beta \log p_F(f) \right\} \tag{2.42}$$

Maximizer of this function should satisfy Kuhn-Tucker's second condition of optimality and, if we ignore the condition for non-negativity for the time being,

$$\nabla_f \rho(f, y) = 0, \forall \, f$$

Differentiating again with respect to y we get,

$$\nabla_{ff}^2 \rho(f, y) \nabla_y f + \nabla_{fy}^2 \rho(f, y) = 0$$

Here ∇_{ff}^2 and ∇_{fy}^2 are the matrix gradient operators having partial derivatives with respect to the first and second variable of the implicit function defined above. Assuming that $-\nabla_y \rho(f, y) > 0$ *and* replacing $y = \bar{Y}$, we get,

$$\nabla_y \hat{f} = \left[-\nabla_{ff}^2 \rho(\hat{f}, \bar{Y}) \right]^{-1} \nabla_{fy}^2 \rho(\hat{f}, \bar{Y})$$

Substituting this value of $\nabla_y \hat{f}$ in equation (2.41), the linearized local impulse response (LLIR) will be,

$$l^j = \left[-\nabla_{ff}^2 \rho(\hat{f}, \bar{Y}) \right]^{-1} \nabla_{fy}^2 \rho(\hat{f}, \bar{Y}) \nabla_f \bar{Y}$$

Using objective function defined in equation (2.42) and noting that $\nabla_{fy}^2 \left(\log p_F(f) \right) = 0$,

$$l^j = \left[-\nabla_f^2 \left(\log\left(L_y^Y(f)\right) \right) + \beta \nabla_f^2 (\log p_F(f)) \right]^{-1} \nabla_{fy}^2 \left(\log\left(L_y^Y(f)\right) \right) \nabla_f \bar{Y} \tag{2.43}$$

This equation defines LIR in terms of partial derivatives of the implicit MAP estimator. For a special case of ECT, mean measurements are related to the object as follows,

$$\bar{Y}_i = \sum_j H_{ij} f_j + b_i \tag{2.44}$$

$$\log\left(L_y^Y(f)\right) = \sum_i y_i \, log \, \bar{Y}_i - \bar{Y}_i \tag{2.45}$$

$$\nabla_{ff}^2 \left[\log \left(L_y^Y(f) \right) \right] = \sum_i \left(\frac{y_i}{\overline{Y_i}^2} \right) \nabla_{ff}^2 \, \overline{Y_i} - \sum_i \left(\frac{y_i}{\overline{Y_i}} - 1 \right) \nabla_{ff}^2 \, \overline{Y_i}$$

Partial derivatives of the likelihood function with respect to the first and second variable are as follows,

$$\nabla_{ff}^2 \left(\log \left(L_y^Y(f) \right) \right) = H^t diag \left\{ \frac{y_i}{(\overline{Y_i})^2} \right\} H$$

$$\nabla_{fy}^2 \left(\log \left(L_y^Y(f) \right) \right) = H^t diag \left\{ \frac{1}{\overline{Y_i}} \right\}$$

Also, note that $\nabla_f \overline{Y} = He^j$ where e^j is the unit vector having 1 at the $j - th$ location. Substituting all these values back into the relation (2.43), we can write LIR as follows for emission tomography,

$$l^j = \left[H^t diag \left\{ \frac{y_i}{(\overline{Y_i})^2} \right\} H + \beta \ddot{R}(f) \right]^{-1} H^t diag \left\{ \frac{1}{\overline{Y_i}} \right\} He^j$$

$$l^j = \left[H^t diag \left\{ \frac{1}{\overline{Y_i}} \right\} H + \beta \ddot{R}(f) \right]^{-1} H^t diag \left\{ \frac{1}{\overline{Y_i}} \right\} He^j \tag{2.46}$$

Here $\ddot{R}(f)$ is Hessian of the prior function. This equation defines the local impulse response function (LIR), which we have used extensively in our work in order to evaluate and compare resolution properties of various priors.

2.12 Summary

A discussion of emission tomography physics, with reference to PET and SPECT has been presented, in this chapter, for various types of data acquisition and system models. Various image degrading effects have been discussed which ultimately degrade final image quality and consequently make reconstructed resolution non-stationary and cause a signal loss in form of PVE due to limited resolution capabilities of these systems [6;11;14;19;23;28;41;61;93;94]. Asymmetry of these effects across the FOV and noise in the data with its incomplete nature make the mathematical image reconstruction problem ill-posed. We discussed different approaches, for example implicit or explicit regularization techniques, to solve the ill-posed reconstruction problems in the context of their capabilities to control final reconstructed resolution and noise [46;109;134;135]. We argued that explicit regularization methods, such as MAP or PLEM reconstruction methods

have better control over the final reconstructed resolution through a use of penalty or prior distribution functions as compared to the other methods [66;95;105;111;125]. Different prior functions have been proposed to reconstruct images bearing specific characteristics depending on the selected priors [77;105;121;128;129]. A brief description of the requirements and capabilities of different reconstruction approaches is given in Table 2.1. This table indicates that analytical reconstruction methods do not take care of the ill-conditioning of the problem due to noisy and incomplete data whereas they are much faster as compared to the iterative and statistical reconstruction methods.

Table 2.1: Comparison of different reconstruction methods for their resolution control and other characteristics such as edge preservation, ill-posedness and additional parameters required.

Reconstruction Method	Ill-Posedness	Conv. Speed	Edge Preservation	Prior Used	Resolution Uniformity	Parameters Required
Analytical Reconstruction						
Direct Inversion	Yes	Fast	Smoothed	No	Uniform	No
Fourier Reconstruction	Yes	Fast	Smoothed	No	Uniform	No
Filtered Backprojection	Yes	Fast	Smoothed	No	Uniform	No
Iterative Reconstruction						
Least Square	Yes	Fast	Smoothed	No	No	No
Algebraic Reconstruction	Yes	Fast	Smoothed	No	No	One
Conjugate Gradient	Yes	Slow	Smoothed	No	No	One
Maximum Likelihood	Yes	Slow	Smoothed	No	No	No
Reg. Least Square	Less	Slow	Smoothed	Yes	No	One
Statistical Iterative						
MAP-QPs	Less	Mod	Smoothed	Yes	Controlled	One
MAP-NonQPs	Less	Mod	Preserved	Yes	Controlled	More than One
MAP-MRPs	Less	Mod	Robust	Yes	Controlled	One
MAP-TV	Less	Mod	Robust	Yes	Controlled	More than one

Similarly, analytical methods produce images with almost uniform resolution for space-invariant systems, however, they do not consider any underlying noise distribution and their ability to include various system models is limited [84;86;86;88;122;136]. Simple

iterative methods, without regularization, cannot compensate for ill-conditioning of the reconstruction problem and produce reconstruction based noise because they use information embedded in the data only and do not use any available priori information about the object [105;111;125]. Their convergence is slow and low frequency content is superimposed by high frequency noise if large number of iterations is used, whereas their resolution control is poor [98;100;120;134;137].

Statistical reconstruction methods, with explicit regularization included in form of QPs, require only one parameter to be tuned and have better control on the reconstructed resolution, however, their reconstructed images have anisotropic smoothing characteristics with blurred and de-shaped regions. Non-quadratic regularization techniques need extra empirical parameters to define edges and like TV priors produce patchy artifacts even in uniform activity regions [26;30;60;127;138].

Regularized image reconstruction MAP methods, based on MRPs, require only one empirical hyper-parameter; have robust edge preservation, better resolution control, lower blurring nature and moderate convergence speed [30;107;110;139;140]. They have a problem of analytical description of their convergence properties like that of TV priors, however heuristic approaches are available for the solution. Hence, we described, in this chapter, a brief derivation and modeling of the priors based on quadratic, TV and MRPs based priors in the context of OSL-MAP reconstruction algorithms for image reconstruction [107;112]. We have also presented a brief derivation of the LIR expression, including these priors, used for the valuation and comparison of resolution properties of the images reconstructed by these priors. In rest of the thesis, an exhaustive analysis and comparison of resolution properties of these priors has been presented along with a comparison of their activity recovery performance. Our objective is to find the best available prior distribution function in MAP reconstruction algorithms if uniform resolution characteristics across the whole reconstructed image are desirable.

CHAPTER 3

Literature Review

In PET, SPECT or CT, final reconstructed images are expected to depict underlying activity concentration (in PET, SPECT) or attenuation distribution (in CT) inside the object being imaged [4;141-143]. Clinical community assesses these images in two different ways, namely, qualitatively and quantitatively. Different figures-of-merit (FoMs), depending on the task and requirements of the study being carried out to measure quality of the images, are used [27;144]. The most commonly used metrics include spatial resolution, contrast recovery coefficients, absolute activity values and standard deviation (noise) images etc. Spatial resolution expresses the ability of an imaging system to distinguish between two smallest separable structures, inside the object being imaged, and is an important evaluation criterion for the comparison of different images [22;50;65;145]. Images can only be compared to each other, or various image processing tasks such as segmentation or registration or feature recognition can only be performed accurately, if they have matched reconstructed resolution characteristics [24;29]. Finite reconstructed resolution of these systems depends on many physical or estimator dependent, image degrading effects and it is very difficult to obtain images bearing uniform and matched resolution characteristics [6;10;60;141]. Also due to many noise processes present in emission and detection processes, a compromise is always needed for a trade-off between resolution and noise which ultimately depends on the reconstruction method or model used. In this chapter, we reviewed image formation process, causes of image quality degradation and non-uniform reconstructed resolution, various image reconstruction methods, their resolution properties and methods to compensate for resulting non-uniform resolution properties of images reconstructed by different methods.

3.1   Introduction

Analytical image reconstruction methods, such as filtered backprojection (FBP), Fourier reconstruction (FR), and convolution backprojection (CBP), are the reconstruction

methods based on an inversion of the assumed line integral model of the projection data and work well for space-invariant systems [60;86-88;146]. For space variant systems response, these methods ignore any underlying noise distribution and have limited capability to model various image degrading effects and their reconstructed image bear degraded noise and resolution properties [61;104;122;126]. Simple iterative methods, such as ART or SART, try to solve analytical line integral model numerically, as a set, of linear equations without any modeling of the projection process or the object properties, while considering the object as a linear combination of parameters to be estimated, hence, cannot fully exploit imaging physics properly [39;60] and lead to images with lesser than optimized quality [56;79;99]. Methods based on simple modeling of the statistical nature of the data, such as simple likelihood based method or methods based on least squares data modeling; result in noisier images with increasing iteration number due to ill-condition of the mathematical formulation of the reconstruction problem [23;28;93]. These methods try to fit the solution image to the data only, which is noisy in nature, and this noise gets amplified because of very small singular values of the forward model matrix [102, 106].

Several methods based on the concept of restricting or constraining smallest singular values, known as implicit or global regularization methods such as early iteration stopping or post-smoothing of the fully converged MLEM image, are employed to reduce this reconstruction based noise, because these images still have better noise properties as compare to the analytical methods [104;147;148]. Resultant images may have better noise properties, however, their overall resolution and noise characteristics depend on the number of iterations, the sieve or the filter used for post-filtering, with least resolution control and much longer convergence times [24;95]. Modeling various image degrading effects may improve bias and variance of the reconstructed images, however, images may still suffer from reconstruction based noise due to ill-conditioning of the problem. Another feasible approach is to use some explicit regularization technique to overcome this iteration based noise. Methods proposed in the framework of Tikhonov Regularization are Penalized-Likelihood Expectation Maximization (PLEM) reconstruction methods or Maximum-a-Posterior (MAP) reconstruction methods in Bayesian framework [50;111;117]. Explicit regularization allows inclusion of a priori knowledge about the object distribution properties and helps conditioning the reconstruction problem. Arbitrary regularization can be applied to obtain user defined resolution properties of the reconstructed images, which provide extra resolution control [109;129;135]. Regularizing functionals may be added as penalty functions in PLEM framework or the prior distribution functions in Bayesian sense. These regularization functions are also termed as local

regularization methods, because they are generally based on Gibb's prior distribution functions and work on a small neighborhood vicinity of a pixel of interest [66;109].

Most commonly used penalties or priors are the smoothness priors or the edge preserving priors [24;97;108;148]. Simplest form of smoothing priors, Quadratic prior functions, have been used as conventional regularization choice due to their implementation simplicity; however, they result in images with non-uniform and asymmetric resolution properties across the FOV, even for approximately shift-invariant systems, such as PET near the centre of the scanner, because they lead to an estimator with highly non-uniform and asymmetric response [26]. This is due to the non-uniform smoothing induced by this type of regularization functions, which results from various object dependent, such as non-uniform attenuation distribution, and system dependent factors, such as non-uniform detector response function (DRF) across the field of view in PET [6]. This induced non-uniform smoothing, or consequently non-uniform and asymmetric resolution, properties produce shape deformations in the reconstructed images and affect image quantification and make other processing tasks difficult [29]. A serious attempt to correct for these non-uniformities and asymmetries, in response function, induced by QPs in MAP methods, has been presented in [24;129;138]. A correction scheme for interactions between data term and the prior term has been introduced, which effectively generates locally modified space-variant hyper-parameter values and provides increased uniformity in resolution, based on local certainty with quadratic regularization, however, asymmetry still persists [129]. This behavior of QPs is due to their strong smoothing behavior, which increases with higher intensity differences, especially at the edges. Edge preserving regularization functions provide a way to compensate for this discrepancy and median root priors (MRPs) have a robust ability to preserve edges, though they have theoretical problems in defining their derivatives [107]. Total Variation (TV) regularizing functions are another edge preserving priors with the same theoretical issue, however, their resultant images bear reasonable properties [112;114;116;149;150]. These priors are non-quadratic functionals and bear heavier ill-conditioning as compared to the QPs and take more time to converge.

We have implemented MRPs and TV priors based MAP algorithms with an analysis of their resolution properties as compared to QPs, by an implementation of these functionals in Local Impulse Response (LIR) expression. We have also introduced a correction scheme for non-uniform spatial resolution based on an alternate prior functional, with and without certainty based term. We use an edge-preserving MRPs based non-quadratic regularizing prior, in this scheme, to correct for the above mentioned interactions between data and the prior term [108;110]. Our correction scheme is based on an intrinsic property of MRPs that

they penalize pixel values with respect to the local median, and their behavior is non-linear, which simulates behavior of local certainty type correction method. Also, MRPs have a robust edge preserving characteristic, without any additional parameter required, and they can be run to any number of iterations without adding much noise to the final image. In the following sections, we present a review on tomographic image reconstruction methods, ill-posedness of the image reconstruction, methods to correct for this, non-uniform resolution properties of the reconstruction images and the use of MRPs for the recovery of non-uniform resolution and their activity recovery performance in MAP reconstruction algorithms for histogram and list-mode data.

3.2   Tomography Imaging and Reconstruction Methods

Medical imaging systems try to recover distribution of some property, such as non-uniform object attenuation as in CT or radioactive emission density proportional to the non-uniform activity distribution, based on administered activity. These systems acquire data around the object, known as projection data, which is mathematically represented as Radon Transform or Attenuated Radon Transform, more precisely [45;81;82]. Two very important factors, which influence the final outcome from these systems, are the resolution of the final image and the noise present in it. Resolution can be optimized by accurately modeling acquisition and detection processes, whereas, noise may be limited by modeling emission process by modeling the object itself. These models are generally implemented through the reconstruction algorithms used to reconstruct distribution of these properties inside the object, in-vivo [66;97;151]. For acquisition and detection processes modeling, various image degrading effects which influence image quality at each of the steps from administration of the activity to the reconstruction scheme used need to be modeled into the system. Analytical reconstruction method have limited ability to model these effect, however, iterative methods can model these effects into the system model.

3.2.1   Image Degrading Effects

Disappearance or escape of the emitted photons, due to absorption or Compton scattering, out of the line of detection is termed as attenuation, which signifies a loss of true signal [8;15]. In SPECT, this effect is more complicated, due to its dependence over depth inside the object. Some sort of transmission scan is performed to generate attenuation distribution map to further apply it as a correction into the system model or reconstruction method [4;103;103;152]. Scattered photons, detected out of the line of their emission, add

blurring to the acquired data [7;9;19;141]. Numerous energy window-based, and model based scatter correction, methods have been proposed for PET or SPECT system [10]. These methods, however, do not remove 100% of scattering from the measured data. Attenuation is easier to handle in PET due to its independence over depth of interaction as compared to SPECT. Accidental coincidences are another concern in PET system [20]. A delayed coincident timing window is used to accumulate these random events which can be subtracted from the acquired data before reconstruction [20;153].

There are other detector based effects that influence event localization, which is a crucial measurement, of an emitted photon in ECT during the detection and acquisition processes. Scintillation blur, detection blur up to the finite size of the small detectors, crystal penetration effects and variations in individual detector performance, all contribute to variations in detector response and are known as detector sensitivities [4;5;13;154]. These detector sensitivities can be accounted for by performing normalization scans in PET or uniformity correction maps in SPECT [11-13].

3.2.2 System Modeling

To achieve accurate quantification and lesser image artifacts, all the above factors need to be addressed, however, some of the above effects are generally ignored by the system models used, for the sake of speed, implementation simplicity and storage requirements. Different approaches have been devised to simplify modeling of the above factors. Though inclusion of these factors into the system model drastically overburdens computational and storage resources, Mumcugolo et al., 1997 proposed a very popular factorized system matrix model in which depth dependent geometric sensitivity, photon pair non-co-linearity, attenuation, intrinsic detector sensitivity, non-uniform sinogram sampling, crystal penetration and inter-crystal scatter are modeled with system geometry, object non-uniform attenuation and other effects to improve system model accuracy [23;34;141]. By accurately modeling these probabilities spatial distortions can be minimized and certain assumptions are generally made for real time reconstruction speeds in clinical environment. Though, it is known that complete and accurate system modeling should produce images with better quality, fully accurate modeling of the system matrix makes a full project in itself [52;155]. Even, with complete modeling of the physics of various effects into the system model, image reconstruction problem is still an ill-posed problem in its mathematical formulation due to incomplete and noisy data [52;64;93;94]. Small changes in the input data may produce very large and unacceptable changes in the resultant image and leads to noisier image [67;70;75;102].

3.2.3 Geometric System Model

Iterative reconstruction methods are based on a linear model, which relates acquired data to the unknown source distribution, through a projection matrix, also known as system matrix or probability matrix [23;53;61;156]. Each element of this matrix models probability of an event emitted in a particular pixel (voxel in 3D) and being detected at a certain location inside the detector. This reduces basic image reconstruction problem, into a simple iterative estimation method, to find an approximate solution of a set of linear equations [98;119;122]. Line intersection length of a pixel, with a zero width line, through the centre of the LOR is a typical approximate model used to calculate these probabilities [53]. Further improvements have been proposed to reduce relative calculation time for the line and pixel intersection lengths [57-59;155]. Another very popular model approximation is to use intersection area of a pixel of interest and the strip (in 2D) or tube (in 3D) joining the two detectors in PET, or a diverging strip starting at detector surface and passing through the pixel of interest in SPECT, which is considered to be more accurate as compared to the line intersection length model, because, it can cover the whole pixel area [54]. It should be noted that simple geometrical system model is not sufficient for accurate system modeling and other physical and detector based image degrading effects need to be modeled [23;52].

3.2.4 Analytical and Iterative Reconstruction Methods

Analytical methods, based on some inversion scheme of the simple line integral model, such as FBP, FR and CBP, are well suited for space-invariant imaging systems. These methods lead to fast reconstructions and reconstructed images have almost uniform resolution properties across the FOV for space-invariant systems [24;29]. However, for space variant systems these methods have limited quantitative accuracy, because, they use implicit assumptions about the system model and ignore any degrading factors which results the data to deviate from line integral model. Also, they do not account for statistical nature of the event counting or any underlying noise distribution [84;86;88;129;138]. Resultant reconstructions have inferior quality, bear various artifacts such as streak artifacts in FBP images, cannot account for non-negativity constraint for the emission process and produce added noise. Post-filtering is generally used to reduce noise, which has the least control over reconstructed resolution only through the choice of filter parameters used. These filters are generally space-invariant and cannot account for various space-variant image degrading effects present [39;60;90]. Simple iterative methods, such

as Algebraic Reconstruction Techniques (ART) by Gordon et al. 1972, present a class of numerical methods to solve a set of large sparse systems and try to approach the analytical problem numerically. Several excellent reviews were given by Censor and Zenios [79;92;99;157]. These methods simple follow the line integral model; ignore any underlying noise distribution or nonlinear image degrading effects and produce images with inferior quality.

3.2.5   Statistical Iterative Reconstruction Methods

Statistical iterative methods take care of the statistical nature of the data counting and model data noise which is generally considered to be Poisson. These methods became a very hot subject for research community with appearance of a paper by Shepp and Verdi (1982), for a detailed derivation and description of Maximum-Likelihood Expectation Maximization (MLEM) reconstruction method [99]. This method was a start of an era of statistical methods due to their ability to include system related and other physical models for acquisition and reconstruction processes and produce images with better noise characteristics. However, because of slow reconstruction speed because of slow convergence of high frequency components, and limited computer resources available at that time, inclusion of full system model was a problem.

There have been many efforts to increase the speed of convergence for this algorithm where most popular of these is Ordered-Subset EM reconstruction method (OSEM). This algorithm divides data into disjoint or mutually exclusive subsets and final image is evaluated using each subset sequentially [158]. Convergence speed of this algorithm is faster, approximately, the same number of times, than MLEM, as the number of subsets. It is attractive and very popular variant of MLEM, due to its fast convergence rate, however, it does not converge to the same solution as ML-EM. Convergence point depends on the number of subsets or the number of iterations used or even on the initial image [98;137;159]. Many researchers have tried to get convergent variants and convergence may be achieved through an appropriate choice of relaxation parameters, though resolution properties of these algorithms are not very well understood, and will also depend on these parameters [134;160]. There is no consensus in the choice of subsets or the number or subsets, too.

Kaufman has shown that MLEM algorithm is a kind of steepest ascent optimization method and other optimization methods, such as Conjugate Gradient (CG) or Least Squares (LS) method, can alternatively be used to reconstruct images from projection data [161]. Pre-conditioned conjugate gradient (PCCG) methods and least squares method with

Gaussian noise models have extensively been used by many researchers and have been shown to converge faster than MLEM [100;101]. Some researchers have used single pixel update strategy, instead of updating whole image at a time, as in iterated coordinate ascent (ICA) method, and these methods have been shown to converge faster than MLEM [119]. There is another class of reconstruction methods known as optimization transfer methods [162]. Instead of maximizing non-linear set of equations having no closed form solution, other functionals can be added, which guarantee maximization of the original function, if they are maximized. This may result in a closed form solution. SAGE algorithms are a class of these types of algorithms. They use hidden data spaces with respect to the original data sets [133;163], however, their development and analysis is confined to speed up the reconstruction and their resolution characteristics are not very well known. In all these methods, mentioned above, stress was to increase convergence rate or to get the converged solution with no serious effort made to exploit or control resolution properties of these methods. Similarly, these methods only consider data modeling and try to fit the final image to the data at best, which is noisy in nature; hence, lead to images with reconstruction based noise due to ill conditioning of the reconstruction problem.

3.3   Ill-Posedness of Image Reconstruction Problem

MLEM type methods are expected to produce images with uniform resolution characteristics, if allowed to fully converge with complete system matrix modeling, however, they need large number of iterations before convergence can be achieved [104;147;161]. Unfortunately, simple ML problem, in ECT, is highly ill-conditioned, mathematically, and reconstructed images get noisier as we continue increasing the iteration number due to incomplete data and noise. Images exhibit high spatial variance and image features are overcome by the induced noise [17;72;164]. In Hadamard sense, solution image is not unique or may discontinuously depend on the data. This is because of very small singular values of highly ill-conditioned system matrix. Several implicit regularization techniques have been proposed, such as stopping the reconstruction before convergence, post-filtering the fully converged MLEM images or methods of Sieves, which in essence try to get rid of these very small singular values [95;147]. However, these methods are generally space-invariant and induce bias towards a uniform starting guess image [29]. These methods have either no or very least control over reconstructed image resolution. Additional constraints are needed to limit the set of solution images. These constraints are generally implemented in form of an additional function, describing object

properties in form an object distribution function, and are generally referred to as explicit regularization methods.

3.3.6   Explicit Regularization Techniques

Explicit regularization simply means to include object distribution properties, along with data distribution function, as part of a cost function which is optimized to find the final reconstructed image. In Tikhonov regularization framework, key idea of explicit regularization is to introduce a continuous approximation of a non-continuous operator and is known as Penalized-Likelihood Expectation Maximization (PLEM) reconstruction method in penalty function framework [71;75]. This approach is equivalent to add a penalty term to the likelihood function and then to maximize this modified objective function [96;118]. An explicit form of regularization, to overcome the problem of ill-conditioning, can be implied in form of a prior distribution probability along with the likelihood in Bayesian framework and is, generally, known as Maximum-a-Posterior (MAP) reconstruction algorithm [77;111;117]. This prior function is used to satisfy the data and to include any prior knowledge available about the object being reconstructed and may be a generalized image description based function or an anatomical image of the object being imaged [93;111;122]. A very popular choice of theoretical image description is based on a property of images derived from morkov-random-fields (MRF) as Gibbs distribution function. This function works on a very small local neighborhood of image pixels assuming that images are locally smooth [111;125]. Hence, most favored regularization choice is that of smoothness priors or penalty functions based on piece-wise pair differences of pixels in local neighborhoods of an image [24;26;138].

3.3.7   Prior Distributions

Smoothness priors work on a basic image description that images are locally smooth and are generally applied in form of Gibbs distribution priors. Quadratic regularization priors, based on pair-wise pixel differences, have been most advocated and analyzed as smoothness priors in MAP reconstruction methods due to their simple implementation and good smoothing properties to reduce noise. However, these priors cause an over smoothing at regional edges and high count areas in the image, because their smoothing behavior is spatially non-uniform and depends on various factors such as activity concentration, system geometry, and non-uniform attenuation. Fessler (1996), has shown that QPs produce over smoothing in high count regions and consequently, images bear spatially-

variant resolution properties with poor resolution in these areas [24;26;129;138;148]. Difficulty in hyper-parameter tuning is another drawback of MAP reconstruction methods, because, this parameter unlike cut-off frequency in FBP, does not have any units and is difficult to evaluate. Smoothing heavily depends on this parameter and several methods have been proposed to tune this parameter much like a tabulation of cut-off frequency against resolution [26;126]. It has also been shown that effective parameter value for QPs is spatially non-uniform and depends on local certainty, though, impulse response is independent of the object intensity values, because Hessian of QPs becomes independent of the object.

Interestingly, non-uniform resolution is not specific to QPs only and, for non-quadratic priors; local resolution may not only depend on the smoothing parameter but also on object through Hessian of the prior term. However, this dependence, somehow, is also desirable such as in edge preservation. Non-quadratic priors, in general, require more than one parameter to be tuned which is a tedious problem [107;111;125]. The quadratic and non-quadratic (excluding MRPs) priors work on a basic description of the images that they are locally smooth and try to penalize pixel differences without any respect for basic image features, such as edges, where pixel differences are highest [77;121]. This results in an estimator form which drags the final image towards its locally smooth version. Hence, these estimators result in images with non-uniform and asymmetric resolution properties.

3.3.8   Edge Preserving Priors – MRPs and TV

Quadratic regularization blurs edges and induces low resolution in high count regions, whereas, to avoid this problem an edge preserving non-quadratic regularization may be used [77]. Several edge preserving techniques have been proposed. However, either these methods use non-quadratic regularization (other than Median Root Priors - MRPs) such as Huber and Lang's penalty functions or they are computationally intensive and use complex edge defining techniques such as deterministic annealing or the method of level sets [77;120;127]. Also, these methods have only been implied to improve edge preservation without addressing the problem of non-uniform resolution and, generally, use more than one empirical parameter to define edges [134;135].

Median Root base Priors (MRPs) have a robust property to preserve edges [107;128]. This is mainly due to the fact that MRPs assume that images are locally monotonic and median follows the edge. Alenius et. al., (1998) documented several advantages of MRPs, such as lesser quantification errors because of noise suppression and automatic edge preservation without additional parameters required [128]. MRPs do not induce noise with

proceeding iteration number and virtually can be iterated to any feasible number of iterations. Our results have shown that reconstructed resolution with MRPs is less sensitive to the hyper-parameter value, which is an advantage in MAP reconstruction methods [30].

We gained motivation for our analysis and design to use MRPs by Alenius et. al. (1998). They proposed non-quadratic regularization based on these priors and assumed a Gaussian-like distribution for their prior function about the median taken as its mean in a local neighborhood [128;165]. Their proposed reconstruction algorithm may be thought of as a generalization of one-step-late (OSL) variation of PLEM methods by Green [105]. There are certain drawbacks of using MRPs for example there are no straight forward analytical derivatives available for MRPs due to their nonlinear dependence in a local neighborhood and one has to resort to an empirical definition, because response of the system in MAP methods depends on Hessian of the prior function [107;112].

Hsiao et. al., (2003), have discussed analytical behavior of MRPs in detail and propose their own prior function based on an approximation to absolute function, because optimized absolute function in a local neighborhood turns out to be the local median [110]. They defined an auxiliary field of variables, in registration with local medians, for minimization of their suggestive objective function and claim that their posterior is a true joint estimation due its analytical derivability. Interestingly, even though the convergence properties of MRPs are not very well known, still they pointed out that, all the images they tried with MRPs converged. Their method results in images that bear same properties as images reconstructed by MRPs and the same has been observed by us [30]. Hence, in our point of view, it is more a matter of theoretical description and we used MRPs in our analysis borrowing heuristic derivatives while leaving their convergence properties as an open question. Another class of prior functions, having same problem with their analytical derivatives, is the TV regularizing functional [112;149]. Even with theoretical issues, these priors have been vastly used in image restoration problems with acceptable results. We have also compared TV regularizing functionals in our studies and compared them with QPs and MRPs.

3.4   Non-uniform resolution compensation

A serious effort to thoroughly investigate user controlled resolution properties with QPs is presented in [29]. An analytical expression has been developed for QPs to evaluate impulse response of the system and further to evaluate resolution properties of their MAP estimators. A local certainty based method has been proposed including QPs to obtain images with almost uniform resolution properties through a calculation of space-variant

penalty coefficients. This method, effectively, provides a way to calculate spatially-varying parameter values to obtain almost uniform resolution properties across the FOV.

3.4.1   Modified Priors and Combined Priors (ModMRPs and CPs)

Several publications describe implementation and evaluation of MRPs based regularization in MAP image reconstruction to reduce noise [31;63;107;110;139;165]. However, no serious effort, up to our knowledge, has been made to evaluate resolution properties of MRPs in comparison to the quadratic and non-quadratic priors. Qi and Leahy, (1999) have developed expressions to examine spatial resolution and variance properties of MAP reconstructed PET images [50]. They derived expressions for local impulse response contrast recovery coefficients (LIR-CRC) and variance for each voxel and, then, used these results to evaluate an effective parameter value for each voxel. Their work is based on quadratic regularization and, we have extended almost the same approach with MRPs [30]. They have also shown that noise performance of MAP estimators with QPs and post-smoothed filtering methods is almost similar and choice of a particular estimator should be based on some other factors, such as convergence speed. A very recent work in this regard has been presented by, Ahn et al., (2008), for an analysis of resolution and noise properties of the non-quadratic regularizers [132]. They mentioned about limited literature to understand quantitative properties of non-quadratic regularization and proposed a local perturbation response (LLPR) to analyze these properties, with an expression to evaluate resolution and variance. They, too, have based their design on quadratic regularization for which results are much analogous to our ModMRPs. Most of their development resembles our work which was published in Lecture Notes in Computer Science [30]. Fessler and Rogers (1996), suggest a certainty based penalty design for quadratic regularization in MAP estimators to induce almost uniform reconstructed resolution across the FOV [24]. They noted that a constant hyper-parameter value results in spatially-variant resolution properties with MAP estimators including QPs for Poisson data and, hence, proposed a way to effectively produce spatially-variant parameter values to induce spatially-uniform resolution characteristics across the image. In other words, this method corrects for non-uniformly induced resolution by evaluating space-variant coefficients for QPs. Certainty based modified penalty coefficients increase the effective parameter value in high count regions to compensate for higher smoothing. Resembling this behavior, we propose the use of nonlinearity of MRPs in MAP estimators as a mean to correct for this non-uniform behavior of the prior. We suggest MRPs based regularization scheme to obtain almost uniform resolution properties. Similarly, relying on certainty based modification for QPs,

we introduced ModMRPs in this work, to obtain uniform resolution properties of the reconstructed images.

We introduced several new median based priors and evaluated their resolution properties in detail with an analysis of their ability to compensate for non-uniform resolution properties, induced by standard uniform space-invariant QPs [24;26;29]. We have also developed hybrid priors based on QPs and MRPs and have shown that they offer fine resolution tuning in between of the ingredient priors [30]. Elsewhere, Fessler et. al., (1996), presented exploration of a modified penalty framework for non-quadratic edge preserving priors to achieve a uniform local step response, and an idea almost resembling to our work was proposed as future work [29]. This work presents resolution characteristics of MRPs, which is a form of non-quadratic edge-preserving regularization, in a modified penalty frame work to condition the reconstruction problem and to obtain almost uniform resolution characteristics [30]. We hope our work would be a step forward towards an understanding and use of MRPs, in the form of our proposed priors or any other new derivation, for the reconstruction of tomographic images with better quality.

3.4.2   Noise Analysis

Statistical iterative methods reconstruct images while trying to fit it to the data [91]. In real systems, data are noisy and consequently reconstructed images are noisy. Even with accurate system model, resultant images are still noisy because of incomplete and noisy data. In addition to accurately modeling of acquisition and detection processes one needs to model emission and object properties to optimize resolution verses noise trade off [17;133;164;166]. Different methods have been proposed to reduce noise and their noise properties have been evaluated [95;147;148]. Wilson et. al. (1994), have investigated propagation of noise into the images reconstructed with linear reconstruction methods such as FBP [131]. Approximate expressions have been developed by, for example Fessler et. al. (1996) proposed method to calculate mean and variance, for implicitly defined expressions, of images reconstructed by PLEM methods [166]. However, their expression assumes fully converged solution and is not valid for iteration stopping criteria. Barrett *et. al.*, (1994), have developed analytical expressions for the calculation of mean and variance of images reconstructed using MLEM reconstruction methods [106]. Similar efforts have been done for regularized MLEM reconstruction methods [167]. A number of figures of merit have been proposed for this reason and are generally based on population mean and variance of the processed data [133;148;166;168].

Noise properties of the reconstruction algorithms are commonly studied either of the fully converged solution or of the images at a particular iteration number [106;133;166]. Though, analytically it is better to study the fully converged solution, reconstructions are stopped after a finite number of iterations, practically. Expressions for theoretical propagation of noise, through iterations, have been developed by Wilson and Barrett for quadratic regularization functions [106;131]. In this work, we developed same type of expressions for the propagation of noise, through any given number of iterations, with MRPs in MAP algorithms. We have also validated our theoretical expressions with Monte-Carlo results.

3.5   Partial Volume Correction (PVC)

Tomographic imaging systems have limited ability to quantify object activity distribution, due to their finite resolution properties. Their resolution is limited by system components such as collimators in SPECT, or crystal size in PET and various physical processes. This limited resolution, consequently, produces Partial Volume Effect (PVE) due to point spread effect or spill-over effect [40;41;141;169]. It is known for a long time that partial volume error induces underestimation, in activity recovery values, for hot objects embedded inside or surrounded by cold background. This effect is known as 'spill-over', from the hot regions having higher activity values into the cold regions with lower activity values. Imaging system's point spread effect (PSF) signifies blurring induced by low resolution of the system for objects of sizes comparable to the reconstructed resolution [33;35;40;143;170;171]. PVE hinders true quantification and is of high importance in measuring response of the tumors to therapy in functional imaging systems. For example, in brain atrophy studies for aging and degenerative brain diseases, partial volume error increases with varying degrees of atrophy [37;143;170]. There have been long time efforts to correct reconstructed images for PVE, with a long list of suggested methods, however, there is not a consensus, for a single method, to be used for PVE, valid for every situation [31-34;37;38;41;172;173].

Initial PVC methods were based on recovery coefficients (RC), where one multiplies measured values in particular regions, with some correction factors [36]. Though, these methods result in good tumor uptake values by implicitly assuming that tumor volume is approximately known, they do not yield PVC images and cannot be used for visual analysis. Another problem is that correction factors need to be pre-collected using some known shape and volume, which is generally assumed to be spherical, and cannot represent practical objects [39;40;42]. This approach was extended to assume regions as spheres

having uniform activity with unknown radius and placed inside a uniform background [40]. Measured image is then modeled as a convolution of the sphere with the point spread function. It is a simple method; however, assumptions required for its implementation are highly restrictive in practical environment. Pixel based PVC methods, work on pixel by pixel basis instead of recovering regional values and, therefore, require structural and functional data together to work upon. By assuming various regions as compartments, with known homogeneous, uptake except where it is being measured, a method has been developed for brain images [34]. A difference of the image produced by convolution of these compartment values and the point spread function with the measured whole image is used to recover the unknown activity. In real imaging conditions, it is difficult to know the activity inside surrounding regions around the region of interest. A generalization of this method was proposed, which does not need this assumption, however, segmentation and registration errors may still persist [172]. These methods assume stationary resolution response which is not true in practice, though, solutions have been proposed to recover for this problem. A recently proposed method of this sort is based on high resolution images, for example CT or MRI, co-registered with low resolution functional images, say from PET [172]. This method also uses wavelet transforms for grey level correlation at the common resolution, which is complex to evaluate.

In contrast to these "post-reconstruction" methods for PVC, where images are processed after reconstruction, several PVC methods have also been suggested for "pre-reconstruction" or during reconstruction correction. MAP reconstruction methods are the ideal to include any structural information available before reconstruction [170]. Most of these methods work as region based methods; however, being pre-reconstruction methods they produce PVC images, instead of only recovering regional activity values. These methods have an advantage that noise can be modeled before PVC; however, they are more complicated, because fractional regional modeling can be a very complex task. Most of the above discussed methods are based on static image reconstruction, which uses some kind of statistical noise model and assume homogeneous activity distribution. However, several methods have been proposed to compensate for PVE in dynamic studies [39]. These methods do recover for PVE, in dynamic images, and include additional parameters for kinetic modeling, which bound them to the only time series calculations and make the problem complex, however, with an advantage of real time PVC. De-convolution has been used to recover spatial resolution in restoration studies. PVC images can be obtained by convolving an assumed true activity image with system response and update the final image adding a weighted difference of the two [174]. These methods do not require high resolution anatomical information. However, they use a segmentation method to define ROI

on the uncorrected images, which is an added complexity. De-convolution based methods greatly amplify the noise; hence, their produced images are not suitable for visual analysis and are preferred only to compare the uptake values.

3.5.1 Partial Volume Correction using MRPs

Geometric transfer matrix (GTM) method for PVC is a generalization of the RC methods and uses high resolution images from CT or MRI for regional definitions [38;39;41;42;172]. This method has successfully been used for brain images to correct for spillover in different brain compartments. Image, as a whole, is considered to be a linear superposition of mutually exclusive regions, with homogenous activity distribution inside each region, to evaluate transfer coefficients, which is practically a difficult condition to fulfill in real situations. Transfer matrix is simple to evaluate for few regions, however, with large number of regions it becomes too complex. Also, assumption of homogeneous activity distribution inside a particular region is not natural. This method was initially developed for FBP and assumes a spatially-invariant system response; hence, it does not account for nonlinearity implicit to the statistical reconstruction methods. It has been shown that this nonlinearity, affects the corrected values, when reconstruction based compensation for detector response is applied and a regional perturbation response method has been introduce to correct for this problem [38;39;39].

Another, recently introduced, method is based on statistical-regional-interaction modeling, instead of linear superposition, by Aston et. al., (2002). They based their model on "Tissue Fraction Effect" and "Point Spread Effect", proposed a least squares solution to derive the problem and addressed the issues of regional activity recovery, estimation of variance and test for homogeneity assumption with correlated and un-correlated noise modeling [42].

Though, the above mentioned methods have some disadvantages, they are capable of recovering good regional activity concentration values. Our work presents an implementation of proposed priors in both of these PVC methods and compares the results with standard QPs. GTM requires an estimator having stationary response, whereas, MAP estimators are nonlinear. A suggestive way out is to use impulse responses evaluated in each region, separately, and use them as the PSF. Similarly, statistical PVC methods are computational intensive and require large storage capacity; however, it is possible to peak off PSF in each dimension to reduce size of the problem. We used the same approach to separate impulse response along each axis to evaluate activity values. MRPs performed equivalent or better than QPs, in various situations. Our results showed that both of these

methods correct the measured activity, corrupted by PVE well, whereas, statistical methods are more sensitive to segmentation error than the GTM method. Also, MRPs have more stable response due to their lesser dependence on the parameter values.

3.6   List-Mode Reconstruction

There is a huge interest in list-mode reconstruction methods after the development of MLEM algorithm by Barret et. al. (1998), for list-mode acquisition data [159;175-178]. However, they mainly discussed savings in storage space and efficient and fast reconstruction options for low count studies. Variations of these methods have been presented, later on, for example, based on concepts of minimization of penalized cross-entropy functions. A faster and more accurate method was developed for iterative reconstruction of list-mode data for low statistics in PET [155;179]. A list mode ML reconstruction method has been proposed, with irregular sampling and depth of interaction, for a rectangular PET system for breast imaging [51;180]. Another List-Mode Iterative Reconstruction Algorithm (ALMIRA) has been presented for SPECT system with a new projector/backpojector pair using radiance distribution to obtain probabilities used in iterative reconstruction [177]. An un-convergent subset version of list-mode reconstruction methods have been developed later with convergent versions of the regularized and subsidized version for speeding up the reconstruction [159]. A list of advantages using list mode reconstruction, over bin mode reconstruction methods, has been published [181]. Data can be collected with higher accuracy and precision in list-mode data acquisition, which is very useful for low count studies. Motion correction can also be easily incorporated into the reconstruction method [182]. Time of flight information can also be included in list mode data for higher accuracy [154;182;183].

All the methods mentioned above are specific to a system or do not consider any resolution characteristics of these methods. A very recent study to evaluate resolution recovery in list mode reconstruction methods, as compared to the other methods including bin mode reconstruction techniques has been done by Bouwens (2000) [179;183]. They developed an iterative reconstruction technique, which used list-mode data with collimator modeling, in SPECT system. They used Gaussian shaped sources of different resolution, placed at different locations inside the FOV to assess spatial response variations. They compared different algorithms and found that variations in response and reconstructed resolution of the list-mode reconstruction methods were worst for off centre locations in the FOV, as compared to the other algorithms. They used a system model partitioned into object dependent and detector dependent modules for better and easy modeling. However,

their method was meant specifically for SPECT system to model different collimators and compares only absolute error at specific iteration number. We evaluated resolution characteristics of different priors included in MAP type list mode reconstruction methods [184]. We used Local Impulse Response (LIR) investigations, to evaluate resolution properties of these priors. No such effort has been done so far, as in our knowledge. We have also compared resolution characteristics of our proposed priors with standard quadratic priors for list-mode data. These results will help in understanding behavior of list-mode reconstruction methods in terms of their resolution and noise properties while object properties are used with data modeling as well.

CHAPTER 4

Non-uniform Resolution Recovery

Tomographic imaging systems require modeling of a number of image degrading effects to compensate for space variant nature of their response [20;141]. Unfortunately, inclusion of these effects into the system model overburdens computational and storage resources and assumptions are made to obtain reconstructions in real clinical times [23]. Complete and accurate modeling can be done with recent computer advancements and image reconstruction methods play a vital role in this modeling. Analytical reconstruction methods assume that projection data follow an ideal line integral model, whereas above mentioned effects are nonlinear and force the data to deviate from line integral model [78;84]. Iterative reconstruction methods have an ability to accurately model these effects and stochastic nature of the data; however, iterative reconstruction problem becomes heavily ill-conditioned due to incomplete data and noise which leads to overly noisy images [67;84;104;141]. To reduce this noise and ill-conditioning of the problem, emission physics is modeled in form of an object prior distribution function [105]. Smoothness and edge preserving priors have been proposed in PLEM reconstruction methods or MAP estimators and quadratic smoothness priors have been investigated vastly due to their convexity. However, they are believed to over smooth images in certain areas and provide images with non-uniform resolution characteristics [147;148;186]. MRPs and TV priors have been used as edge preserving priors with robust edge preservation with no additional parameter required for edge preservation [26;112;128].

In this chapter, we analyze and compare results of an implementation of LIR and of a simple brute force method, including MRPs and TV priors, to evaluate their impulse responses for a comparison of their resolution properties with QPs. We show that QPs produce images with non-uniform resolution properties and propose new MRPs based prior functions to compensate for this non-uniform resolution. We extended certainty based correction method for the correction of non-uniform resolution and further propose methods based on a different prior without a use of certainty correction term. In brief, our objective is to show that, if reconstructed images with uniform resolution properties are

desirable then, MRPs based priors can perform better than other priors in terms of resolution linearity, uniformity, symmetry, noise, reconstruction speed and calculation simplicity etc., and require less number of empirical parameters to be tuned. A theoretical expression has also been derived for iteration based noise propagation in MAP reconstruction methods, including MRPs as prior function, and results have been validated with Monte-Carlo technique [29;129;138].

4.1   Data Simulation and Reconstruction

In this chapter, our main analysis consists of a comparison of various image estimators in terms of their resolution properties and development of new approaches to combat non-uniform resolution. Almost always, new methods in image reconstruction are assessed on the basis of simulated data and then tried on the real scanner data. One of the advantages of using simulated data is to be able to compare reconstructed images directly with true noiseless activity distribution, whereas, it is not possible to separate noise from the signal for real data [107;188;189]. We used a simple system model to simulate our phantom data for the comparison of algorithms and prior functions. It is an imperative argument, in our view, that addition of noise in the data or inclusion of various image degrading effects will further corrupt the results and complicate, slow down or overburden system resources and the evaluation process. Hence, for comparison purposes our simple system model is a valid choice.

4.1.1   Phantom Object Used

Resolution properties of MAP reconstruction algorithms mainly depend on the *activity distribution, object attenuation distribution and various system and estimator characteristics*. We selected a commonly used digital phantom image to simulate our data [24;26;110;129;187]. This phantom represents a superposition of very simple objects, which were further convolved with a 5 x5 averaging filter kernel to delineate sharp edges, and is not an anthropomorphic phantom [107]. There were several reasons to select this phantom. First of all, various regions inside the phantom were used to study the effect of activity concentration and object size variation on the final reconstructed resolution for different estimators. Two circular regions, holding varying activity concentration and embedded inside a background disc, were simulated to study effect of activity variation on the final induced resolution by various reconstruction algorithms. One of the small discs contains higher activity concentration, whereas, the other one contains lower activity

concentration as compared to the moderately hot background disc, which helped us in understanding their comparative behavior. This phantom also facilitated in studying spatial variations in induced resolution and effects of non-uniform attenuation distribution by the addition of an attenuation map of the object. Resolution and noise variations were studied for different reconstruction algorithms and MAP estimators across the FOV and effectiveness of non-uniform resolution compensation methods for QPs, MRPs, and TV priors was measured with the help of this phantom [24]. Our digital phantom image is shown in Figure 4.1, which has been divided physically in 128 x 128 pixels. Relative activity concentration is 1.0 in the left small disc (COLD DISC), 2.0 in the large disc (BKGND DISC) and 3.0 in the right small disc (HOT DISC). Small discs are of radii of 15 pixels and the main background elliptical disc has radii of 30 and 50 pixels with attenuation coefficients of 0.003, 0.013 and 0.0096 mm^{-1}, respectively [129].

Figure 4.3 shows a thorax chest phantom which has been used by several researchers for the evaluation of various algorithms performance [96]. We selected this phantom to analyze and compare the performance of various algorithms and MAP estimators in terms of MAE, percent bias and MSE. Though, this phantom has fairly irregular shaped objects to imitate real object, we used this phantom for our analytical comparison for locally small regions and quantitative comparison for the whole image. Small point sources were added to this phantom, in order to study the effect of various algorithms' response to small sized objects, while only analytically.
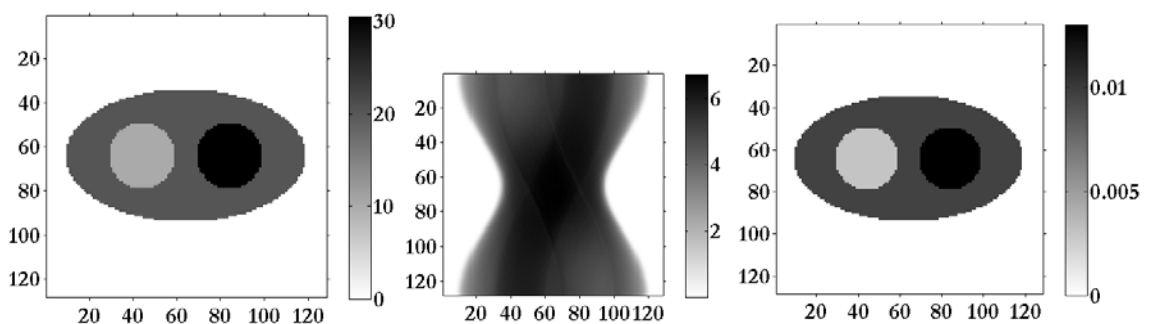
Figure 4.1: Simulated phantom image (left) with its sinogram (center) and attenuation map image (right). Image and sinogram resulted from 1M counts in total while attenuation map image shows the distribution of attenuation with coefficients given in the text above.

Another phantom image, shown in Figure 4.17 and known as holes phantom, was used to study the behavior of QPs, MRPs and TV priors in terms of their noise performance using two hyper-parameter values. This phantom was selected for to its varying sized objects to study the effect of noise and resolution on the estimation of varying sized objects, because it is comprised of small and large sized circular discs.

4.1.2   Data Model

We modeled a simple PET system with 16,384 detector bins or LORs (divided into 128 LORs per angular view for 128 views) over 180^0 around the object. One million (1M) counts were collected in total, assuming a small single crystal detector width equal to that of a single pixel for the sake of simplicity, which was taken to be 1.0 mm in width for the purpose of attenuation correction. A system model was considered without any scatter and background noise included, in which case matrices representing scatter and background noise will become identity matrix $\{H_{scat} = I\}$ in equation (2.4) [23]. However, non-uniform attenuation correction has been included as an attenuation map image and was used to simulate non-uniform attenuation correction factors (ACF) into the system model, as shown in Figure 4.1 (right). These ACFs were obtained by forward projecting an attenuation distribution map with almost resembling values of attenuation coefficients to the real values of soft tissues and bone [8].

4.1.3   Data Simulation Scheme

For event simulation scheme, a random point (using Matlab's random point generator function "rand()") inside the phantom's emission area was generated to represent a random emission location, along with a random angle from $0 \ to \ \pi$ to simulate gamma ray travelling direction. An LOR index was calculated based on the emission's spatial location and the random angle generated. This value was then weighted by the pixels activity concentration and the probability of detection of the event along a particle LOR using Siddon's (1998), algorithm [53]. Corresponding LOR counts were incremented accordingly to represent its contribution to the final sinogram with an application of the attenuation effect. Figure 4.1 (center) displays a resulting sinogram image.

4.2   Software Implementation

Various simulation software are available freely online which can generate simulated data for different systems, such as SimSET for PET/SPECT and SIMIND for SPECT system. These implementation codes are very straight forward and user friendly. However, for a basic understanding of these imaging systems they are just black boxes. Even though their implementation and modeling details are available in form of various manuals and publications, they are not very fragile and modifiable. Hence, for a better understanding of the working and physics of these systems, we decided to implement our own codes and

routines. However, we only developed our stand alone routine to carry out various task instead of a complete package, because of the availability of the above mentioned software. There were also many unique tasks needed to be carried out in this research work, for which there were no implementations available, for example impulse response evaluation for list-mode data or implementation of PVC method for statistical methods. Another obvious reason for self implementation of various routines was a better and stronger control over different steps of the process. For example, for customized phantom and data simulation or for customized implementation of reconstruction codes and for the evaluation of the geometrical system matrix, it was necessary to code our own algorithms.

Different computational routines were coded and implemented for data simulation and reconstruction purposes, for this work. Calculation of system matrix elements, for a defined PET system model to evaluate probabilities of event emission and detection processes, was a basic requirement for our analysis. Siddon (1985), described an algorithm to calculate system matrix elements for 3D CT reconstruction and is considered to be very fast as compared to the method of evaluation of these probabilities for each pixel in sequence, because it considers only those pixels which are intersected by a specific LOR [53]. Its implementation has further been simplified by Jacob (1998) to simplify most time consuming nested loops of the evaluating code, because this evaluation needs to be performed for each LOR and for every pixel intersected by the LOR [59]. We implemented this algorithm as a MATLAB MEX file which can be directly used as a MATLAB sub-function with its C++ implementation files. This routine is available on File-Exchange webpage, of Mathworks website, under a heading of "PET System matrix" where it can be downloaded freely. This code is a direct computer implementation of Jacob's modified algorithm to evaluate PET system matrix elements for a given LOR for square pixel grid and for parallel beam geometry [59]. It should be noted that this function has been downloaded and used by several people in their development work. It outputs its results in sparse matrix form, which is very helpful in reducing storage requirements and implementation time. Format of this routine is given as follows;

$$Function \ (struct) \ out = sys\_ele\_v2\_new((int) \ lor, (struc) \ sys).$$

In this function, '*out*' is a structure containing intersected lengths and indices of pixels intersected by a particular LOR, whose number is given as an integer variable '*lor*' with a structure defining system parameters in '*sys*'. These input and out variables are clearly defined inside the function definition as comments.

Another very important computer implementation is of various reconstruction algorithms including MLEM, PLEM-QP, PLEM-MP and PLEM-TV as given in Appendix A.2. This is an implementation of OSL algorithm by Green, and has been implemented in LOR major format, instead of pixel based sequential format in a MATLAB function [105]. It should be noted that it evaluates system matrix elements on the fly, hence, does not need to store these elements, which reduces storage requirements. Further, these codes were written for an implementation of our developed prior distribution functions. This routine was implemented in form of a MATLAB function as below;

$$FUNCTION \; [rec\_img, rms] = ImageReconstruction(sys, sino, algo, iter, beta, neigh)$$

Many of the above mentioned parameters are self explanatory, such as '*sys*' is a structure defining system parameters and '*neigh*' is a vector giving neighborhood size and '*algo*' is the algorithm being used, such as MLEM or PLEM-QP.

Implementation of various forms of LIR function was a tricky job because of huge storage and computational burden. With a 128 x 128 image matrix size and same number of LORs, generated file was of Gigabytes size and it was not possible to hold it in double precision in a 2 GB or even 4 GB RAM, available on my laptop. To overcome this problem, two different files were created and stored, for their further use by loading them in turn, having almost half of the matrix size in each file, required by the CG function to evaluate LIR with different MAP functions [100]. This was mathematically equivalent to load half of the matrix at one time for matrix multiplication or addition. Required calculation time of days was reduced to hours using direct matrix multiplication or addition of the most time and storage consuming part of the function i.e. evaluation of $H^t DH$, with this save, load and use technique [24;29]. Similarly, LIR implementation was divided into two parts and initially $H^t DH$ was evaluated and saved and then the whole LIR was calculated by loading this matrix in CG. It was interesting to note that computational time for nonlinear and non-quadratic priors, such as MRPs or TV, was longer as compared to the quadratic priors. It was possible to reduce image size for the same reason; however, the results were not up to the mark for smaller sized images.

Other routines, such as GTM or STAT methods for PVE, were time consuming but with lower storage requirements [41;42]. Similarly, to calculate mean and variance images for iteration based noise analysis, image size was reduced because of its less importance on the final results. For the sake of repetition or improvements, few important routines have been included in this thesis as an appendix.

4.3   Hyper-parameter Tuning and Perturbation Analysis

One obvious disadvantage of MAP estimators is an absence of some specific criteria to choose regularization parameter value. There are few methods proposed in the literature to help in selecting this value. L-Curve is a log-plot of the norm of a regularization solution versus norm of the corresponding residual norm and shows the size of the solution and fit to the data and helps in defining an optimum value of the regularization parameter. However, it is computational expensive and requires a lot of data [68;69]. Unbiased predictive risk estimation (UPRE) is another method which minimizes expected value of the predictive risk and shown to find good estimates of the parameter values, however, with large size problem it becomes complex to implement and computationally expensive. Generalized cross validation (GCV) is another method which minimizes predictive risk, however, it may become flat or may have multiple minima and computational expensive too. These methods either require large data because they are based on statistical analysis or they are computationally extensive [69]. In our experimental work, we only needed to decide crudely for a parameter value where resolution, at some fix point inside the phantom, say at the center is uniform with low computational efforts. Hence, we opted for a technique suggested by Fessler and Rogers (1996), to select β parameter value for a single selected pixel, say inside the center of the object [24;190]. This method consists of a tabulation of reconstructed resolution values for a given pixel and for a range of β values. Then, for any user specific reconstructed resolution, one can simply interpolate that table to get a desired value of the parameter. Though empirical, this method is simple to follow and reduces the burden of extra calculations.

We used our simulated digital phantom image shown in Figure 4.1 for β verses resolution analysis. A point source, having a spread of 4.0 pixels FWHM, was added to the image at the center and its noiseless sinogram data was generated, using same system and parameter values as mentioned in section 4.1. That sinogram was then reconstructed with MAP algorithm, including QPs and MRPs as prior functions, for a number of β values. Figure 4.2 (left) presents reconstructed resolution values at the centre of the phantom image for a range of parameter values for QPs. It also shows β verses resolution response of MRPs with different neighborhood window sizes. Response to the added impulse was evaluated using Brute Force method, which may be defined by the following expression [24],

$$l^j = \lim_{dx_j \to 0} \frac{[\check{f}(x_j + dx_j) - \check{f}(x)]}{dx_j} \tag{4.1}$$

In this expression, $\check{f}(x_j + dx_j)$ is the noiseless reconstruction of the perturbed image at pixel location x_j, $\check{f}(x)$ is a reconstruction of un-perturbed noiseless image and dx_j is the perturbation size added to the $j - th$ pixel. It has been argued by researchers that mean reconstruction from a sample of noisy data, using MAP estimators, highly resembles to the reconstruction from noiseless data [159]. Hence, we used only a single reconstruction from noiseless data for our analysis. Figure 4.2, displays profiles for FWHM against different perturbation sizes and parameter values, for QPs and MRPs with a neighborhood size of 3 x 3, to obtain optimum parameter value and perturbation size for these priors. Figure 4.2 (top and bottom right), shows reconstructed resolution response for the centre pixel of the image against perturbation size. Resolution seems to approach its limit for QPs as β value increases and size of the perturbation dx_j decreases.
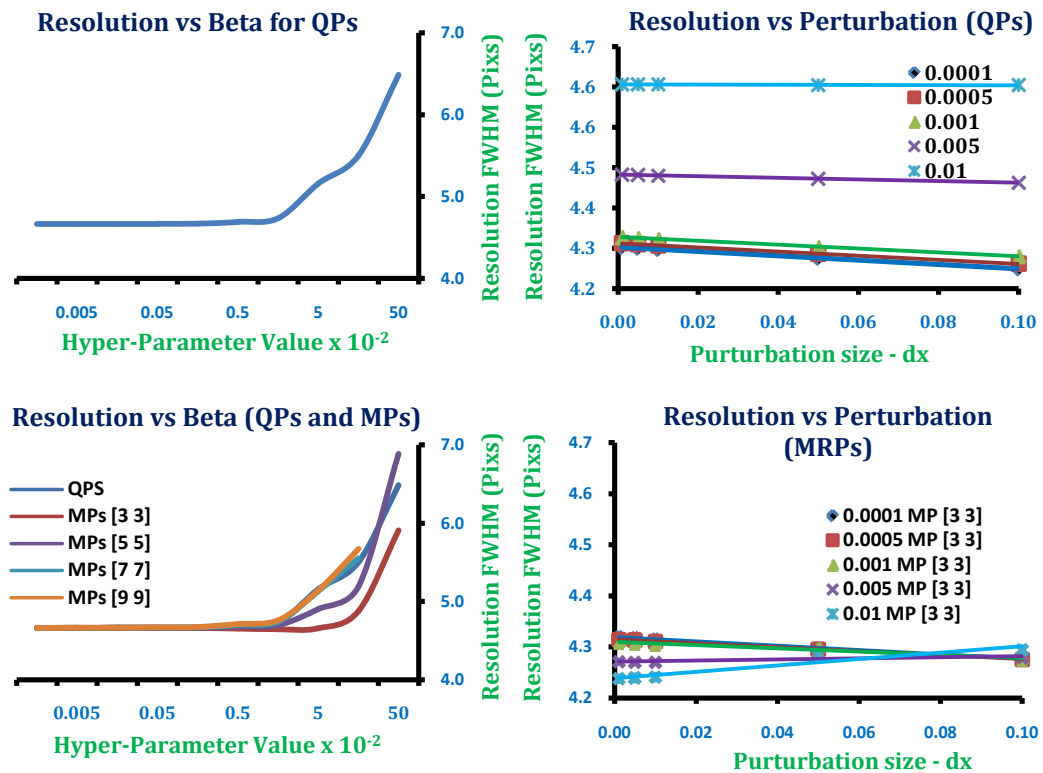
Figure 4.2: (left) Resolution FWHM (in pixels) plotted for a range of hyper-parameter values for QPs. Profile is almost flat for small values of the parameter whereas reconstructed resolution worsens very fast for values above 0.01. Sinogram was blurred with a Gaussian filter (FWHM=4.0 pixels) to introduce a detector blur and to define our targeted resolution. (right) Reconstructed resolution against perturbation size and parameter values and indicates that by reducing perturbation size and decreasing parameter values, reconstructed resolution approaches a limit. Sinogram was blurred with a Gaussian filter (FWHM=4.0 pixels) to introduce a detector blur and to define our targeted resolution.

Similarly, for MRPs, resolution approaches its limit with decreasing β value and the perturbation size. We selected a perturbation size of 1.0 x 10⁻⁴ for a reasonable impulse

response width. Figure 4.2 (top and bottom left), shows reconstructed resolution in FHWM (Pixels) against β values for QPs and MRPs. For very small values of β, induced resolution remains stable at approximately 4.3 pixels while it increases rapidly for a beta value > 5.0 x 10^{-3} with an average pixel value of 4.5 pixels. This means that prior starts getting more weight after this value and its effect get stronger on the resultant image beyond this point, whereas data has the dominant effect before this value. Neighborhood size used for QPs was 3 x 3 pixels and increasing this size does not have much effect on the profile, which means far pixels do not affect the results much. We draw resolution profiles, against β values, for MRPs using different neighborhood window sizes. A window size of 3 x 3 pixels, for MRPs, has a response more stable than QPs, against β value, whereas, it is worse than QPs for a 9 x 9 window. This indicates that, in case of MRPs, reconstructed resolution is more sensitive to the selected neighborhood window size as compared to the influence of β parameter, which is stated other way by other researchers [107]. We may infer from these results, that it is better to study resolution properties of such estimators with fully converged solution instead of iteration based analysis [166]. Based on the above results, we selected values of hyper-parameters, i.e. 1.0 x 10^{-2}, 5.0 x 10^{-4} and 1.0 x 10^{-4} to analyze for image quality.

4.4   Reconstruction Algorithms

Unfortunately, real systems do not provide noiseless measurements and appropriate sampling or sub-sampling is further required. In PET system, arc-correction is needed to sample the data back into parallel projections for FBP reconstruction. In 3DRP reconstruction algorithm, complete 3D data is not available and one needs to fill in the missing data by forward projecting an initial reconstruction [191;192]. In Fourier Rebinning (FR) reconstruction method, 3D data is rebinned into 2D projections, before 2D FBP is applied, which suffers from geometric distortions due to rebinning process. For accurate reconstruction, all the physical image degrading effects need to be included in the system, whereas, non-uniform attenuation in SPECT system is very difficult to model [8;10]. Approximate, ACFs may be applied, which do not compensate well for the error. Similar to the FBP, depth dependent attenuation is a problem for direct inversion methods and these methods do not incorporate any underlying data noise model in the reconstruction.

Non-statistical iterative methods try to estimate the image by discretizing the problem into a set of unknowns. They mainly use the ideal line integral model in discrete form and do not consider underlying noise models in the reconstruction problem. Statistical iterative

methods, such as MLEM methods, try to achieve this by explicitly defining some model of the measurements in the form of data likelihood [91;122]. Several models can fit into the reconstruction framework, while defining the likelihood function. However, because the image reconstruction problem is ill-posed, MLEM tend to produce overly noisy images similar to the noise amplification by ramp filter in FBP. Methods have been proposed to reduce this noise, which generally apply some implicit regularization such as truncated iteration or post-convergence filtering. However, these methods have poor resolution control of the reconstructed images. Smooth basis function based approaches, such as blobs, need large number of iterations to converge and may also increase the ill-conditioning of the problem [49;72;73;104;193].

MAP reconstruction methods based on Bayes' rule, or equivalently PLEM reconstruction approach in the penalty design framework, has two advantages over the other alternate methods for regularization [76;77;121;123]. Firstly, because a prior distribution is formed about the object and then a MAP estimate is sorted, inclusion of the prior distribution improves conditioning of the problem and, secondly, various prior distributions can help control the final reconstructed image characteristics, especially the resolution, in our perspective. Nonnegative definite prior functions are generally selected, for maximization purposes of the overall objective function. Prior functions are very important in determining the final image quality [93;110;121;125;126;165]. Simplest form of the prior function used is called the smoothing or the quadratic priors. These priors work on the basis of pixel differences and generate overly-smoothed or an-isotropically blurred images. This fades out the salient features such as edges inside the image. Alternatively, edge-preserving prior functions are used for reconstruction [129;165].

Non-quadratic edge preserving prior functions have been introduced, however, they make the objective function non-convex and produce patchy areas of varying intensities. Median Root Priors (MRPs) and Total Variation (TV) prior functions have a robust property to preserve the edges. A numerical problem with these two prior functions is that their analytical derivatives are not defined, however, various heuristic definitions of the derivatives have been proposed which work well [112;114;116;128]. They only have a problem that their convergence properties cannot be analytical described. In this work, we opted for prior functions based on MRPs and TV regularization functions and analyzed their resolution characteristics, in detail. We developed methods for the compensation of non-uniformity in reconstructed resolution using MRPs prior functions [30]. This topic is the main focus of our work and will be discussed in detail in the next sections.
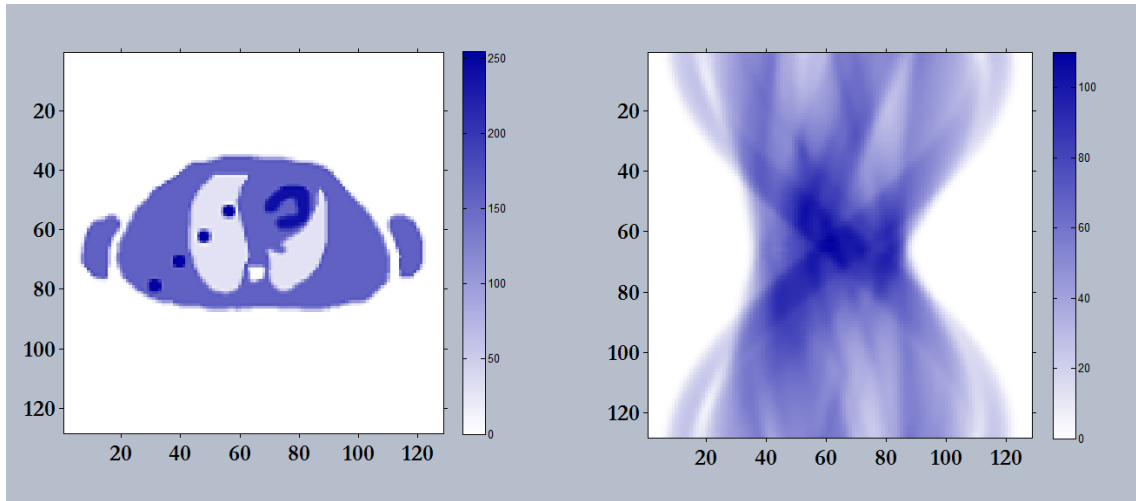
Figure 4.3: Digital thorax phantom with its simulated sinogram data.

In this section we compare performance of various algorithms and prior functions using a simulated digital human thorax phantom of size 128 x 128 pixels. This phantom has been simulated in the same manner as described above, though without simulating non-uniform attenuation.

Table 4.1: Reconstruction methods used and their corresponding abbreviations mentioning different parameter values and neighborhood sizes.

Reconstruction Methods	Abbreviations
Filtered Backprojection, Hann filter, 0.5 cut-off	FBPh
Maximum Likelihood, 15 iterations	ML15
Maximum Likelihood, 30 iterations	ML30
Maximum Likelihood, 200 iterations	ML200
MAP reconstruction with QPs, 15 iterations	QP15
MAP reconstruction with QPs, 200 iterations	QP200
MAP reconstruction with MRPs, 15 iters. [3 3] window	3MRP15
MAP reconstruction with MRPs, 15 iters. [7 7] window	7MRP15
MAP reconstruction with MRPs, 200 iters. [3 3] window	MRP200
MAP reconstruction with TV, 15 iterations	TV15
MAP reconstruction with TV, 200 iterations	TV200

The reconstruction algorithm can be considered as an estimator of the unknown quantities or pixel values and performance of different algorithms can be compared using several measures. The estimate should be unbiased, statistically, and often there is a trade-off between bias and variance of the estimate. The variance measures the variability of the calculated estimate.
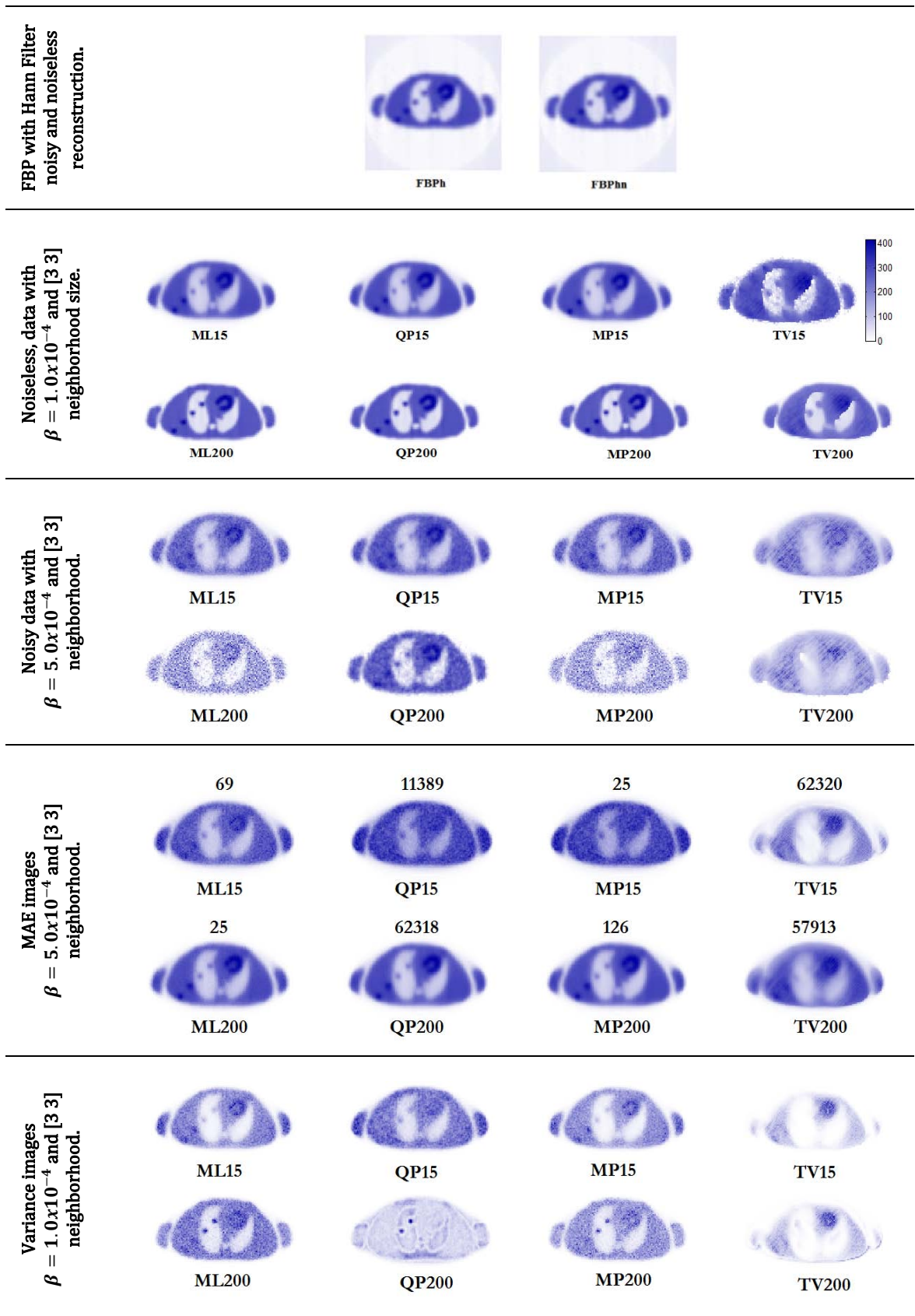
Figure 4.4: Reconstructed images of a thorax chest phantom for noiseless and noisy data with different algorithms and parameters values. Images in the top most row is for noiseless data and a β value of 1.0 x 10-4 for QPs, MRPs and TV with a neighborhood size of [3 3]. Second and third row images were reconstructed using same parameters but for β values of 1.0x10-4 and 5.0x10-4, respectively. Last row contains images for MRPs only with β value of 1.0x10-4 and neighborhood size of [7 7].

An estimator with small bias from the average, whereas having large variance, may make an individual estimate unreliable. Mean square error (MSE), generally, depends on both bias and variance and mean absolute error (MAE) can be a measure of accurateness and changeability of the estimate. Some of these measures need to know the true activity distribution, so simulated data is most helpful in this comparison [166]. The quality and estimation of the effect of noise on the correctness` of reconstructed images was evaluated using our simulated phantom shown in Figure 4.3. Our phantom is not an anthropomorphic one but served well for quantitative testing, because the reconstruction algorithm should be able to reconstruct any kind of data. This phantom image was forward projected to a noiseless sinogram and then Poisson noise was added to it, using Matlab "imnoise()" function, in order to get 100 different noisy realizations.

These sinograms were reconstructed using different algorithms, as listed in Table 4.1, and priors with different parameters values. The aim was to compare MRPs performance with well experimented standards, FBP and MLEM algorithms, and then further compare with QPs and TV in MAP algorithms. In order to examine the consequences of the selection of suitable prior function, images were tested against known true phantom image and the statistical properties of the images were inspected. We treated the whole image as an ROI bearing non-uniform activity distribution and used following relations to compare various algorithms and priors [128].

$$
\begin{aligned}
MAE &= \frac{\sum_i |I_i - \mu_i|}{N} \\
Var &= Var(I_i) \\
\%bias &= \frac{\sum_{i \in roi} \left(\bar{\bar{f}}_i - f_i \right)}{N_{roi} \times \bar{t}} \times 100 \\
MSE &= bias^2 + \sigma^2, for\ i = 1,2,\dots,100
\end{aligned}
\tag{4.2}
$$

In this relation, bias is defined in terms of mean reconstructed image pixels $\bar{\bar{f}}_i$ and true ROI mean $\bar{t}$ with N_{roi} number of pixels in the ROI. To evaluate mean image pixels, we reconstructed images from 100 noisy realizations, by inducing Poisson noise in the true phantom image. σ^2, is variance of all the pixels from all the noisy reconstructions, for a particular algorithm, and for a specific value of the hyper-parameter, if required. We decided for a set of reconstruction methods, as given in Table 4.1, to compare their reconstruction abilities, as an initial assessment of their reconstructed resolution properties, in the form of regional uniformity and shape distortions. Here, we present results for two different hyper-parameter values are shown for different prior functions in MAP reconstruction algorithms.

Figure 4.4 displays thorax phantom images reconstructed using different algorithms for few parameter values. Mean Absolute Error (MAE) and Variance images have been calculated from 100 noisy reconstructions, of the phantom image containing Poisson noise and total 1M counts with an average of ~400 counts per non-zero pixel. *MAE* and *variance* images have been calculated using 100 noisy reconstructed images. Noiseless reconstructions are not much different from each other except for FBP images which contain streak artifacts and TV images show patchy edges in both images obtained after 15 and 200 iterations.

Streak artifacts are visible in FBP images for noiseless or noisy data with false activity impression outside the object boundaries. Some mock activity, for example around the arms, can be seen in noisy and noiseless data in images obtained after 15 iterations for all the iterative algorithms. This is possibly the initial uniform activity guess used to start the iterative algorithm and indicates initial convergence of low frequency components. All the algorithms performed almost similar for noiseless data even after 200 iterations, however, with noisy data MRPs and ML algorithms behave much the same way. Their reconstructed images are closest to each other as compared to the images reconstructed by other algorithms and indicate least smoothness [128]. For TV priors there are obvious patchy artifacts. Global image variance is displayed along with MAE images, which is smallest for ML and MRPs, whereas, TV priors present worst results. QPs produce images with maximum smoothing effect which is, certainly, strong blurring effect instead of the effect of noise reduction.
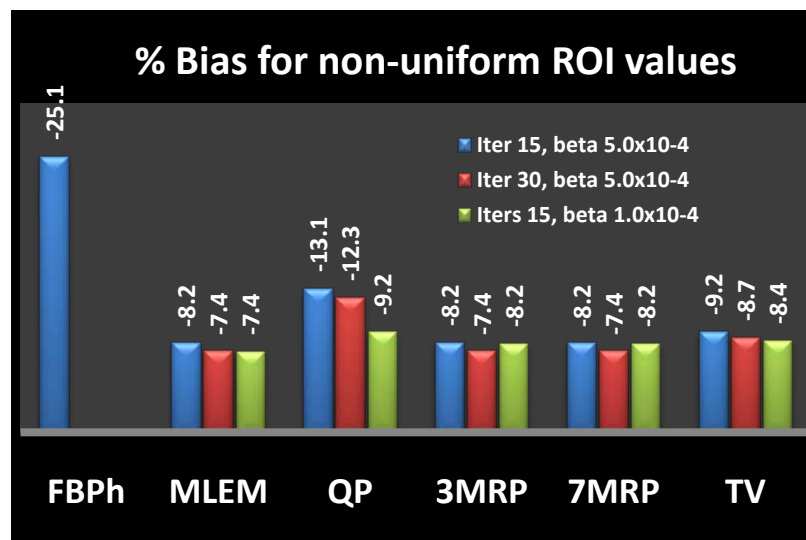
Figure 4.5: %Bias values for various algorithms and parameters such as iterations and hyper-parameter values.

Last row displays variance images calculated from same 100 noisy reconstructions, and the results indicate that MRPs and ML estimates are almost matching, whereas, QPs and TV show some strenuous artifacts, which indicates their poor noise performance in terms of variance. These results demonstrate superiority of MRPs, over the other algorithms, for iteration based reconstruction image quality and noise performance. We present results for Bias, Figure 4.5, and MSE, Figure 4.6, values for two different iteration numbers (15 and 30) and two parameter values (5.0×10^{-4} and 1.0×10^{-4}). Selected ROI includes those pixels having non-zero value inside the phantom image and contains non-uniformly distributed activity concentration. All MAP algorithms seem to perform better than FBP in terms of percent bias values. Both MRPs perform almost same as MLEM, whereas, TV priors performed worse than MRPs, but, better than QPs. QPs have poor performance in case of percent bias, which is a measure of accuracy, due to heavier smoothing induced by them and this behavior worsens with higher β value. High frequency components converge at higher iteration number and that seems to be a reason for slightly better results. Mask window size and iteration number do not have appreciably different effect for MRPs results due to earlier convergence of the low and high frequency components at earlier iterations. TV priors behaved almost similar manner to QPs, with lower bias values, which suggest their almost similar smoothing trend and dependence over η parameter value.

Figure 4.6 presents results for MSE for various algorithms in terms of iteration number and β parameter value. FBP is not included here and MLEM performs worse with increasing iteration numbers. QPs work better than MRPs and TV priors, with lower error at higher β values, which indicates heavier smoothing, and slightly increased error with increased iteration number. MRPs and TV perform almost similar due to the median and differential operations. Percentage bias values provide us with accurateness of the behavior of a particular measurement or estimation process and MSE is a measure of preciseness. In our analysis, we defined MSE including both bias and variance, however, bias is very small as compared to the variance, hence, it is mainly a measure of preciseness. According to these results MRPs performed well in terms of accuracy and almost equivalently to other algorithm in terms of precision.

Resolution properties are commonly studied either iteration based or of the fully converged solution and depend upon estimator characteristics [106;166]. In our work in this chapter, we analyzed resolution properties of the fully converged solution, using impulse response function and brute force empirical method, in terms of *resolution uniformity* and *impulse response linearity and symmetry* across the FOV.

MSE for non-uniform ROI values
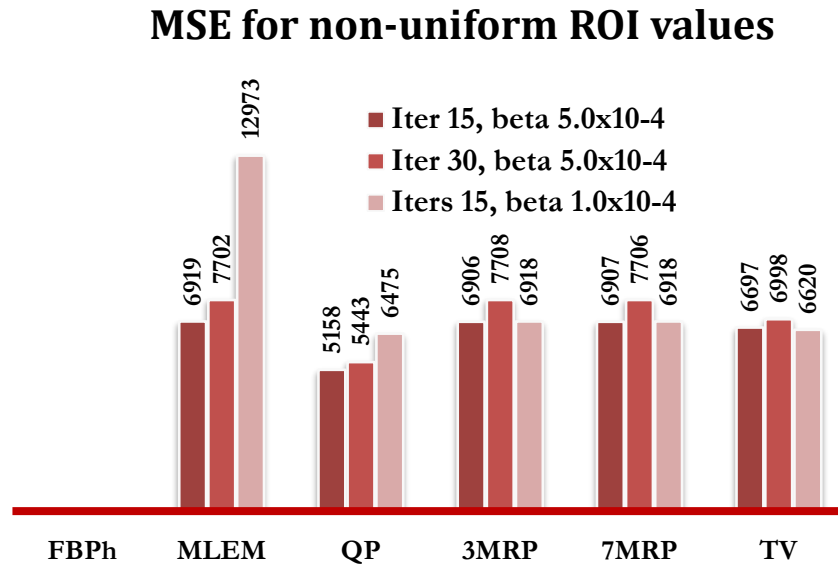
Figure 4.6: MSE values for various algorithms and parameters.

Other influencing factors such as *hyper-parameter sensitivity*, *activity concentration distribution* and *spatial location* inside the FOV have also been discussed. Our strategy mainly proceed with choice of a proper prior distribution function, for the purpose of uniform reconstructed resolution, in order to see if MRPs may provide lesser variations in system response as compared to the other priors, specifically QPs.

4.5   Resolution Properties of QPs

Reconstruction algorithm controls speed of the reconstruction process and does not affect the final solution, as far as objective function maximization is concerned, however, it is possible to control the final image characteristics through the choice of prior function in MAP algorithms. Some algorithms though, such as Ordered Subset Expectation Maximization (OSEM), intrinsically do not converge to a single final solution but only speed up the reconstruction [137]. Post-reconstruction filtering or sinogram de-blurring methods can produce images with almost uniform resolution characteristics for space-invariant systems, whereas, they may need a large number of iterations to finally converge [120]. Analytical methods, such as FBP or direct inversion methods, are better suited for space-invariant systems, but, have an embedded mismatch between practical real system models and model of their own [78;151;185]. Methods based on un-regularized ART techniques may take much longer to converge and need post filtering to specify their resolution properties, which will mostly depend on the chosen filter. Least Squares methods such as Penalized Unconstrained Least Square (PULS) methods are linear reconstruction methods.

These are, generally, based on incorrect noise model and do not relate reconstructed resolution to the hyper-parameter values directly.

In post-filtered MLEM, resolution properties depend on and can fully be expressed by the properties of the filter used and can provide almost uniform resolution properties of the final image for space-invariant systems. However, space-variance and depth dependent attenuation in SPECT may not be fully compensated by these methods. Unconventional pixel basis, such as blobs, can provide good uniform resolution properties, however, may take large number of iterations to converge due to an overlapping of the basis functions. Statistical MAP estimators including standard QPs, provide non-uniform resolution which is space-variant and object and system dependent. Certainty based correction methods have been proposed to compensate for space-variant resolution properties of QPs in PLEM reconstruction framework, however, edge smoothness still remains a problem [26;90;193;194].

With all the methods reviewed above, MAP estimators have stronger control over the resolution properties, convergence speed, edge preservation, noise control and ability to incorporate noise model as compared to the other methods. In the following sections, we have presented resolution characteristics of MAP estimators, including MRPs in comparison to QPs and TV, and suggest correction methods, based on certainty correction method developed earlier for QPs in PLEM methods and, in addition, suggest new correction method based on alternate prior function to compensate for non-uniform reconstructed resolution. Standard QPs are the most favored priors due to their simple implementation and their resolution characteristics have already been investigated in detail [24;26;29;108;118;129;138]. In the next section, resolution properties of QPs in MAP reconstruction methods are briefly analyzed with noiseless phantom data.

4.5.4 Resolution Uniformity and Symmetry

Space-variant system response for QPs is a consequence of different image degrading effects, which act non-uniformly across the FOV. Figure 4.6 (a) presents results for an evaluation of resolution properties of QPs at three specific points inside the phantom including emission and transmission properties. These three points were selected to evaluate effect of varying activity levels and its spatial distribution and are at the centers of two small COLD and HOT discs and at the center of the whole image. Purpose of this evaluation is three folds: first to analyze local resolution properties of the estimator, second to quantify and compare local reconstructed resolution and third to compare different priors and to seek for more suitable prior distribution function based on this analysis. Here,

we present resolution properties of the reconstructed images in terms of their *space-variance, linearity and symmetry for QPs* and evaluated responses using brute force method, as given by equation (4.1) [103;129].

 Though, a large number of noisy reconstructions are required to obtain mean reconstructions from noisy data sets, it is luckily, well known that reconstructions from noiseless data very well approximate the noisy mean reconstruction [24;102;106]. Therefore, only a single reconstruction of a perturbed and unperturbed noiseless data is required to evaluate impulse response. This perturbed version is simply the addition of an impulse to a pixel of interest. An accumulative horizontal profile through the impulses at the selected pixel locations is shown in Figure 4.2(a), obtained by MAP reconstruction methods using QPs with two different β values and 30 iterations to display resolution space-variance and non-linearity. Symmetry contours, with contour heights at 99%, 75%, 50% and 25% of the peak value at center of the impulses, are shown in Figure 4.2(b).
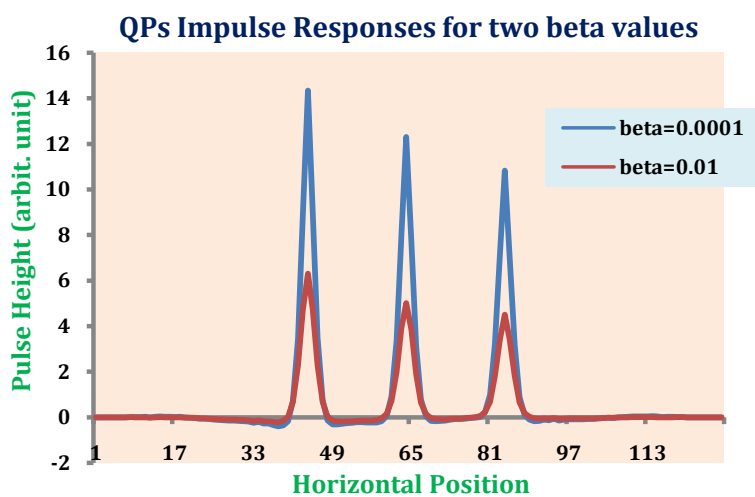
Figure 4.7: (a): Resolution (shown as FWHM in pixs) at the center of the small discs of an image reconstructed by QPs with two different parameter values. Resolution is almost uniform with lower parameter values whereas the responses are heavily smoothed out and have non-uniform response with higher values of the parameter which indicates high dependency of induced resolution on parameter values.
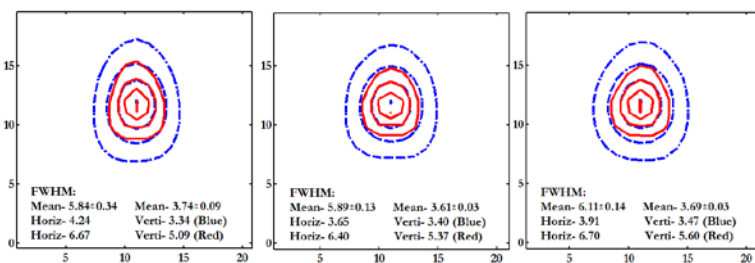
(b): Response symmetry shown as contours at 99%, 75%, 50% and 25% of the peak value at the center of the three disks for two parameter values. Responses are asymmetric and spread out with higher parameter value.

 Responses get heavily smoothed out, with large β value or with higher weight given to the prior term, whereas they get thinner and less smooth with lower β values. Similarly, responses are nonlinear and depict non-uniform resolution at three different locations, as shown by the FWHM values, with poorer resolution in high count regions. Symmetry

contours are elongated in vertical direction due to higher attenuation encountered in that direction. These contours are not very irregular though, because of a simple system model introduced without considering many of the degrading effects, which will certainly distort the response further. These results indicate that reconstructed resolution, with QPs in MAP or PLEM methods, is non-uniform, non-linear and asymmetric due to anisotropic smoothing produced by these priors across the field-of-view (FOV) with higher sensitivity to β values. So, even the spatially uniform penalties or shift-invariant penalties bearing isotropic and symmetric weighting in a local neighborhood of a pixel, such as QPs, which are expected to induce uniform resolution response across the FOV, produce space variant system response in terms of local uniformity, linearity and symmetry, which is further sensitive to the hyper-parameter values [26;129].

4.6   Local Impulse Response Evaluations

Because resolution properties depend on the number of iterations used in brute force method, to work out properties of the fully converged solution we implemented LIR given by equation (2.39), using our defined system matrix and a simulated human torso phantom data, presented in Figure 4.8. An impulse response was evaluated at the location shown in Figure 4.8. Surface plot indicates that the response is asymmetrical which is further elaborated in a contour plot at four different heights (99%, 75%, 50% and 25%) of the peak value. This plot indicates that horizontal and vertical resolution, in FWHM is 1.27 and 1.69 pixels, respectively. LIR allows us to quantify resolution at some given location inside the object, and possibly with respect to some given target resolution. For example, in this image the desired response was selected to be isotropic and with 1.00-pixel FWHM.

To assess space-variant nature of the system response with QPs, we evaluated impulse responses at a number of locations inside our digitally simulated phantom. Instead of evaluating LIR at all pixel positions, we used a sub-sampled grid of pixel points of interest for our investigation, as shown in Figure 4.9. Sub-sampling was used to see an effect of the varying activity and varying spatial position inside the phantom.

This figure shows a grid of sample points along with contour maps of the LIR function at each pixel position. Numbers mentioned at top of each contour plot represent average contour radius in pixels of the impulse at 50% height, and standard deviation of the contour radius at that height.
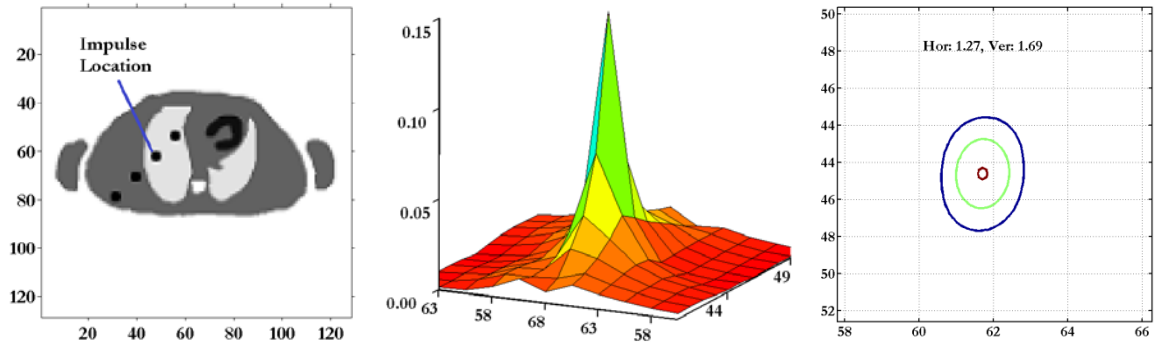
Figure 4.8: 2D Local impulse response inside torso phantom at the specified location (left) with a 2D surface plot showing asymmetric response (center) with a zoomed 2D contour at four heights with respect to the peak (right).

Mean reconstructed resolution is higher in the high activity area as compared to the low activity region. Standard deviation is higher in the low count area which indicates higher error in low activity region. This indicates that QPs produce higher and anisotropic smoothing in high count regions as compared to the low count areas, which makes reconstructed resolution non-uniform and asymmetric.
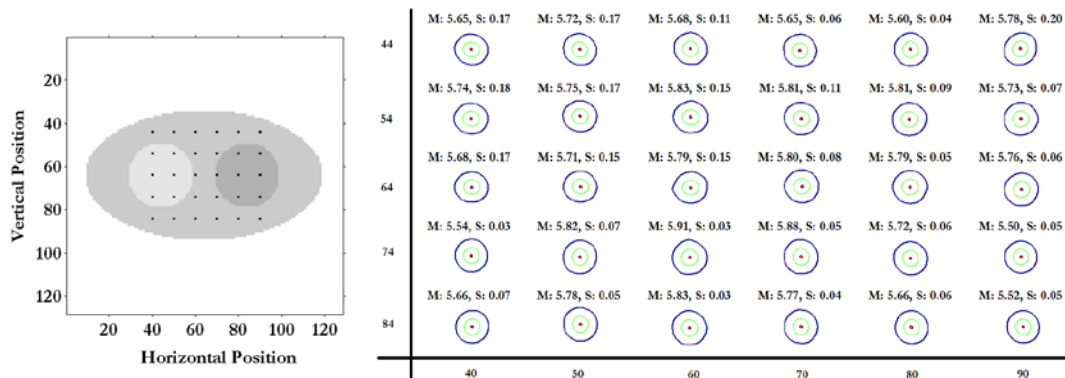
Figure 4.9: Impulse responses evaluated at various locations inside our simulated phantom.

β parameter value was selected to be 0.01 for these results. This sub-sampling is justifiable because impulse response does not change appreciably with spatial position. These results indicate that spatial resolution is space-variant with higher smoothing in the high count region for QPs in MAP estimators.

4.7   Non-uniform Resolution Analysis and Correction Methods

LIR expression, equation (2.39), elaborates that response of an imaging system for MAP methods depends on the properties of the *system, the object* and *the estimator* used including *the prior distribution function*. Hence, even uniform shift-invariant penalties, or

priors in Bayesian perspective, produce shift-variant response instead. Theoretically, we can say that although the prior term was added to reduce final image noise and better condition the problem, it makes the system response non-uniform and asymmetric across the FOV. This may be understood partially, if we assume that measurement noise is homoscedastic or has a uniform variance v, then the variance term in LIR may simply be written as a scaled identity matrix: $D = v^{-1}I$ and LIR will become [129],

$$
\begin{aligned}
l^j &= \left[v^{-1}H^tH + \beta\ddot{R}(f)\right]^{-1}v^{-1}H^tHe^j \\
&= \left[H^tH + v\beta\ddot{R}(f)\right]^{-1}H^tHe^j
\end{aligned}
\tag{4.3}
$$

This relation shows that the effective smoothing parameter $v\beta$ is not constant and depends on the local variance. Hence, regions with higher variance or higher mean activity for Poisson noise will observe heavier smoothing or lower induced resolution.
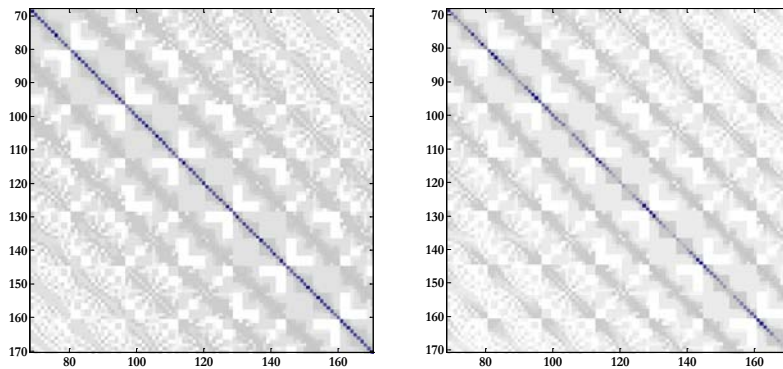
Figure 4.10: Zoomed image of $\boldsymbol{H^t diag\left\{\frac{1}{Y_i}\right\}H}$ and $\boldsymbol{H^tH}$ near the diagonal. The diagonal term makes the diagonal of FIM highly non-uniform as compared to the FIM without it.

Mathematically, Fisher information matrix (FIM), $H^t diag\left\{\frac{1}{Y_i}\right\}H$, or so called *data certainty,* will be smaller in regions with higher activity and the prior will get more weight which will ultimately lower the induced resolution [195]. FIM can be considered as a mapping from and to the image space. Due to non-uniform variance term, $\left\{\frac{1}{Y_i}\right\}$, diagonal of this matrix is highly non-uniform as shown in Figure 4.10 and adds to the non-uniformity of the induced resolution across the FOV.

4.7.1 Certainty-based Correction Method

QPs produce images with space-variant resolution properties due to anisotropic smoothing which is higher in high count regions. This suggests a way to compensate for

this smoothing by introducing some factor into the response function, which depends on local activity concentration, or in other words certainty of the rays crossing a particular pixel [29]. If we use factorization of the system matrix as given in equation (2.4), then system matrix may be split into pixel dependent, ray dependent and geometry dependent factors. In such case, we may write, $H = diag\{c_i\} \, H_{geom} \, diag\{s_j\}$ with c_i as LOR dependent and s_j as pixel dependent factors and H_{geom} is the object independent geometric system matrix defining only geometric probabilities as $H_{geom} = \{g_{ij}, i = 1, \dots, M \ and \ j = 1, \dots N\}$. The matrix $H^t{}_{geom}H_{geom}$ is almost shift-invariant and induced non-uniform resolution is a consequence of non-uniformity in the variance term $diag\left\{\frac{1}{\overline{Y}_i}\right\}$. Because measurement mean is not directly available, we simply replace it by the noisy measurements, or $\overline{Y}_i = \overline{y}_i$. With such a non-unique factorization, the LIR would become,

$$
l^j \approx \left[diag\{s_j\}H_{geom}^t \, diag\left\{\frac{c_i^2}{y_i}\right\} H_{geom} \, diag\{s_j\} \right.
$$
$$
\left. + \, \beta \ddot{R}(f) \right]^{-1} diag\{s_j\}H_{geom}^t \, diag\left\{\frac{c_i^2}{y_i}\right\} H_{geom} \, diag\{s_j\}e^j \qquad (4.4)
$$

The Fisher Information Matrix in the above expression can be written as,

$$
FIM = \, diag\{s_j\}H_{geom}^t \, diag\left\{\frac{c_i^2}{y_i}\right\} H_{geom} \, diag\{s_j\}
$$

Or element wise, with $\left(H_{geom}\right)_{ij} = g_{ij}$,

$$
(FIM)_{ij} = \, s_j^2 \sum_i g_{ij}^2 \frac{c_i^2}{y_i} = k_j^2 \sum_i g_{ij}^2 \ for \ j = 1, \dots, M
$$

With,

$$
k_j^2 = \, s_j^2 \sum_i g_{ij}^2 \frac{c_i^2}{y_i} \Big/ g_{ij}^2. \qquad (4.5)
$$

This equation shows that, k_j, is a normalized back-projection of the term, $\frac{c_i^2}{y_i}$. Fessler and Roger (1996), proposed an approximate *FIM* based on the above estimation so that the matrix becomes almost shift-invariant [24], as follows,

$$FIM = \ diag\{s_j\}H_{geom}^t \ diag\left\{\frac{c_i^2}{y_i}\right\} H_{geom} \ diag\{s_j\} \approx FH_{geom}^t \ H_{geom} \ F$$

where,

$$F = diag\{k_j\}$$

With this *FIM*, the LIR expression will become,

$$l^j \approx \left[FH_{geom}^t \ H_{geom} \ F \ + \ \beta\ddot{R}(f)\right]^{-1}FH_{geom}^t \ H_{geom} \ Fe^j$$

$$= F^{-1}\left[H_{geom}^t \ H_{geom} \ + \ \beta F^{-1}\ddot{R}(f)F^{-1}\right]^{-1}H_{geom}^t \ H_{geom} \ Fe^j$$

$$= k_j F^{-1}\left[H_{geom}^t \ H_{geom} \ + \ \beta F^{-1}\ddot{R}(f)F^{-1}\right]^{-1}H_{geom}^t \ H_{geom} \ e^j$$

For further approximation, they concluded that in local neighborhood of a single pixel effective smoothing depends on certainty of the number of LORs passing through that pixel and, with higher certainty the induced resolution will be poorer. They proposed a modified prior term, based on the above observation as $F^{-1}\ddot{R}(f)F$ and the LIR with an assumption that neighboring pixels have similar certainties, would simplify to,

$$l^j \approx k_j F^{-1}\left[H_{geom}^t \ H_{geom} \ + \ \beta\ddot{R}(f)\right]^{-1}H_{geom}^t \ H_{geom} \ e^j \qquad (4.6)$$

Assuming almost shift invariant H_{geom}, this modified LIR produces uniform responses with standard QPs. Technically, this modified penalty term only corrects for interactions between data non-uniformity and the prior term or $F^{-1}\ddot{R}(f)F^{-1}$.
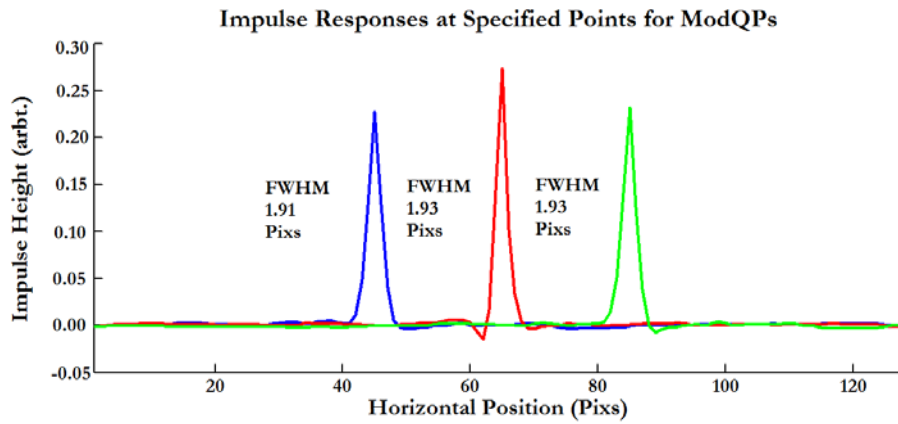
Figure 4.11: Accumulative horizontal profile through impulses at three selected points for ModQPs with a parameter value of 0.01. Resolution is given in FWHM in Pixels at the three points. Responses have almost similar reconstructed resolution and non-linearity due to difference in activity concentration has almost been removed.

Secondly, the presence of $k_j F^{-1}$ term indicates that there will be some asymmetry near the edges, where there are heavier data transitions due to the variance term [29]. Figure 4.11, presents horizontal profile through impulse responses at three locations inside our phantom. Responses are thinner as compared to QPs and have higher reconstructed resolution. Responses are also less non-linear and heavier smoothing due to the prior weighting has almost been recovered. Hence, modified QPs have an ability to recover for non-uniformity and non-linearity in the system response due to non-uniform activity concentration. However, edge preservation is a problem with QPs because there are higher pixel differences at edges and there is no obvious tuning method in the prior to locate edge differences. We present an alternate correction method for non-uniformly induced resolution with MAP estimators based on MRPs.

4.7.2   Alternate Prior-based Correction Method

LIR expression based on modified QPs corrects for interactions between data or likelihood term and the prior term by multiplying a local certainty based correction term with the prior. This correction term corrects for non-linearity induced by the differences in local activity concentrations at various locations inside the object. However, this modified prior function still contains QPs as the basic prior function and will pose a problem of overly smoothed edges. Non-quadratic priors may also be used; however, they will induce object dependent non-linearity to the response and would make the prior function non-convex, hence adding to the ill-conditioning of the problem and, generally, need extra empirical tuning parameters.

QPs suffer from underlying non-linearity in the local variance, whereas ModQPs try to correct for this local variance by including a correction term based on the local certainty. This non-linearity correction may also be induced using some non-linear prior function. This may add to the ill-conditioning of reconstruction problem and will need a compromise between the correction needed and further processing needed to solve the problem. We propose the use of MRPs as an alternate prior to develop a modified LIR [30;107].

MRPs Impulse Responses for two beta vals
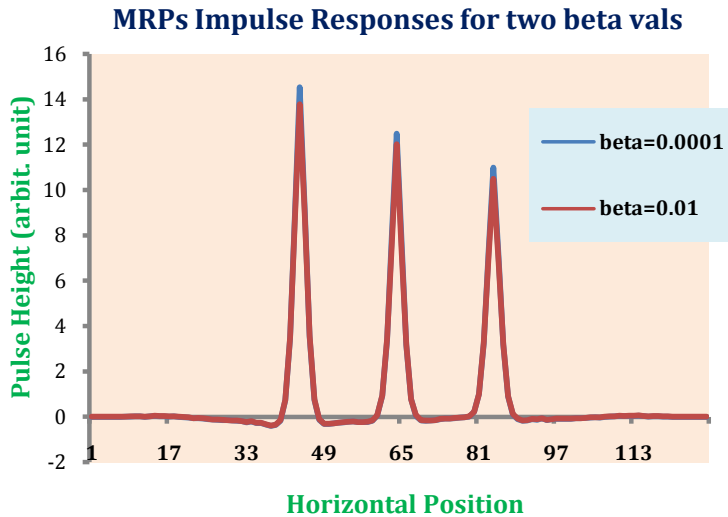
Figure 4.12 (a): Resolution (shown as FWHM in pixs) at the center of the small discs of our phantom image reconstructed by PL-EM-MPs with two different parameter values. Resolution is almost uniform with lower parameter values whereas the responses are heavily smoothed out and have non-uniform response with higher values of the parameter which indicates high dependency of induced resolution on parameter values.
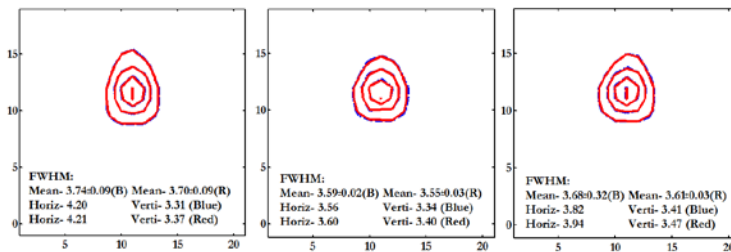
(b): Response symmetry shown as contours at 99%, 75%, 50% and 25% of the peak value at the center of the three disks for two parameter values. Responses are asymmetric and spread out with higher parameter value.

MRPs will have non-linear response and are expected to correct for the local variance problem automatically. Also, they have a robust property of edge preservation, which will solve the problem of overly smoothed edges and, further, they need only a single parameter as QPs. Their main theoretical issue of having no analytically defined derivative may be solved by using their heuristic derivatives. Figure 4.12, presents results for an implementation of LIR with MRPs, in the form of response profiles and contour maps, for two different parameter values. Theoretically, MRPs drag the final image towards its monotonic version in a local neighborhood, which contains smoothness as a subset, and the prior is non-linear so we expect automatically higher response in regions having higher count level. In other words, correction between the likelihood term and prior term would automatically be taken care of, using MRPs as the prior function. Horizontal profile image for MRPs, Figure 4.12(a), shows that the response is almost independent of β value, which is another advantage of using MRPs as an alternate prior function. Also, nonlinearity in responses, with different parameter values is corrected across the FOV in contrast to that of QPs. This supports our hypothesis that system response variations are expected to be lesser with MRPs.
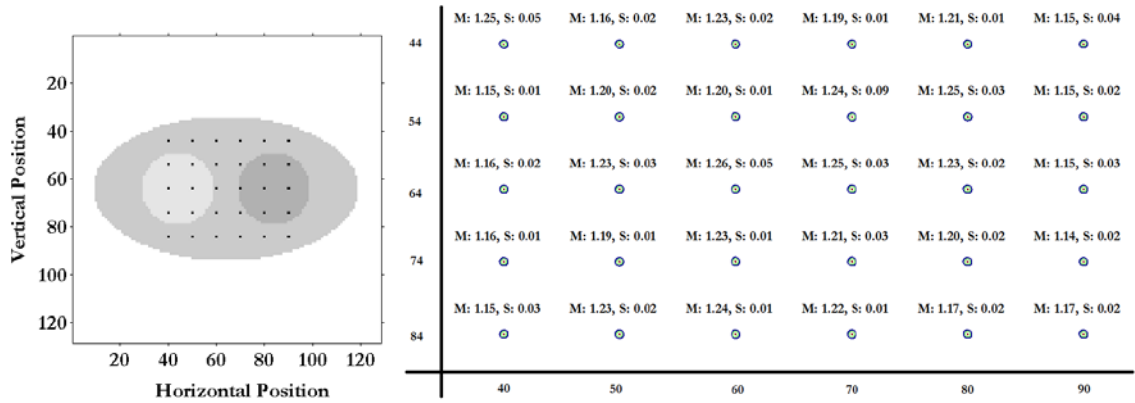
Figure 4.13: Impulse responses shown at defined sub-sampled grid of pixels with mean and standard deviation for resolution values mentioned above each contour plot.

Figure 4.13, presents results for an evaluation of LIR with MRPs for the same grid of points used in previous sections. Mean resolution in pixels and its standard deviation is given with each contour plot. Induced resolution is better as compared to the recovered resolution in case of QPs and almost uniform except near the edges. Similarly, error in the radius of the contour along all angles has been reduced. Contours are smaller and almost symmetric which resembles the results with that of ModQPs. This suggests that non-linear response of the median operator has recovered non-linearity due to varying activity and attenuation distribution, as expected. We selected a β value of 1.0 x 10^{-2}, however, because MRPs are not very sensitive to the parameter value, we found results with other parameter values almost similar.

4.8   Further Priors Design

Non-uniform smoothing behavior of QPs is more evident, especially in case of Poisson statistics, where variance equals mean of the measurements. Due to higher variance in high count regions resultant smoothing is higher and makes the ultimate response non-uniform across the FOV. On the other hand, MRPs have a non-linear behavior, robust ability to preserve edges and penalized image pixels with respect to the local median instead of neighborhood pixel differences [128]. This suggests a use of both the prior functions in some joint form. Consider LIR given by equation (4.4) as follows,

$$l^j \approx \left[diag\{s_j\} H^t_{geom}\, diag\left\{\frac{c_i^2}{y_i}\right\} H_{geom}\, diag\{s_j\} \right.$$

$$\left. + \beta \ddot{R}(f) \right]^{-1} diag\{s_j\} H^t_{geom}\, diag\left\{\frac{c_i^2}{y_i}\right\} H_{geom}\, diag\{s_j\} e^j$$

Hessian of the prior function $\ddot{R}(f)$, in this relation, can be defined for QPs as follows,

$$R(f) = \frac{1}{2} \sum_{j=1}^{j=M} \sum_{k=1}^{N_b} \omega_{jk} (\Delta f)^2$$

$$\ddot{R}(f) = \begin{cases} \sum_{k=1}^{N_b} \omega_{jk} \; for \; j = k, \\ -\omega_{jk} \; for \; j \neq k. \end{cases}$$

However, for a hybrid type of prior function, we suggest use of the following prior form,

$$R_{cp}(f) = \frac{1}{2} \sum_{j=1}^{j=M} \left(\sum_{k=1}^{N_b} \omega_{jk} (\Delta f)^2 + med(f_k | k \in N_b) \right),$$

and Hessian of this prior will be,

$$\ddot{R}_{cp}(f) = \begin{cases} \sum_{k=1}^{N_b} \omega_{jk} + {}^1/_{M_j} \; for \; j = k, \\ -\omega_{jk} \qquad\quad for \; j \neq k. \end{cases} \tag{4.7}$$

In the relation above, M_j is a median in a small local neighborhood vicinity of the pixel j. Here, we made use of heuristic definition of the derivative of MRPs. Results for an implementation of this combined prior in LIR are shown in Figure 4.14.
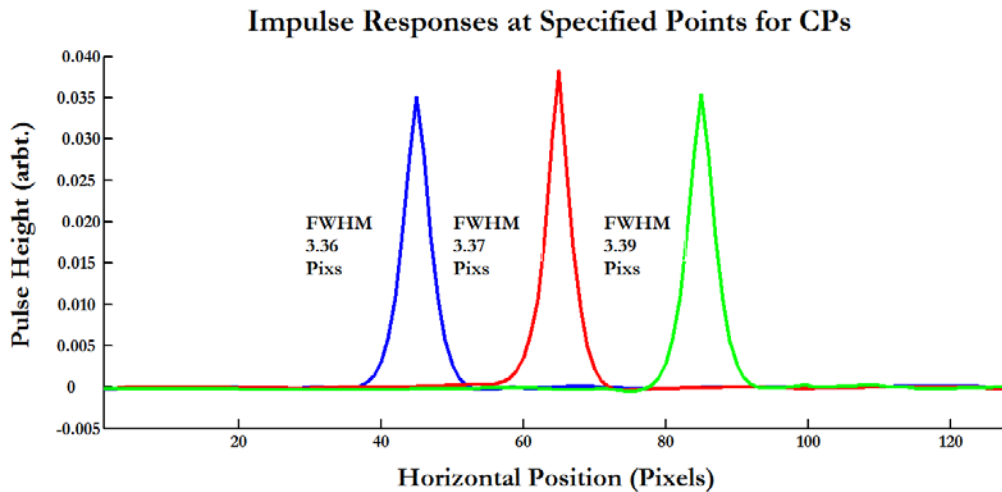
Figure 4.14: Accumulative horizontal profile through impulses at three selected points for CPs with a parameter value of 0.01. Resolution is given in FWHM in Pixels at the three points.

Responses have almost similar reconstructed resolution and non-linearity due to difference in activity concentration has almost been removed.

This figure shows that response non-linearity has been reduced and the induced resolution is better distributed uniformly, however, the responses are broader as compared to MRPs or ModQPs. This might be due to non-linear behavior and penalization based on the median operation of MRPs. We used only one β value of 1.0 x 10^{-2}, however, it is possible to use two different values for both the priors to vary their weighting accordingly, towards the final solution. This will make the response properties more controllable and in between of QPs and MRPs. Further results are needed to look for any improvements it may provide however that will be out of the scope of this thesis.

4.8.3 Certainty plus Prior-based Design

Certainty based prior design is a kind of local correction applied to the response of the system in a local neighborhood. Basic idea for this correction is to use normalized backprojection of the local certainty, or the local activity as shown in the equation below.

$$l^j \approx k_j F^{-1} \left[H_{geom}^t H_{geom} + \beta \ddot{R}(f) \right]^{-1} H_{geom}^t H_{geom} e^j$$

Here k_j is the correction term applied to the LIR to correct for local resolution control. For QPs, this relation simplifies to,

$$l^j \approx k_j F^{-1} \left[H_{geom}^t H_{geom} + \beta \ddot{R}_{qp}(f) \right]^{-1} H_{geom}^t H_{geom} e^j$$

Hessian of the prior term $\ddot{R}_{qp}$ is for the QPs. In case of MRPs this expression will become as follows,

$$l^j \approx k_j F^{-1} \left[H_{geom}^t H_{geom} + \beta \ddot{R}_{MRP}(f) \right]^{-1} H_{geom}^t H_{geom} e^j \qquad (4.8)$$

We propose the use of MRPs, with certainty based correction method for non-uniform resolution recovery. Reasons for adding certainty based correction are two folds; first to include advantages offered by the prior based method and, second corrections offered by the certainty based method. However, it should be noted that we are still correcting for interactions between the data and the prior term, $F^{-1}\ddot{R}(f)F^{-1}$, in LIR.

4.9   Application to tomography

To check, if our proposed priors and developed MRPs-MAP estimators work for real data, a sinogram acquired on a GE Infinia Dual Head gamma camera, installed at Institute of Nuclear Medicine and Oncology, Lahore, (INMOL), Pakistan, was reconstructed using QPs and MRPs as shown in Figure 4.12 [196]. We acquired a point source containing an activity concentration of 200 μCi in 4 x 4 x 2 mm, was placed at approximately -85 mm off the centre along the x-axis. A sinogram was acquired with step and shot algorithm, at 25 cm radius, with 128 views over 180⁰ around the point source, collecting 10 kCnts at each view with 128 x 128 image matrix size. A 2D sinogram acquired in x and z direction while keeping y direction constant, and keeping the point source in focus, shown in Figure 4.12, was obtained in *Interfile* format. This 2D sinogram data, reconstructed with MLEM, PLEM-QPs and PLEM-MRPs algorithms (as given in Appendix A), with resultant images is shown in the same figure. For each point source, reconstructed resolution in FWHM in pixels and in mm is shown with an estimated pixel size of 2.84 mm. We selected that value of the β parameter, which induced almost same resolution for MRPs and MLEM.
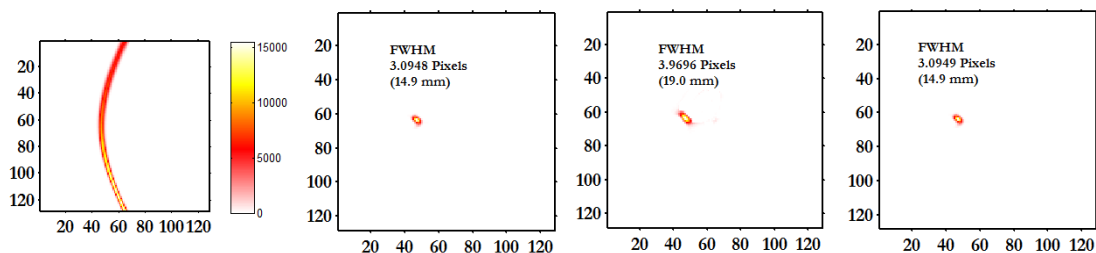
Figure 4.15: A 2D sinogram obtained from a 3D SPECT sinogram data acquired from a point source, placed -80 mm off the center, on a GE Infinia Dual Head Gamma Camera, with 128 views collected for 128 x 128 matrix size.

These images show that QPs produced heavier blur due to strong smoothing behavior and point source was spread out more, whereas, for MRPs and MLEM this spread is the minimum. It should be noted that a diagonal elongation of the point source was due to the physical shape deformation of the point source prepared in a cotton swab. Results for another real PET data set are shown in Figure 4.16. This is a CTI EXACT PET Scanner emission data, which has been pre-corrected for randoms.
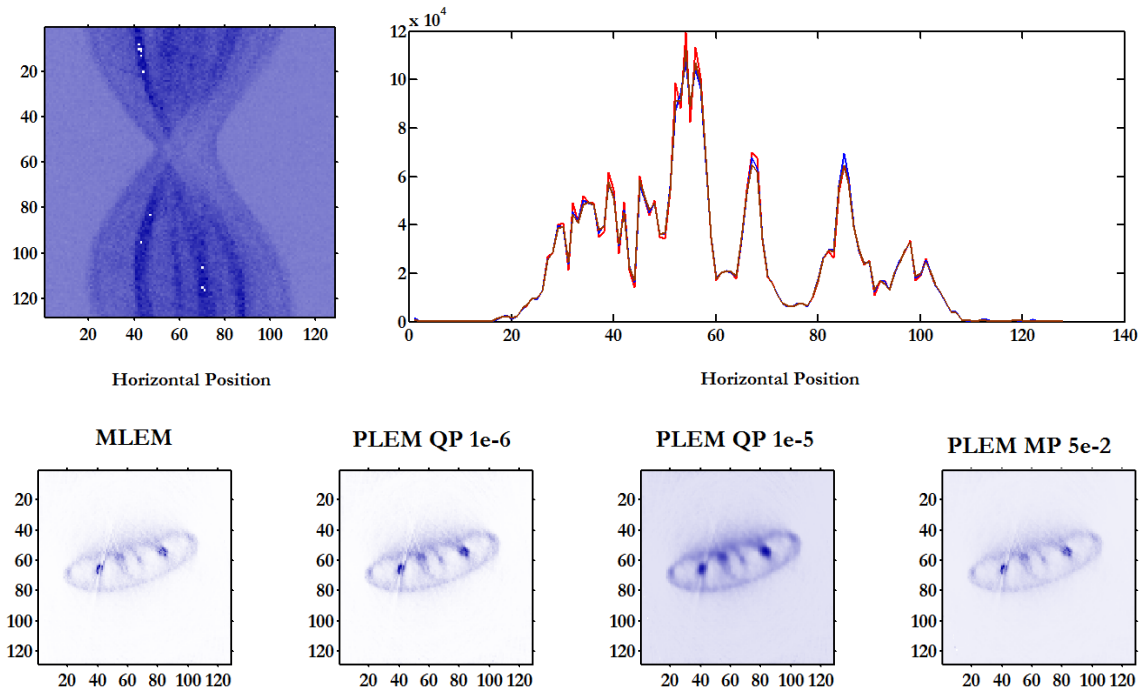
Figure 4.16: This figure shows real CTI EXACT PET sinogram data which is available for free use on J. A. Fessler's home page. This is only the emission data pre-corrected for randoms. The data file has been resized to 128 x 128 sinogram size or an easy use with our reconstruction routine.

Transmission data is also available to apply the correction; however, we have only presented results for emission data without carrying out any correction to show an application of our reconstruction routine with real data. Actual size given for the emission sinogram was 47 slices of 160 x 192 pixels, however, we have resized this data into a 128 x 128 sinogram by simple interpolation functions of Matlab to fit it for our reconstruction routine sizes. Four images, reconstructed by simple MLEM, QPs in MAP algorithm with β values of 1.0 x 10^{-6} and 1.0 x 10^{-5} and MRPs with β value of 5.0 x 10^{-2}, are shown in the bottom row. Top row presents sinogram data image at the center of the axial direction, which is 23rd slice of the data set out of 47 slices. A horizontal profile is also shown through the four reconstructed images at a height of 58 pixels. This profile image indicates that the four algorithms generate reasonable images from the data set with almost matching profiles.

4.10 Noise Effect

Noise properties of a reconstruction algorithm are closely related to their resolution characteristics [133;166]. Reconstruction methods may behave differently with noisy data and may be sensitive to the amount of noise in it. To assess this, we performed mean absolute error (MAE) test for different priors in MAP estimators to investigate their noise sensitivity by analyzing single pixel behavior near the center of the image as shown in

Figure 4.16. Altogether, 50 noisy sinogram realizations were generated by adding Poisson noise to our phantom image, with three different levels of total counts. We used a 'holes' phantom image shown in Figure 4.16. These noisy sinograms were reconstructed using QPs, MRPs and TV, and MAE for each noisy reconstruction was calculated by the following relation,

$$MAE_i = \left| \hat{f}_i - t \right| \tag{4.9}$$

Here MAE_i represents the $i-th$ mean absolute image, $\hat{f}_i$ is the $i-th$ reconstructed noisy image and t is the phantom image, with given total number of counts.
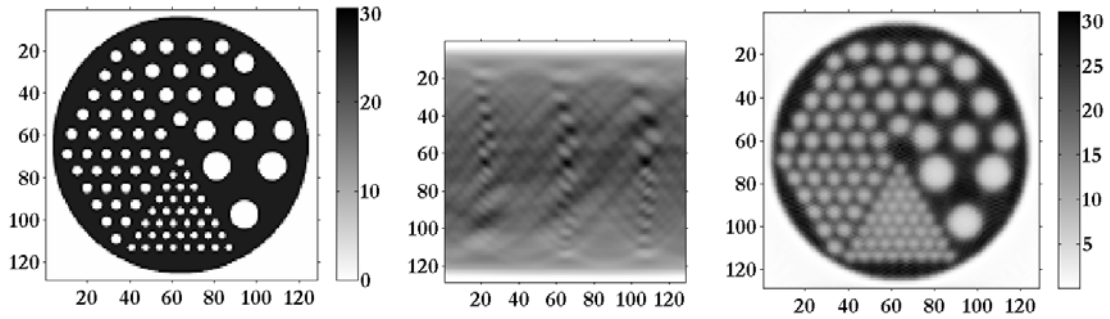
Figure 4.17: Wholes phantom image with its sinogram image and a MLEM reconstructed image. MAE was calculated for a pixel at the center of the largest cold disc near the right corner of the center.

MAE profile for an image pixel at the center of the largest cold disc inside the phantom for two different β values and three different count levels is plotted in Figure 4.17. We increased the mean number of counts per pixel in the image, to observe an increase in per pixel variance.

Table 4.2: This table presents MAE (%) for the same pixel averaged over 50 noisy realizations for three count levels and two β values.

β Value	Counts	QPs	MRPs	TV
1.0x10^{-4}	1.0x10^6	34.9	34.2	32.8
	5.5x10^5	17.2	16.9	17.3
	5.0x10^5	3.0	2.9	3.0
5.0x10^{-4}	1.0x10^6	37.5	34.2	42.2
	5.5x10^5	18.1	16.9	19.1
	5.0x10^5	3.0	2.9	3.0

Table 4.2, shows MAE values, for the same pixel, averaged over 50 noisy images. Three different noise levels have been used and an increased MAE can be observed for higher mean counts for the three priors.

MAE for noisy realizations

MAE for noisy realization
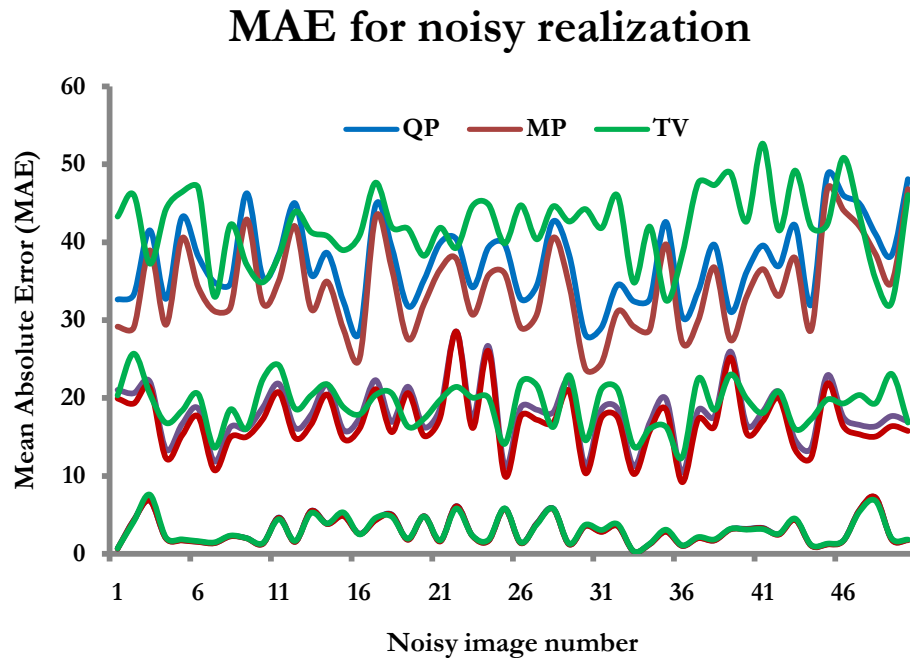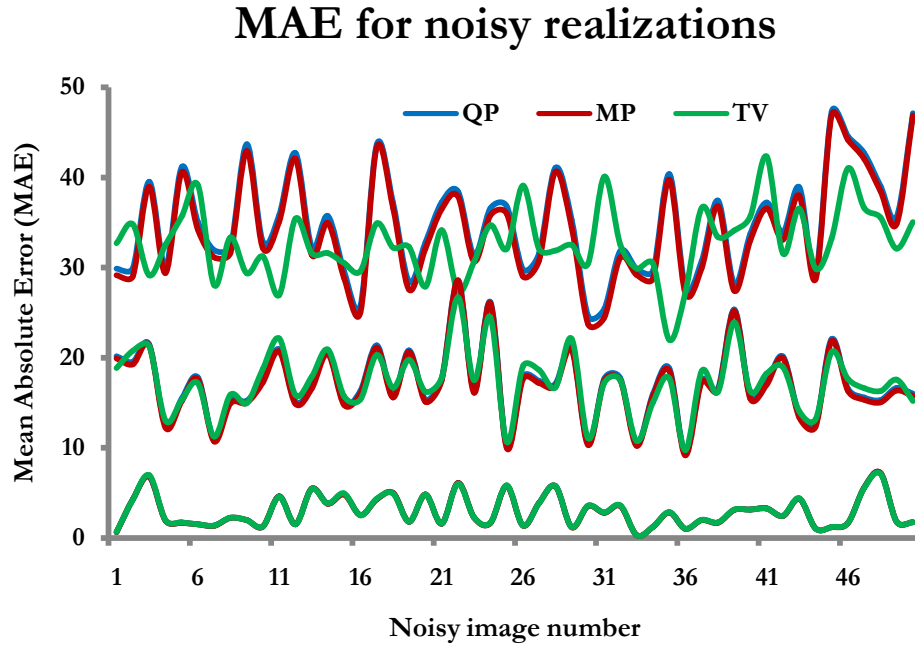
Figure 4.18: Plots showing MAE for the pixel at the center of the largest cold disc inside the phantom for three different variance levels. Top graph is for a $\boldsymbol{\beta}$ value of 1.0×10^{-4} and the bottom plot is for 5.0×10^{-4}.

At low noise level and with both parameter values, all the priors have almost similar response. However, with higher noise, QPs and TV performed worse than MRPs for

increased β value, as depicted by Figure 4.17. Table 4.2 indicates that MRPs have the most stable response as compared to the other priors, for various noise levels and β values. Hence, response of MRPs is least sensitive to these effects.

4.10.1 Iteration Based Noise Prorogation with MRPs

There are two strategy used to analyze noise propagation in the reconstructed images. Fessler (1996), analyzed noise propagation in reconstructions computed at a fixed point for a class of objective functions [168]. However, another approach followed by Barrett and Wilson (1994), tracks noise in the reconstruction at each iteration [106;197]. We extended this approach to study noise statistics in reconstructions at a specified iteration number for MAP objective function, including MRPs.

A brief derivation of the related theoretical expression to evaluate noise propagation at any selected iteration is given in this section. One-Step-Late (OSL) MAP-EM algorithm has been formulated in equation (2.24) [105],

$$f_j^{k+1} = \frac{f_j^k}{\left\{\sum_{i=1}^{M} H_{ij} + \frac{\partial}{\partial f_j} \log p_F(f^k)\right\}} \sum_{i=1}^{M} \frac{y_i}{H_{ij} f_j^k} H_{ij}$$

In vector notation we may express this algorithm as,

$$\boldsymbol{f}^{k+1} = \frac{1}{\boldsymbol{s} + \frac{\partial \log p_F(\boldsymbol{f})}{\partial \boldsymbol{f}}\Big|_{\boldsymbol{f}=\boldsymbol{f}^k}} \boldsymbol{f}^k \boldsymbol{H}^t \left[\frac{\boldsymbol{y}}{\boldsymbol{H}\boldsymbol{f}^k}\right] \tag{4.10}$$

With $\boldsymbol{s} = \boldsymbol{H}.\boldsymbol{1}$ and small-bold-face letters represent vectors and bold-capital-letters present matrices, whereas, normal-capital-letters represent random variables with bold face small letter or subscripted-small-letters as their deterministic realization vectors. Some special presentations, such as k for iteration number, are explained in the context.

4.10.1.1   Quadratic Priors (QPs)

Now, as we know, derivative of log of QPs is $\frac{\partial \log p_F(\boldsymbol{f})}{\partial \boldsymbol{f}} = \frac{\partial(-1/2\boldsymbol{f}^t\boldsymbol{R}\boldsymbol{f})}{\partial \boldsymbol{f}} = -\boldsymbol{R}\boldsymbol{f}$, equation (4.10) becomes,

$$f^{k+1} = \frac{1}{s - Rf^k} f^k H^t \left[\frac{y}{Hf^k}\right]$$

To evaluate propagation of noise through iterations, we re-write the above equation in random variables as below,

$$F^{k+1} = \frac{1}{s - RF^k} F^k H^t \left[\frac{G}{HF^k}\right]$$

Here G is considered to be a random detector measurement variable, for which y is a noisy realization, because we are studying ensemble statistics over noisy measurements. Taking log on both sides and substituting $Y^k = log\, F^k$, we get,

$$Y^{k+1} = Y^k + log\left(H^t \left[\frac{G}{HF^k}\right]\right) - log(s - RF^k) \qquad (4.11)$$

We decompose random vector F^k into mean image, or expectation a^k, and deviation from mean N_f^k, where deviation has zero mean itself, then vector $Y^k = log(a^k + N_f^k) \cong log\, a^k + \frac{N_f^k}{a^k} = log\, a^k + N_y^k$ with $N_y^k = \frac{N_f^k}{a^k}$. This is based on the approximation that signal is much larger than noise in it, or $N_y^k \ll 1$. Similarly, using mean operator $G = Hf + N$, where, N is noise in the sinogram and f is the phantom image, the second term in equation (4.11) becomes [197],

$$H^t \left[\frac{G}{HF^k}\right] = H^t \left[\frac{Hf + N}{Ha^k + H(a^k N_y^k)}\right]$$

$$= H^t \left[\frac{Hf + N}{Ha^k}\left(1 - \frac{H(a^k N_y^k)}{Ha^k}\right)\right]$$

$$\cong H^t \left[\frac{Hf}{Ha^k}\right] + H^t \left[\frac{N}{Ha^k}\right] - H^t \left[\frac{[Hf][H(a^k N_y^k)]}{[Ha^k][Ha^k]}\right]$$

$$log\left\{\frac{G}{HF^k}\right\} = log\left\{H^t \left[\frac{Hf}{Ha^k}\right] + H^t \left[\frac{N}{Ha^k}\right] - H^t \left[\frac{[Hf][H(a^k N_y^k)]}{[Ha^k][Ha^k]}\right]\right\}$$

$$\cong log\left\{H^t \left[\frac{Hf}{Ha^k}\right]\right\} + \frac{H^t \left[\frac{N}{Ha^k}\right] - H^t \left[\frac{[Hf][H(a^k N_y^k)]}{[Ha^k][Ha^k]}\right]}{H^t \left[\frac{Hf}{Ha^k}\right]}$$

$$\cong log\left\{H^t \left[\frac{Hf}{Ha^k}\right]\right\} + \frac{H^t \left[\frac{N}{Ha^k}\right] - H^t \left[\frac{[H(a^k N_y^k)]}{[Ha^k]}\right]}{s}$$

And the third term in equation (4.11) may be evaluated as,

$$s - \beta RF^k = s - \beta R(\mathbf{a}^k + N_y^k) = s - \beta R\mathbf{a}^k - \beta RN_y^k$$

Taking log of both sides of these equations will be,

$$log(s - \beta RF^k) = log(s - \beta R\mathbf{a}^k - \beta RN_y^k) \cong log(s - \beta R\mathbf{a}^k) - \frac{\beta RN_y^k}{s - \beta R\mathbf{a}^k}$$

Inserting these values into the equations (4.11), we get for QPs,

$$\begin{aligned} log\, \mathbf{a}^{k+1} + N_y^{k+1} \\ = log\, \mathbf{a}^k + N_y^k \\ + log\left\{H^t\left[\frac{Hf}{H\mathbf{a}^k}\right]\right\} + \frac{H^t\left[\frac{N}{H\mathbf{a}^k}\right] - H^t\left[\frac{\left[H(\mathbf{a}^k N_y^k)\right]}{[H\mathbf{a}^k]}\right]}{s} - log(s - \beta R\mathbf{a}^k) \\ + \frac{\beta RN_y^k}{s - \beta R\mathbf{a}^k} \end{aligned}$$

Equating random and deterministic terms to each other on both sides,

$$log\, \mathbf{a}^{k+1} = log\, \mathbf{a}^k + log\left\{H^t\left[\frac{Hf}{H\mathbf{a}^k}\right]\right\} - log(s - \beta R\mathbf{a}^k) \qquad (4.12)$$

and,

$$N_y^{k+1} = N_y^k + \frac{H^t\left[\frac{N}{H\mathbf{a}^k}\right] - H^t\left[\frac{\left[H(\mathbf{a}^k N_y^k)\right]}{[H\mathbf{a}^k]}\right]}{s} + \frac{\beta RN_y^k}{s - \beta R\mathbf{a}^k} \qquad (4.13)$$

Equations (4.12) and (4.13) can be used to evaluate ensemble mean $\mathbf{a}^k$, by running noise free MAP-EM algorithm till k iterations, from phantom image f. Further these equations present update linear relation to find noise propagation in the log of reconstructed image at iteration k. Because we do not know the noise N, in the sinogram these equations need further modifications to find the final noise expressions. Equation (4.13) can be re-arranged as follows,

$$N_y^{k+1} = B^k N + [C^k - A^k] N_y^k. \tag{4.14}$$

Where B, C and A, are implicitly defined matrices as,

$$B^k N = \frac{H^t \left[\frac{N}{Ha^k}\right]}{s}$$

$$C^k N_y^k = \frac{\beta R N_y^k}{s - \beta R a^k}$$

$$A^k N_y^k = \frac{H^t \left[\frac{[H(a^k N_y^k)]}{[Ha^k]}\right]}{s}$$

Using component notation for matrix multiplication and division as, $ab = diag(a)b$ and $a/b = diag\left(\frac{1}{b}\right)a$, we can write matrices B, C and A for QPs as follows,

$$B^k = diag\left(\frac{1}{s}\right) H^t diag\left(\frac{1}{Ha^k}\right)$$

$$C^k = diag\left(\frac{\beta R}{s - \beta R a^k}\right) \tag{4.15}$$

$$A^k = diag\left(\frac{1}{s}\right) H^t diag\left(\frac{1}{Ha^k}\right) H diag(a^k)$$

4.10.1.2   Median Root Priors (MRPs)

For MRPs we will obtain, $\frac{\partial \log p_F(f)}{\partial f} = -\frac{(f_j - M)}{M} = -\left(\frac{f}{m}\right) + 1$, with m as vector of medians and of length of the image vector, hence, equation (4.10) will become,

$$f^{k+1} = \frac{1}{s + \beta\left(1 - f^k/m^k\right)} f^k H^t \left[\frac{y}{Hf^k}\right]$$

Indicating random variables with capitals and deterministic variables by small letters for image vector f and data vector y and taking log on both sides we get,

$$Y^{k+1} = Y^k + \log\left(H^t \left[\frac{G}{HF^k}\right]\right) - \log\left(s + \beta - \beta\frac{F^k}{m^k}\right) \tag{4.16}$$

Second term in the above relation would become,

$$log\left\{H^t\frac{G}{HF^k}\right\} = log\left\{H^t\left[\frac{Hf}{Ha^k}\right] + H^t\left[\frac{N}{Ha^k}\right] - H^t\left[\frac{[Hf][H(a^kN_y^k)]}{[Ha^k][Ha^k]}\right]\right\}$$

$$\cong log\left\{H^t\left[\frac{Hf}{Ha^k}\right]\right\} + \frac{H^t\left[\frac{N}{Ha^k}\right] - H^t\left[\frac{[Hf][H(a^kN_y^k)]}{[Ha^k][Ha^k]}\right]}{H^t\left[\frac{Hf}{Ha^k}\right]}$$

$$\cong log\left\{H^t\left[\frac{Hf}{Ha^k}\right]\right\} + \frac{H^t\left[\frac{N}{Ha^k}\right] - H^t\left[\frac{[H(a^kN_y^k)]}{[Ha^k]}\right]}{s}$$

Third term will simplify to,

$$(s+\beta) - \beta\frac{F^k}{m^k} = (s+\beta) - \beta\left(\frac{a^k}{m^k} + \frac{N_y^k}{m^k}\right)$$

Taking log of this term,

$$log\left(s + \beta - \beta\frac{F^k}{m^k}\right) = log\left((s+\beta) - \beta\left(\frac{a^k}{m^k} + \frac{N_y^k}{m^k}\right)\right)$$

$$\cong \mathbf{log}\left((s+\beta) - \beta\frac{a^k}{m^k}\right) - \frac{N_y^k}{\left(s/\beta + 1\right)m^k - a^k}$$

Putting these two values in equation (4.16) for MRPs, we get,

$$log\, a^{k+1} + N_y^{k+1} = log\, a^k + N_y^k + log\left\{H^t\left[\frac{Hf}{Ha^k}\right]\right\} + \frac{H^t\left[\frac{N}{Ha^k}\right] - H^t\left[\frac{[H(a^kN_y^k)]}{[Ha^k]}\right]}{s}$$

$$- log\left((s+\beta) - \beta\frac{a^k}{m^k}\right) + \frac{N_y^k}{\left(s/\beta + 1\right)m^k - a^k}$$

Equating random and non-random terms on both sides separately, we get,

$$log\, a^{k+1} = log\, a^k + log\left\{H^t\left[\frac{Hf}{Ha^k}\right]\right\} - log\left((s+\beta) - \beta\frac{a^k}{m^k}\right) \qquad (4.17)$$

$$N_y^{k+1} = N_y^k + \frac{H^t\left[\frac{N}{Ha^k}\right] - H^t\left[\frac{[H(a^kN_y^k)]}{[Ha^k]}\right]}{s} + \frac{N_y^k}{\left(s/\beta + 1\right)m^k - a^k} \qquad (4.18)$$

and, equation (4.18) can be used to evaluate value of N_y^{k+1} using constants B, C and A, implicitly defined matrices as,

$$B^k N = \frac{H^t \left[\frac{N}{Ha^k} \right]}{s}$$

$$C^k N_y^k = \frac{N_y^k}{\left(\frac{s}{\beta} + 1 \right) m^k - \mathbf{a}^k}$$

$$A^k N_y^k = \frac{H^t \left[\frac{[H(a^k N_y^k)]}{[Ha^k]} \right]}{s}$$

Using component notation for matrix multiplication and division as, $\mathbf{ab} = diag(\mathbf{a})\mathbf{b}$ and $\frac{a}{b} = diag\left(\frac{1}{b} \right) \mathbf{a}$, we can write matrices B, C and A for MRPs as,

$$
\begin{aligned}
B^k &= diag\left(\frac{1}{s} \right) H^t diag\left(\frac{1}{Ha^k} \right) \\
C^k &= diag\left(\frac{1}{\left(\frac{s}{\beta} + 1 \right) m^k - \mathbf{a}^k} \right) \\
A^k &= diag\left(\frac{1}{s} \right) H^t diag\left(\frac{1}{Ha^k} \right) H diag(\mathbf{a}^k).
\end{aligned}
\tag{4.19}
$$

4.10.1.3   Noise Statistics

Generally, a uniform image is used as a starting object for the MAP-EM algorithm, $N_y^0 = 0$ and the recursive relation may be summed to yield,

$$N_y^k = U^k N \tag{4.20}$$

Where a $M \times N$ matrix U^k would satisfy the recursive relation below, and depends only on the deterministic parameters of the algorithm, such as system matrix, iteration number, noise free estimate and the object itself and its median image at each iteration.

$$U^{k+1} = B^k + \left(C^k - A^k \right) U^k \ \ with \ U^0 = 0 \tag{4.21}$$

Noise in the reconstruction at $k - th$ iteration depends on the noise in the sinogram through U^k as,

$$N_f^k = a^k N_y^k = diag(a^k) N_y^k = diag(a^k) U^k N$$

Given the Poisson nature of the emission process, random variable G representing projection measurements, considered as independent Poisson distribution, and have mean Hf. The forward projection model may be given by $G = Hf + N$, where object dependent noise, N has conditional mean zero. The conditional covariance matrix N or $E[N^t N|f]$ is same as the conditional covariance matrix of G which is $E[(G - E[G])(G - E[G])^t|f]$. It is a diagonal and symmetric matrix with $i - th$ diagonal element representing the covariance of G_i or [106;197],

$$E[N^t N|f] = E[(G - E[G])(G - E[G])^t|f] = diag(Hf)$$

Now, the covariance matrix of $F|f$ is also the covariance matrix of $N_f^k|f$ or

$$
\begin{aligned}
Cov_{F|f}^k &= E\left[N_f^k (N_f^k)^t |f\right] \\
&= diag(a^k) Cov_{N_y|f}^k diag(a^k) \\
&= diag(a^k) U^k Cov_{N|f}^k (U^k)^t diag(a^k) \\
&= diag(a^k) U^k diag(Hf)(U^k)^t diag(a^k),
\end{aligned}
$$

and the $(i, j) - th$ element of this matrix will be,

$$\left[Cov_{F|f}^k\right]_{ij} = a_i^k a_j^k \sum_m [U^k]_{im} [U^k]_{jm} [Hf]_m \tag{4.22}$$

Diagonal of this matrix represents the variance image reconstructed at the $k - th$ iteration. This equation gives the noise statistics of the algorithm with MRPs or the QPs with suitably calculated U matrix.

4.10.2 Monte-Carlo Validation of the Derivation

We simulated large number of noisy images, for Monte-Carlo evaluation of mean and variance images, by applying a Poisson random number generator to the noiseless sinogram data. Sample mean of T number of noisy images was evaluated at iteration k as follows,

$$F^k = \frac{1}{T} \sum_{t=1}^{T} f_t^k \qquad (4.23)$$

Whereas sample covariance was calculated by,

$$Cov^k = \frac{1}{T-1} \sum_{t=1}^{T} (f_t^k - F^k)(f_t^k - F^k)^t \qquad (4.24)$$

For theoretical noise statistics, we reconstructed noise free estimates a^k of the object for various iteration numbers for $iteration = 1, \ldots, k$, and then evaluated U^k using required parameters, such as system matrix H and object f, to get the covariance matrix. A variance image is simply the main diagonal of the covariance matrix. The conditional mean is a^k for the specific iteration number.

To validate above relations, 100 noisy sinogram realizations have been generated, by inducing Poisson noise with 10^6 total counts, for our simulated phantom image. These sinograms were reconstructed by MAP reconstruction method using three priors for 30 iterations and mean and variance images have been calculated. Figure 4.18
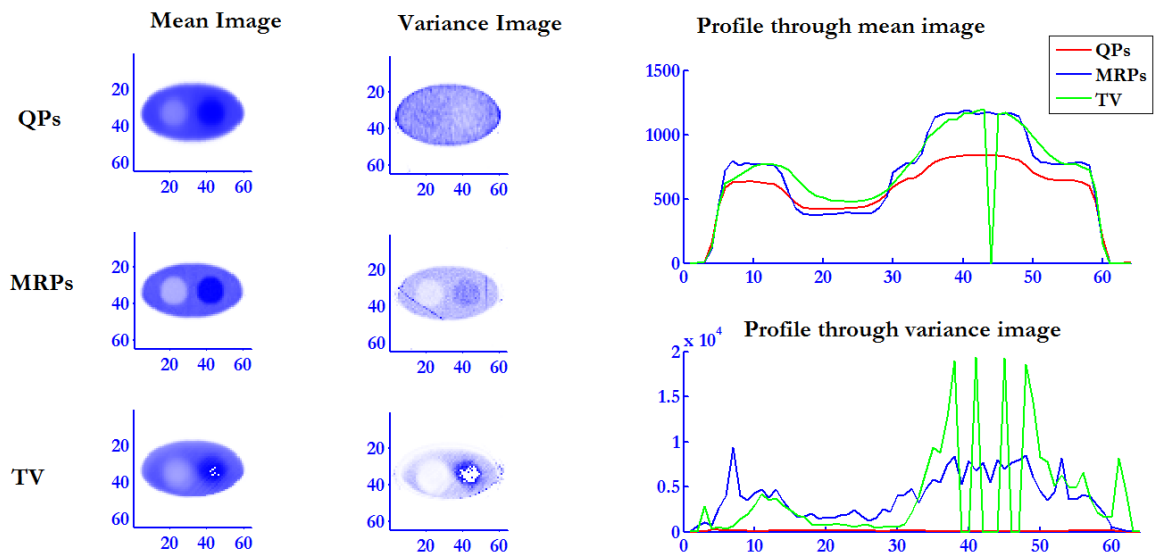
Figure 4.19: Mote-Carlo mean and variance images for various priors with a parameter value of 5.0×10^{-4} for QPs and MRPs and 1.0×10^{-4} for TV regularization.

shows that mean images for QPs are smoothed out whereas smoothing is not so strong for MRPs and TV, with better edge definition with MRPs. Horizontal profiles through mean

images indicate a similar trend. MRPs present least smoothed mean profile. TV has also smoothed out the image more than MRPs, which may be due to the parameter η. Profiles through variance images, shown in Figure 4.19 for theoretical expressions, also indicate that MRPs behave better than other priors. Low variance level for QPs may be attributed to higher smoothing than better noise properties.

4.11 Summary

Tomographic imaging systems suffer from various image degrading effects. These effects cause response of these systems to be space-variant. Iterative methods have an ability to explicitly model these effects, as compared to the analytical methods; however, they lead to noisy images, because they consider information only based on noisy data. Implicit regularization techniques, added to these methods, can reduce this noise, but unluckily, have least resolution control [72;141;164]. MAP reconstruction algorithms are better suited to recover for this space-variance in response of the system, due to the application of an explicit form of regularization with prior object knowledge, which can also be used to reduce noise in the reconstructions and for better control over their reconstructed resolution and noise properties. Smoothing prior functions are commonly used in MAP algorithm; however, they have a notorious problem of anisotropic smoothing behavior [26].

In this chapter, we have analyzed and compared reconstructed resolution and noise properties of various priors, included in MAP algorithm, with simulated and real data. Initial results, for hyper-parameter tuning, indicate that MRPs are less sensitive to the value of this parameter, as compared to the standard QPs and TV regularization. Further, our qualitative analysis with simulated thorax chest phantom data, suggests that MRPs perform better, in terms of correctness and preciseness, as compared to the other regularization priors and produce images close to MLEM, whereas, QPs and TV produce over smoothing and patchy effects.

Resolution properties of the reconstructed images were evaluated in terms of response linearity, uniformity and symmetry for different priors with brute force empirical method and LIR analysis methods. MRPs have better linearity and uniformity of the response function and reconstructed resolution is less sensitive to the parameter value, though, various priors behave almost similar in terms of anisotropic smoothing characteristics, whereas blurring is the least for MRPs. LIR evaluations indicated that resolution is less non-uniform and with better recovered resolution, for MRPs as compared to QPs. The non-uniform resolution response is due to the non-uniform FIM in LIR.
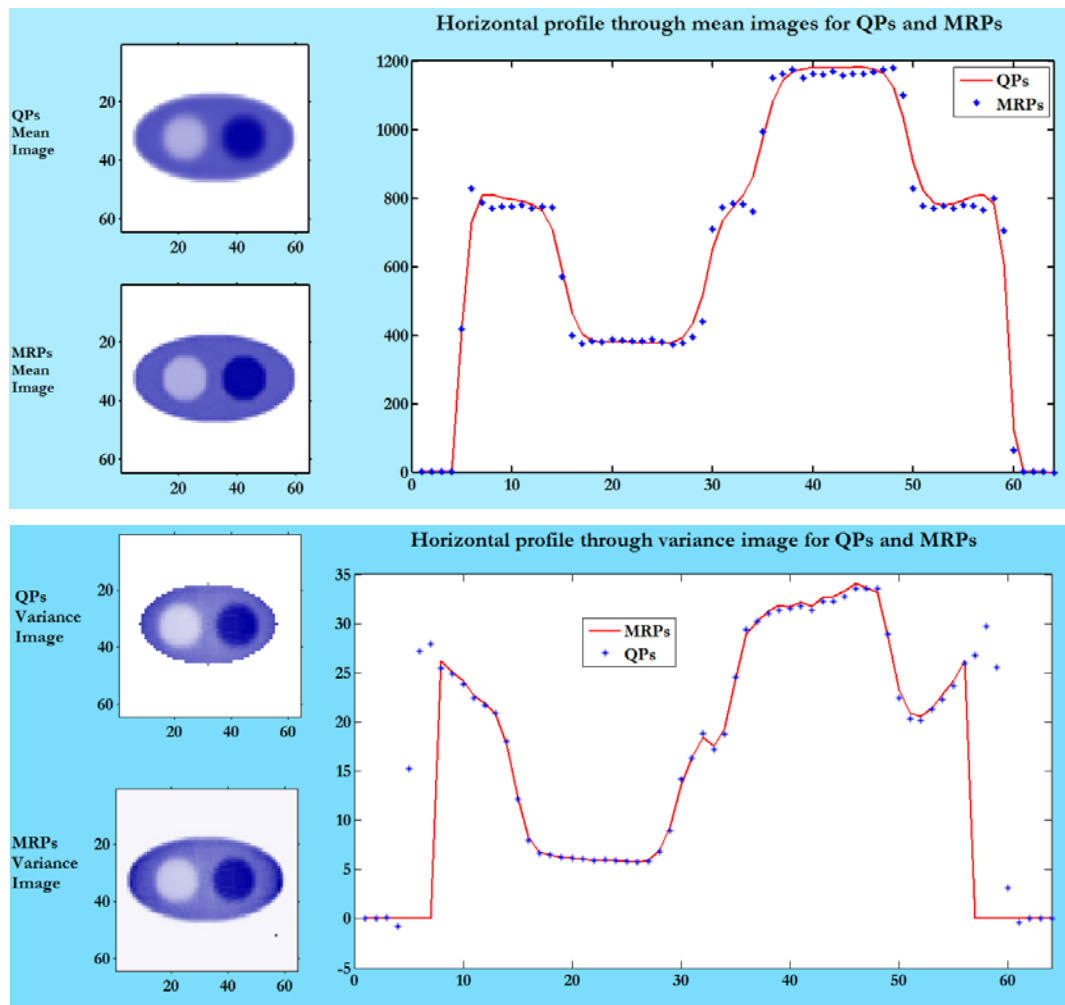
Figure 4.20: Profile images through mean and variance images for QPs and MRPs using theoretical formulae.

Certainty based correction method, developed for PLEM methods including QPs, was implemented to produce better responses with QPs and we developed a similar approach to introduce a simple prior based correction method, using MRPs. Non-linear response of MAP with MRPs helps in reducing non-linearity and non-uniformity in the spatial resolution characteristics of the reconstructed images. Extending this approach further, we suggested use of an average behavior of both QPs and MRPs in the form of Combined Priors (CPs). Results indicate that these hybrid priors have a response in between of median and quadratic priors. A combination of certainty based and prior based corrections has also been analyzed, with a conclusion that MRPs have an ability to compensate for non-uniform resolution with better correction for nonlinearity, non-uniformity, and asymmetry and parameter sensitivity.

Noise analysis is, commonly, carried out for a fully converged solution or solution obtained after a specific number of iterations. To analyze behavior of MRPs with noisy data, we opted for iteration based analysis, because, these algorithms are generally run for a

certain number of iterations. Analytical expressions were derived for the propagation of noise through iterative process with MAP algorithm, including MRPs, after a certain number of iterations. These expressions were validated using Monte-Carlo methods, through an evaluation of mean and variance images. Results indicated that QPs have higher blurring effect than reducing the noise in the reconstructed images. In conclusions, if uniform resolution across the FOV is desirable, then MRPs, produce images with better quality and lesser system variations.

CHAPTER 5

Partial Volume Correction

A promising efficacy of emission computed tomography (ECT) is the ability to measure underlying tissue activity concentration. However, accuracy of measuring this activity is limited due to finite resolution capabilities of these imaging systems and resulting partial volume effect (PVE) [34;41;42]. Resolution properties of the reconstructed images are closely related to the ability, of the reconstruction methods and ultimately of the imaging system to recover for PVE. In previous chapter, methods have been proposed to recover for non-uniform reconstructed resolution. Here, we show an implementation of two very popular PVC methods, with MAP estimators. We present results of our proposed MRPs based, priors in MAP estimators and compare them with standard QPs [31].

5.1   Geometric Transfer Matrix (GTM) Method

A very popular and vastly used method for PVC is due to Rousset et al. (1998) [41]. Certain variations of this method have been developed, however, their basic theme is still the same [38;169]. This method was initially developed for quantification of the brain images; however, it can be used for other body organs, too. This method uses three basic assumptions; (i) a linear transformation among mutually exclusive regions inside the object, (ii) homogenous activity concentration distribution inside a single region and (iii) a spatially-invariant system response. These assumptions are not natural; still this method results in relatively good recovery values for regional quantification, with linear reconstruction methods such as FBP [41]. This method is known as geometric transfer matrix (GTM) method and in the following we briefly describe the theory behind it.

Suppose our object is divided into N number of different tissue domains, represented by $D_i, (i = 1,2, \ldots, N)$ and that the true activity concentration level, represented by $A_i, (i = 1,2, \ldots, N)$ inside the $i - th$ domain is considered to be homogeneous within that domain or region. Then, activity concentration of the object f, being imaged is assumed to be a linear sum of all the activity concentrations within those regions,

$$f = \sum_{1}^{N} A_i z_i \tag{5.1}$$

In this equation, z is 1, if the point of interest lies inside the $i - th$ domain, and 0 else where. Rousset proposed considering restricted domains to be convolved with the system's PSF, instead of the whole image to obtain regional projections termed as regional spread functions (RSF) [41]. A regional projection RSF_i of the $i - th$ domain through the object can be thought of as a linear superposition of the true activity concentrations in all the regions. In this case, the mean observed activity concentration for a $j-th$ region or ROI$_j$ can be stated as;

$$RSF_j = \sum_{i=1}^{N} w_{ji} A_i$$

Matrix W is called the geometric transfer matrix (GTM) and its elements w_{ij} represent activity transfer coefficients in region i into another region j. Diagonal elements of this matrix represent self contamination of each region by its own activity concentration while off diagonal terms give inter-regional contamination. If matrix W is known then the true activity concentrations vector A may be recovered by inverting this matrix and solving the following equations.

$$A = W^{-1}T$$
$$Var = (W^2)^{-1}V \tag{5.2}$$

Here V is a vector representing the variance in each domain D_i and T is vector of measured mean activity concentrations and A is a vector of true mean activities in all regions calculated using above equation. Elements of matrix W can be estimated by the following method [198].

$$w_{ij} = \frac{1}{N_j} \{ROI_j \cdot Rec[Proj(ROI_i)]\} \tag{5.3}$$

ROI_i is the image vector of the $i - th$ ROI filled with unit activity, forward projected and then reconstructed back into an image. This reconstructed image is then multiplied

using dot product "•" operator with a binary vector of the $j-th$ ROI. N_j is the total number of pixels in the $j-th$ ROI.

5.1.1   Digital Simulated Phantom

We used our 128 x 128 pixels digital phantom image as shown in Figure 5.1 for our analysis, assuming 128 detector bins per view and 128 views over 180°, using pixel size equal to that of the detector bin, in parallel beam geometry. This phantom has two discs with low and high activity, termed as ROI1 and ROI3, embedded in a moderately active background disc, termed as ROI2, with a relative activity concentration ratio of 1.0, 2.0 and 3.0, respectively. A much smaller region ROI4 with relative activity concentration of 4.0 was added to observe PV effect, when object size approaches system's reconstructed resolution. With inclusion of this small region our phantom was now able to compare the effect of PVE for different reconstruction algorithms, with varying sized objects and varying activity concentrations. Two larger discs were added to study the effect of varying activity concentration, as compared to the background on the PVE and the smaller disc was added to observe the effect of object size. This smallest disc also contains very high activity concentration as compared to the background and is expected to show the maximum PVE due to higher spill-over effects. Otherwise the phantom is almost same as described in the previous chapter for consistency. Image was segmented by intensity threshold method to define regions. This simulated phantom, with defined regions is shown in Figure 5.1.
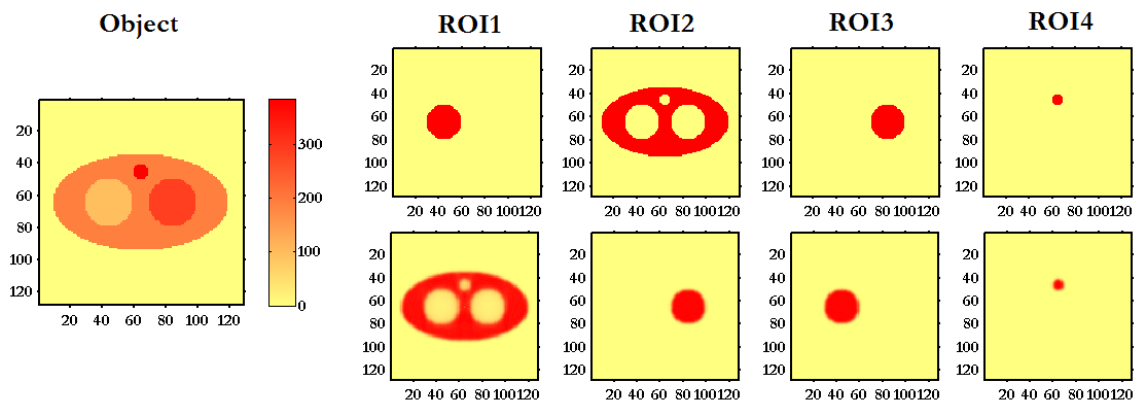
Figure 5.1: Digital simulated phantom used for PVC analysis with definition of ROIs (ROI 1, 2, 3 and 4 from left to right). ROI 4 was added to observe the PV effect when object size approaches comparably to the system reconstructed resolution. Bottom row show reconstructed images of these ROIs.

A simple PET system with line integral model, as discussed in Chapter 4, was used to evaluate activity recovery performance. We ignored any scattering or randoms, however,

evaluated recovery performance of MAP estimator with different priors with or without attenuation added and a Gaussian blur of 3.5 pixels FWHM was applied to the sinogram along the radial direction. Images were reconstructed with OSL-MAP versions of the QPs and MRPs. Two hyper-parameter values have been selected to have a very low and a reasonably high smoothing, at the center of the image. We also compared the performance in terms of Percentage Bias values for the estimated mean pixel activity concentration in a region, relative to the true values as defined by the following formula [38;198;199],

$$Bias\ (\%) = \frac{A_{est} - A_{true}}{A_{true}} \times 100 \qquad (5.4)$$

Underestimated values will produce negative bias and overestimated values will result in positive bias. Small discs of radii of 15 pixels and 5 pixels have been placed inside the large elliptical background disc of radii 30 and 55. The smallest disc has a relative size of within 3 to 4 times of the system resolution. Other two discs are large enough and should show only a difference of the edge pixels.

5.1.2   Activity Recovery Performance

Figure 5.2 presents our results for an implementation of GTM method with QPs and MRPs in MAP estimators and compares activity recovery performance of these priors with line intersection length model. Without attenuation correction, recovered activities are heavily underestimated for all the discs and negative bias values were obtained from -25% to 70%, hence these results are not shown here. These very high bias values mean that, if attenuation correction is not performed, activity recovery will be heavily undermined.
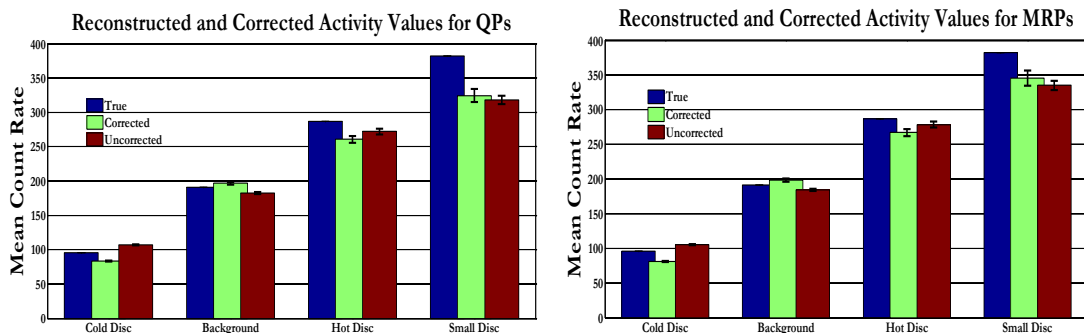
Figure 5.2: Activity recovery performance of QPs and MRPs in GTM method, with attenuation correction performed, for various disks defined in our digital phantom image. Vertical axis represents mean counts per pixel and error bars indicate variance in each region.

However, with attenuation correction applied for QPs, measured values show a spill-out from the hot disc and spill-into the cold disc from the background disc, respectively. An accumulative effect, in the background disc is a spill out of the activity from this disc. In smaller hot disc, a heavier spill-out can be seen because of higher PVE due to its size comparable to the system FWHM. Similar behavior can be observed, in case MRPs; however, in the smallest hot disc recovery is better as compared to QPs.

Table 5.1: Integrated activity values in various ROIs, represented as GTM

	Cold Disc	Background	Hot Disc	Small Disc
Cold Disc	93.2 %	1.2 %	0.0 %	0.0 %
Background	14.9 %	90.0 %	14.9 %	31.2 %
Hot Disc	0.0 %	1.25 %	93.2 %	0.0 %
Small Disc	0.0 %	0.4 %	0.0 %	79.0 %

A typical GTM matrix is shown in Table 5.1 below for QPs with parameter value of 1.0 x 10^{-4}. For example, for background disc 90.0% of the activity remains inside the disc, whereas 1.2% spilled into the cold disc and 14.9% and 31.2% spilled into this disk from the hot disc and the small disc, respectively. Our modified priors (ModMRPs), defined in previous chapter, provided almost similar results for activity recovery performance, as depicted by Figure 5.3. There was one exception though, that both the modified priors have almost equal and higher sensitivity to β value and produce highly underestimated values for the mean regional activities with higher parameter values.
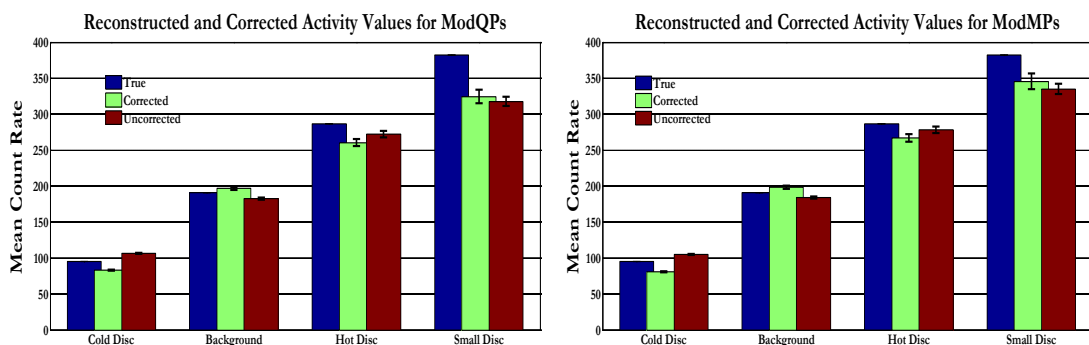
Figure 5.3: Activity recovery performance of ModQPs and ModMRPs in GTM method, for various disks defined in our digital phantom image, with attenuation correction performed. Vertical axis represents mean counts per pixel and error bars indicate variance in each region.

5.2 %Bias and Noise Analysis

Figure 5.4, presents results for Percentage Bias obtained using both the priors and with and without attenuation correction applied.
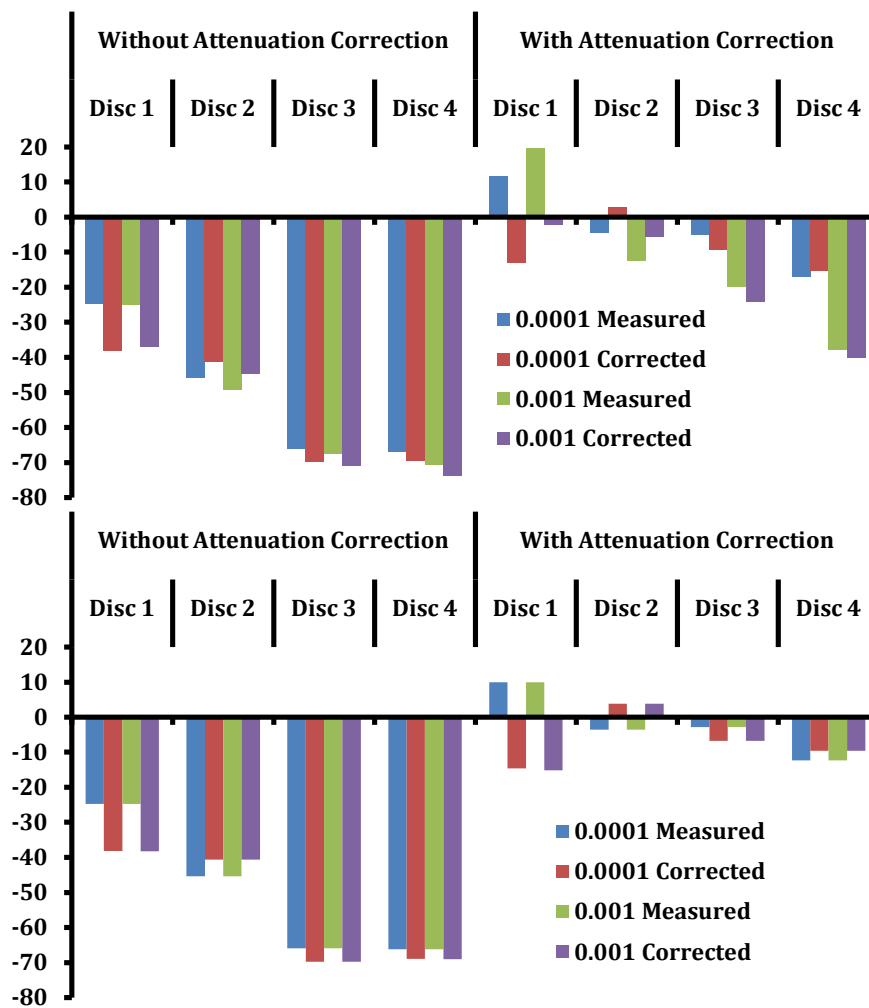
Figure 5.4: Bias (%) performance of QPs (top) and MRPs (bottom) applied in GTM method for various regions defined in our phantom image.

Results are highly underestimated without the application of attenuation correction and bias values range from 25% to 70%, in negative, for various priors and β parameter values. Hence, it is crucial to include attenuation correction, before any activity quantification is carried out.

With attenuation correction performed, highest activity underestimation is in the smallest hot disc with QPs bearing a negative bias value of -17% which recovered to -15% after PVC. These low recovery factors are probably due to a very simple system matrix used and very low blur induced to the sinogram. However, MRPs performed better both in measured values before correction and after PVC applied. Almost similar behavior of both the priors is evident for other regions though values with QPs are much more sensitive to the parameter value. This is most probably due to the smoothing behavior of quadratic regularization.

Table 5. 2: Noise performance of QPs and MRPs with GTM

	True	Corrected	Measured
QPs			
Cold Disc	96	89 ± 11	111 ± 10
Background	191	185 ± 5	172 ± 5
Hot Disc	287	252 ± 13	263 ± 11
Small Disc	382	280 ± 66	279 ± 51
MRPs			
Cold Disc	96	89 ± 12	112 ± 11
Background	191	194 ± 6	180 ± 5
Hot Disc	287	267 ± 15	278 ± 13
Small Disc	382	303 ± 78	300 ± 61

Table 5.2, briefly presents noise performance of QPs and MRPs with GTM method for PVC. Mean recovered values are generated using 30 noisy realizations of the true phantom. Noisy sinograms were generated by adding Poisson noise to the true phantom sinogram, and finally the mean recovered regional activities along with their standard deviations were calculated as average of these 30 reconstructions. Recovered activity values are closer to the true values for MRPs as compared to the QPs except for the cold disc embedded in a relatively higher activity background disc.

5.3   Discussion

In this section, we presented our results for an implementation of various priors in a popular PVC method known as GTM. This method assumes that the object activity, as a whole, can be represented as a linear superposition of regional activities present inside the object, and uses an analytical simulator to evaluate regional spread functions and high resolution anatomical images to recover mean regional activity values. The assumption of linear superposition is not natural and only valid, till, we define mutually exclusive regions which make up, collectively, the whole image. For mutually non-exclusive regions the GTM will not be singular and noninvertible, hence, cannot be used to recover true activities. An implicit noise distribution has been taken into account in the original method, whereas, for comparison of various priors in MAP algorithm, we used, explicitly, Poisson noise, and our work differs here from simple FBP based GTM method [41]. This method assumes a stationary system response which is impractical, because, all real scanners have a spatially variant response [29]. However, it has been observed that this type of non-linearity will affect the results most, if correction for spatially varying detector response function (DRF) is included in the system matrix, which is not a problem in our experiments, because for

comparison of our priors, we assumed a very simple system model which ignores these corrections. Methods have been proposed to evaluate perturbed regional spread functions (pRSF), instead of RSF, to correct for space variant resolution response, though, the results are similar to simple GTM without DRFs correction. GTM method depends on matrix inversion to recover for true regional activities, whereas, any kind of matrix inversion amplifies the noise in the data and our results show the same. Error in recovered regional activity values increases as compared to the measured values for regional activity concentrations. Another very basic problem with this method is an increased computational complexity with an increase in the number of regions, in which the object is divided [33;38;39;41;172]. In our experiments, only four regions have been considered which is not very large. Some extensions of the method have been suggested to reduce the region size to a single pixel and to evaluate the method for PVC images, however, computational burden and size of the problem becomes huge and difficult to handle [173]. Another problem with this method is induced error due to segmentation and registration errors, which is not serious in our experiments because we used true definitions of the ROIs.

Our results indicate that both, QPs and MRPs, can recover regional activity values, when used in MAP reconstruction methods for an implementation of GTM method. QPs produce more smooth images and, hence activity recovery performance of these priors is more sensitive to β parameter values, as compared to MRPs. Recovered activity concentration is better in case of MRPs as compared to the QPs, which could be due to their better comparative edge preserving capability and lower or selective smoothing behavior.

5.4   Statistical Methods for PVC

A partial volume correction method based on statistical properties of the data has been developed by Aston *et al.*, (2002) [42]. We implemented various priors in this statistical PVC method and compared relative performance of QPs and MRPs. Statistical PVC methods try to take into account the signal distribution and underlying noise structure. They have considered both correlated and uncorrelated noise structures under various noise distributions. They claim that their method is independent of the assumption of activity homogeneity in a particular region. They have shown relationship of their method to the GTM and Labbe's methods for PVC. We will describe their derived method briefly in the following section with a 1D example.
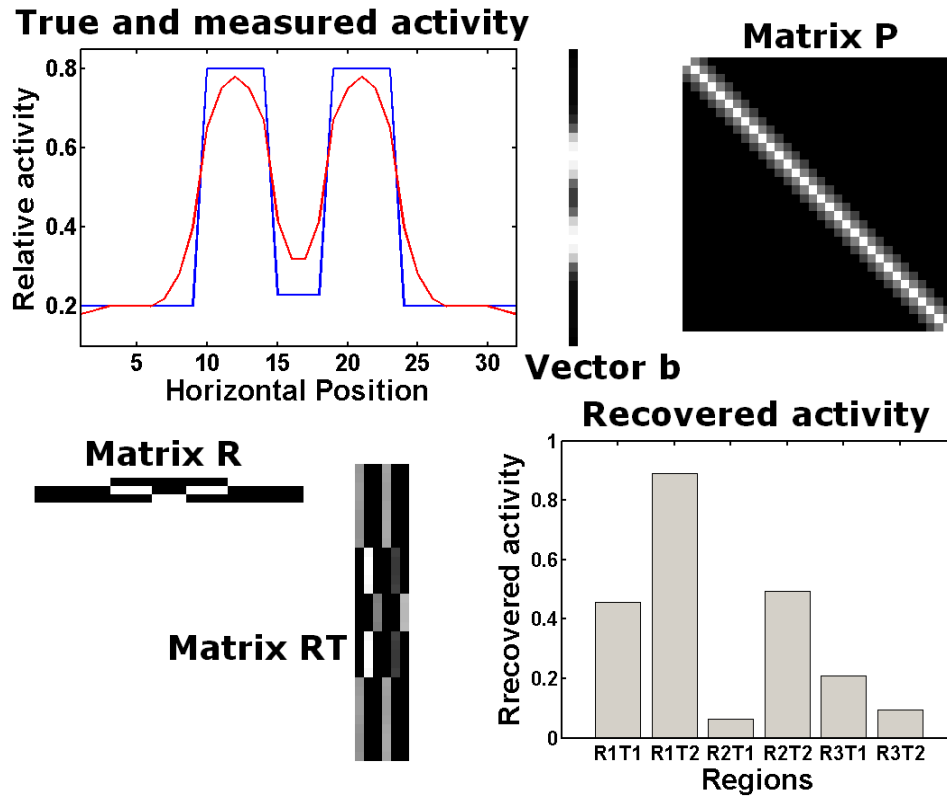
Figure 5.5: A 1D example of statistical PVC method. This example is a modified version of example given by Aston et al. This figure shows different matrices and vectors used in 1D example. A line object is assumed having two hot spots over a background activity concentration.

Suppose our imaged object is comprised of n pixels and let P be a $n \times n$ matrix representing system point spread function (PSF). This matrix will be a symmetric Toeplitz matrix for a space-invariant symmetric system model. Define matrix R as a binary matrix of size $n \times r$ where r is the number of mutually exclusive anatomical regions and T as a $n \times t$ matrix defining different tissue classifications. Let b be a $n \times 1$ vector containing measured tracer concentration in each pixel. The resultant solution vector x will be $rt \times 1$ denoting true activity concentration in different classified regions [42]. If we assume a homogenous activity distribution, the partial volume problem can be formulated as,

$$P(R \otimes T)x = b$$

This relation can be rearranged as follows,

$$(R \otimes T)x = P^{-1}b$$

The last equation represents a linear relation and can be solved using standard linear methods such as conjugate gradient (CG) or weighted least squares (WLSQ) method. Weighted least squares method may be used to find weighted linear least square solution as below,

$$\hat{x} = \left((R \otimes T)^T W (R \otimes T)\right)^{-1} (R \otimes T)^T W P^{-1} b \qquad (5.5)$$

Measurement variance can on the estimated activity values is then given by,

$$var(\hat{x}) = \frac{\left((R \otimes T)^T W (R \otimes T)\right)^{-1} \left((R \otimes T)x - P^{-1}b\right)^T W \left((R \otimes T)x - P^{-1}b\right)}{n - rt} \qquad (5.6)$$

Here, weighting matrix W, is inverse of the covariance matrix. A 1D problem with its solution is shown in Figure 5.5. For experimental purposes, we implemented this method in 2D for our given phantom image and the results have been presented for different priors in the next sections with line intersection length model. We used a point spread function, as a 2D Gaussian distribution with FWHM equal to the FWHM of our blurring function, used to blur the sinogram data. However, we split this PSF into x and y directions into two PSF matrices defining x-direction and y-direction components [42].

5.4.3 Activity Recovery Performance

Figure 5.6, presents results for an implementation of statistical PVC method with QPs and MRPs in MAP reconstruction methods and compares activity recovery performance of these priors with line intersection length model.
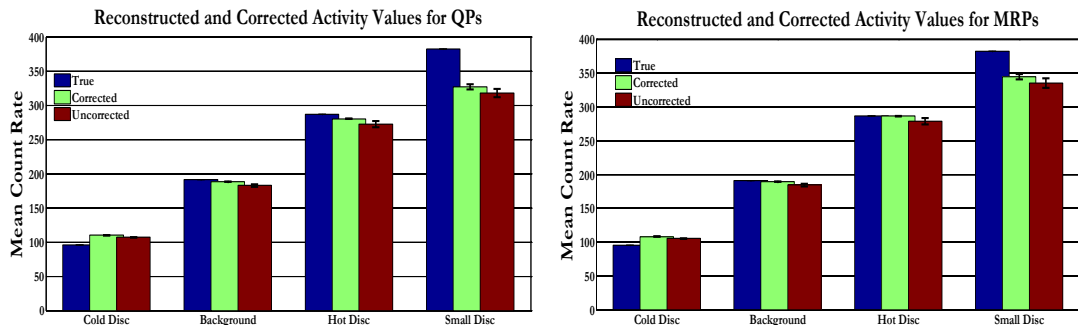
Figure 5.6: Activity recovery performance of QPs and MRPs in Statistical PVC method, with attenuation correction performed, for various disks defined in our digital phantom image. Vertical axis represents mean counts per pixel and error bars indicate variance in each region.

Without attenuation correction, recovered activities are heavily underestimated for all the discs and negative bias values were obtained from -25% to -65%, hence these results are not shown here. These very high bias values mean that activity recovery is heavily undermined, if attenuation correction is not performed.

However, with attenuation correction applied, for QPs, measured values show a spill-out from the hot disc and spill-into the cold disc from the background disc, respectively. An accumulative effect, in the background disc, is a spill-out of the activity from this disc into the cold disc. In smaller hot disc, a heavier spill out can be seen because of higher PVE due to its size comparable to the system FWHM. Similar behavior can be observed in case of ModMRPs, as shown in Figure 5.7, and again in the small hot disc recovery is better as compared to the ModQPs.
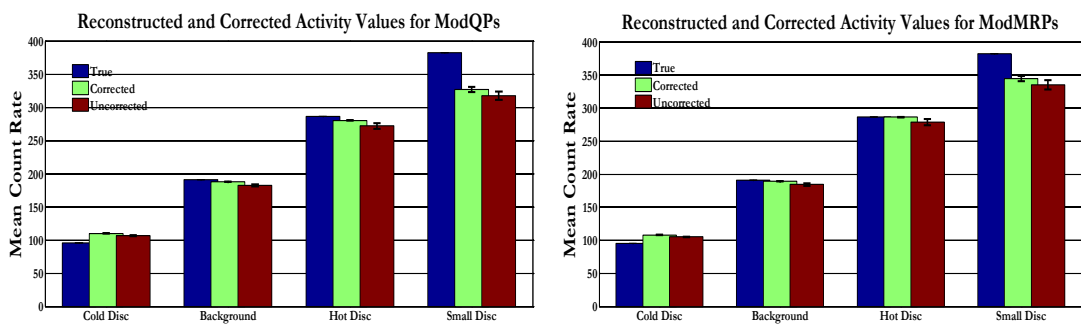
Figure 5.7: Activity recovery performance of ModQPs and ModMRPs in Statistical PVC method, with attenuation correction performed, for various disks defined in our digital phantom image. Vertical axis represents mean counts per pixel and error bars indicate variance in each region.

5.4.4 Bias and Noise Analysis

Figure 5.4, presents results for Percentage Bias obtained using both the priors and with and without attenuation correction applied. Results are highly underestimated without the application of attenuation correction and bias values range from 25% to 70%, in negative, for various priors and beta parameter values.

Hence, it is crucial to include attenuation correction, before any activity quantification is carried out, even with statistical PVC methods. Highest activity underestimation is in the smallest hot disc with a negative bias value of -17% which recovered to -14% after PVC in case of QPs. However, MRPs performed better both in measured values before correction and after PVC applied with -12% to -10% bias values. For other two discs of moderate size, there is a very small underestimation of activity in the measured values with MRPs and it is corrected very well with PVC, however, with QPs there is small amount of error which is certainly corrected, though. For QPs, the image is more smoothed and, hence, results in

more PVE. In both QPs and MRPs, the background disc shows some overestimation, which, after correction gets worse. Similarly, QPs are more sensitive to the parameter value, expectedly.
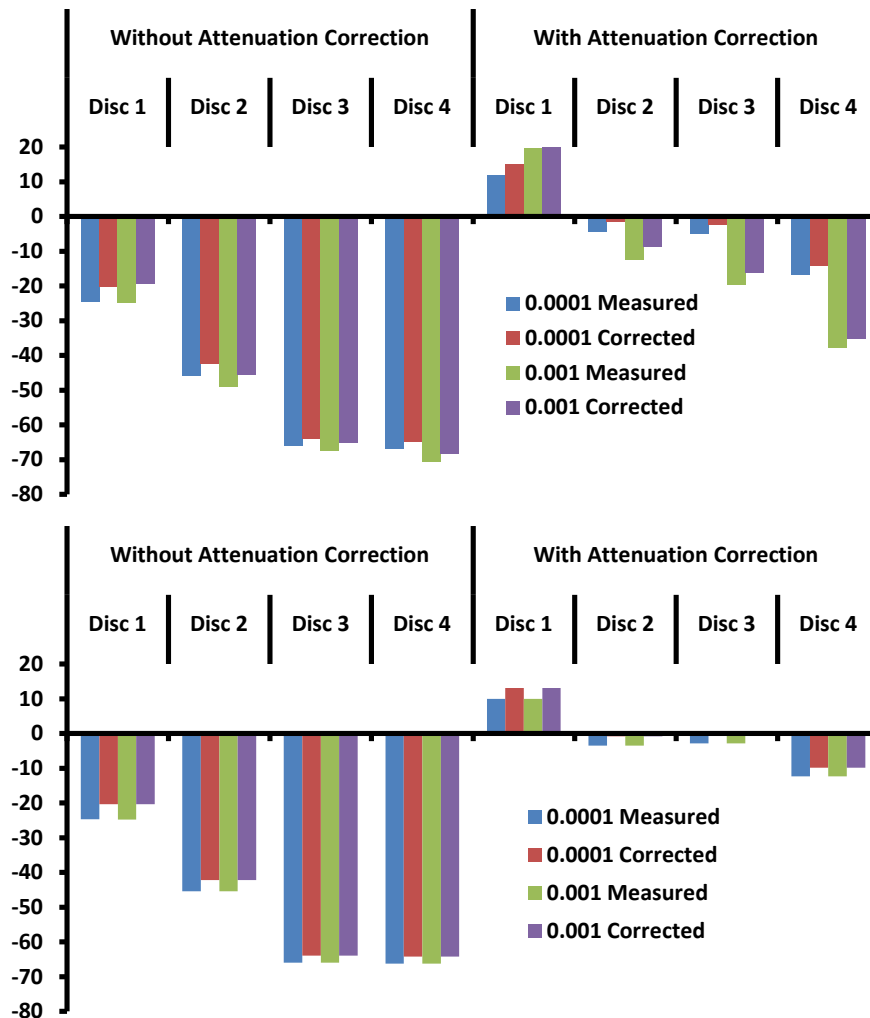
Figure 5.8: Bias (%) performance of QPs (top) and MRPs (bottom) applied in statistical PVC method for various regions defined in our phantom image.

Table 5.3, briefly presents noise performance of QPs and MRPs with GTM method for PVC. Mean recovered values are generated using 30 noisy realizations of the true phantom. Noisy sinograms were generated by adding Poisson noise to the true phantom sinogram and finally the mean recovered regional activities were calculated as average activities of these 30 reconstructions and errors presented are variance of these 30 generated values. Recovered activity values are closer to the true values, for MRPs as compared to QPs, except for the cold disc embedded in a relatively higher activity background disc, where, recovered activity gets worse than the measured one due to the surrounding higher activity.

Table 5.3: Noise performance of QPs and MRPs with Statistical Methods

	True	Corrected	Measured
QPs			
Cold Disc	96	116 ± 11	111 ± 10
Background	191	180 ± 5	172 ± 5
Hot Disc	287	272 ± 13	263 ± 11
Small Disc	382	291 ± 66	279 ± 51
MRPs			
Cold Disc	96	116 ± 12	112 ± 11
Background	191	187 ± 6	180 ± 5
Hot Disc	287	288 ± 15	278 ± 13
Small Disc	382	311 ± 78	300 ± 61

5.4.5 Discussion

In this section, we presented our results for an implementation of various priors in statistical PVC method. These methods have been developed within a mathematical framework to include point spread effect and the tissue fraction effect, while considering statistical nature of the underlying assumptions about noise and data structure. A derivation of the estimation of regional concentrations and associated error estimations are presented in a weighted least squares framework. Similar to GTM, these statistical methods also get complicated with an increase in the number of tissues defined or the size of the image considered, though, not in mathematical complexity but in terms of the computational and storage requirements [37;41;42]. Accuracy of the tissue segmentation and registration process has an ultimate say on the accuracy of the final result and its variation, which is a problem with all other methods using structural definitions of the regions.

This method can accommodate non-stationary system response of the real scanner in the form of a PSF matrix. Though, PSF has a crucial effect on the implementation speed of the method and due to low memory available with PCs a separable model of the PSF has been considered, where this effect was separated in x and y directions. This separable-ability assumption provided an implementation ease and faster speed whereas did not produce much larger error. As mentioned above, non-linearity and space-variance will affect the results, if DRF is included in the system matrix [28;42]. Authors claim that their method does not depend on the assumption of regional activity homogeneity; however, this was not a concern in our assessment of the prior functions performance because we used simulated data for validation with truly defined regions.

Our results indicated that both the QPs and MRPs can recover regional activity values, when used in MAP reconstruction methods and then applied in statistical PVC methods. QPs produce more smooth images and, hence, activity recovery performance of these priors is more sensitive to the beta parameter values as compared to MRPs. Recovered activity concentration is better in case of MRPs, as compared to QPs which could be due to their better comparative edge preserving capability and lower or selective smoothing behavior.

5.5   Summary

Partial volume error is a direct consequence of limited resolution capabilities of the imaging systems. These resolution characteristics are also non-uniform across the spatial span of the system and undermine activity recovery performance of the reconstruction algorithms. MAP algorithms provide us with a way to control resolution properties through the prior term. In this chapter, we used two popular PVC methods to evaluate performance of various priors in MAP algorithm. The simulated phantom, used in the previous chapter, was used for activity recovery performance, of various priors to evaluate effect of spatial activity distribution and its concentration.

Images, reconstructed with QPs and MRPs in MAP algorithm, were evaluated for PVE recovery with GTM method. Our results indicate that these priors have an ability to recover PVE, with GTM method, while it was concluded that attenuation correction has a critical effect on the recovered values and should be performed before the application of GTM method. PVE was mainly due to spill-over from the higher activity regions into the low activity areas with lesser effect due to PSF effect, because of a simple system model used. In larger objects, PVE was mainly due to the edge pixels effect, whereas, in small sized object it was due to spill-over from higher activity concentration regions. This PVE was corrected by MAP estimators including various priors, however, MRPs performed better, or at least, equivalent to QPs in different situations. Similarly, we used statistical PVC methods to recover for PVE using images reconstructed by MAP algorithms, including various priors. These methods take account of the statistical nature of the data and performed reasonably well with the suggested priors. For larger objects PVE is very low and, hence the recovery, whereas for small objects significant error is caused by the PVE and needs careful correction techniques to be applied.

CHAPTER 6

List-Mode Reconstruction Methods

Histogram data is collected in a predefined number of bins in commonly used tomographic imaging systems and then reconstructed using sinogram based reconstruction methods. However, in some systems, such as high resolution research tomograph (HRRT), data is collected as a list of events with different attributes recorded for each event. In such systems, list-mode reconstruction methods are more favorable than the sinogram based reconstruction methods, especially when low count studies are being performed [181]. List-mode data are expected to give better quality images, in low count studies, due to the availability of further redundant data information [155;181;199]. In this chapter, we present an implementation of our proposed priors in MAP algorithms with list-mode data. We contribute towards an assessment of resolution properties of list-mode image reconstruction methods, through an investigation of impulse response function, in MAP methods with our proposed Median Root Based (MRP) priors and have compared our results with standard QPs [184]. We show that better resolution can be recovered with these priors, whereas, QPs produce overly-smoothed images even with list-mode data. We also present results for Combine Priors (CPs), for better user controlled resolution characteristics and noise resolution trade-off with results for non-uniform resolution recovery techniques.

6.1   Introduction

Higher sampling capabilities of modern imaging systems increasingly require a continuous effort to develop new data collection and imaging techniques. For the last few years, total number of crystals in PET tomographic system has increased many folds [176-178;183;184]. There is a proportional increase in the number of lines of response (LORs) for these systems and, hence, requires an exhaustive enhancement in the computational and storage capabilities of these systems. An alternative, to standard histogram reconstruction methods is the use of List-Mode acquisition and reconstruction techniques

to compensate for this increase in the available data [154;181]. Conventional PET systems inherently histogram their acquired data into a predefined number of sinogram bins which is only a feasible method of data collection until the number of lines of response (LORs) does not exceed total number of collected events. This is generally not true when low count studies are performed or not feasible where the number of events in each bin is very close to or less than one. List-mode data collection method is a preferred option in this situation, where collected events are inserted into a long sequential list according to their occurrences in time, along with their other useful information. This data collection method potentially reduces the size of data storage and always has an option of converting latter, if required, the collected data back into the sinogram mode. This always offers a chance to record additional and more accurate information regarding each event, which can be exploited latter during the image reconstruction process. List-mode reconstruction has certain other advantages, too, over histogram reconstruction methods, which includes faster reconstruction and more accurate data information for spatial location and angular position [176].

We present an evaluation of resolution properties of list-mode reconstruction methods, in this chapter, with an emphasis on LIR investigations in MAP reconstruction methods and use of different priors, specially our proposed priors based on median. No such effort has been done before, as of our knowledge, to understand resolution properties of list-mode reconstruction methods using some analytical expression of this kind. We also present a comparison of standard QPs with our proposed MRPs. A further analysis of response symmetry along with resolution properties has been presented using both noiseless and noisy data. These results can help in deeper understanding of the behavior of list-mode reconstruction methods and resolution properties of their reconstructed images which consequently will help making different image processing tasks, such as image comparison, registration or segmentation easier. We used simulated phantom data to do our analysis. This phantom is the same phantom image we used in previous chapters.

6.2 List-Mode Data Simulation

Our digitally simulated phantom image, used in this analysis, has the same shape and activity levels used for non-uniform resolution compensation and partial volume recovery analysis, for consistency of our results. Descriptively, a cold (having lower activity as compared to the background) and a hot disc, of radii 15 pixels, are embedded in an elliptical background disc, with radii 30 and 55 pixels. Activity concentration ratio is same as 1.0, 2.0 and 3.0 in the cold, background and hot disc, respectively. Figure 6.1 presents

this phantom; however, in this chapter we simulated our phantom by generating 1M list-mode events instead of using histogram data simulation scheme [154]. Data simulation algorithm for this phantom may be summarized as follow,

> ➢ Using Matlab's Random Number generator function "rand()", a set of random points inside a rectangle, centered at origin (0, 0), were simulated, tightly inscribing the bigger ellipse of our phantom, having the same radii of size 30 and 55 pixels. Further, points outside of the ellipse and inside the small discs of radii 15 pixels were eliminated by rejection technique. Average activity concentration per pixel in this case was assumed to be 1.0.

> ➢ Again, we generated random points inside two squares inscribing the two small circles (Discs) and rejected those points lying outside of these circles by rejection technique. The number of simulated events was selected such that the relative activity concentration per pixel in left circle (Cold Disk) was half of the background ellipse and double in the right hand circle (Hot Disk) as compared to the background disc.
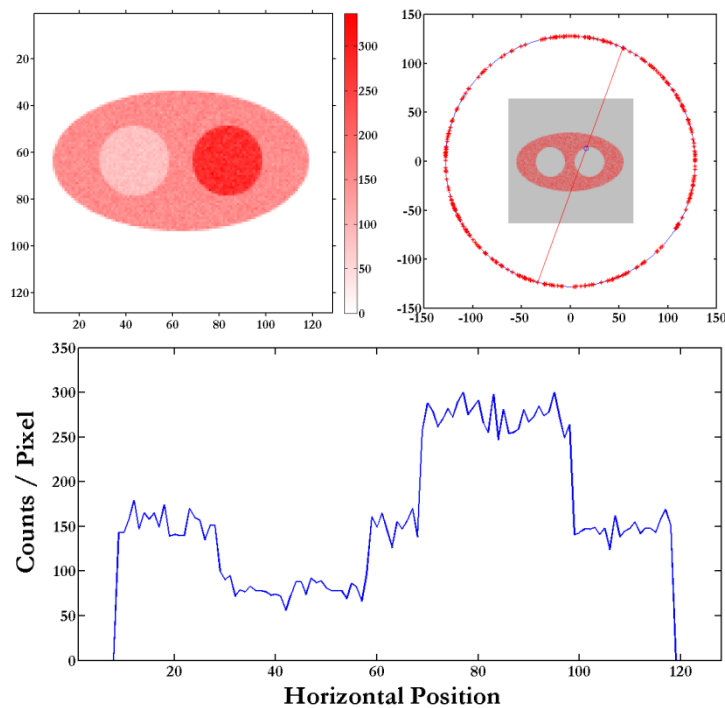
Figure 6.1: A list-mode phantom image (top right) generated by 1,000,000 simulated events with two small discs having activity concentration ratio of 0.5:2 inside an elliptical shaped background disc with a relative activity concentration of 1.0. Image on the top left depicts simulation of a random event with its detection coordinates as line along with many other locations represented by asterisks. The bottom image shows a horizontal profile through the phantom at the centre.

> ➤ These two random point sets were merged to the points of the bigger ellipse to describe emission locations inside our simulated phantom and then normalized to 1M counts. This simulated digital phantom image is shown in Figure 6.1.

> ➤ To simulate random events, along with their emission locations simulated above, inside the assumed detector ring of radius 150 pixels, we generated normally distributed random angles, from $-\pi/2\ to\ \pi/2$, and assigned a random angle from this list to each emission point in our data list. Based on these emission points and random angles, two points (x_1, y_1) and (x_2, y_2) were calculated as opposing detection locations, on the bigger circle, simulating our detector ring, using simple geometry. A typical simulated event is shown in Figure 6.1 with a line representing the LOR and a small circle indicating its emission point inside the phantom.

A file containing long list of event attributes, including two detection points, in form of their spatial coordinates, and an assigned angle was an output of the simulation algorithm. For histogram data representation, we divided the whole data of 1M counts into 16,384 LORs (i.e., 128 bins per view by 128 views over 180°) and detection probability of each event was calculated with respect to its own LOR in which it falls. A part of the list containing few events and their attributes is shown in Figure 6.2.

Figure 6.2: List mode data simulation and data list. First row indicates the total number of events and from the second line onward each column in every row gives attributes of that event.

Few other researchers have used histogram mode data, converted into a list of events, for list-mode reconstruction; however, we more strictly simulated our data in list-mode

manner by generating a list of events with their attributes, though, for a very simple 2D elliptical phantom and circular PET system model [154;181]. It should be noted that reason to use simulated data was an almost no access to the list-mode data from a real scanner. Also, it was much easier to manipulate simulated list-mode data as compared to the real data for our comparative analysis.

6.3   List-Mode Reconstruction Methods

In analytical reconstruction methods, BPF (Back Projection Filtering) is the most suitable algorithm for list-mode data reconstruction [154;176;200]. List-mode events can be back projected and the final image may be post-filtered. These methods are being used even before the list-mode acquisition became popular. However, being an analytical reconstruction method, it uses Fourier Transform and needs complete data to operate upon, which may not be available in 3D acquisitions [78;151;191]. There are few exceptions, where certain solutions have been proposed to generate this data, for example by forward projecting the initially reconstructed image [191]. List-mode data seems to be more appropriately handled by statistical reconstruction methods, due to its count based nature and for exploitation of full list of benefits assumed to be provided by this type of measurements.

If, our object is subdivided into N number of pixels $\{f_j | j = 1, .., N\}$ containing f_j number of expected events, from $j - th$ pixel, which are to be estimated from M number of total recorded events with their attributes given, then List-Mode Likelihood Expectation Maximization (LM-EM) reconstruction method can be expressed mathematically as follows [177;199],

$$x_j^{k+1} = \frac{x_j^k}{s_j} \sum_{\substack{i=1 \\ all\ lors}}^{i=M} \frac{p_{i_l j} \cdot \mathbf{1}}{\sum_{j'=1}^{N} p_{i_l j'} x_{j'}^k}$$

$$s_j = \sum_{i=1} p_{ij}.$$

(6.1)

Here, x_j^k is the $j - th$ pixel update at the $k - th$ iteration, $p_{i_l j}$ defines detection probability of an event emitted at $j - th$ pixel and detected along the $l - th$ LOR, along which that event is expected to be detected, and $\mathbf{1}$ is a unit row vector of size $N\ x\ 1$. A dummy variable j' is used to evaluate forward projection for N pixels and s_j is a row vector defining sensitivity image, for the $j - th$ pixel, which sums the probabilities over all the LORs, also including those one with no counts detected. Though, various derivations have

been proposed for List-Mode MAP-EM reconstruction methods, here we simply adopt an approximate form resembling to that of the OSL-algorithm proposed by Green (1996), as follows [105],

$$x_j^{k+1} = \frac{x_j^k}{\left(s_j + \beta \frac{\partial V(x^k)}{\partial x_j}\Big|_{x=x^k}\right)} \sum_{i=1}^{i=N} \frac{p_{i_l j} \cdot \mathbf{1}}{\sum_{j'=1}^{N} p_{i_l j'} x_j^k} \tag{6.2}$$

This relation is same as the relation (6.1) with an inclusion of the term $\frac{\partial V(x^k)}{\partial x}\Big|_{x=x^k}$ which defines first order derivative of the current image update x^k at $k-th$ iteration, and evaluated w.r.t x_j. Several methods have been proposed to produce images with edge-preserving priors, however, either they are based on high level segmentation techniques [117;134;201] or by inclusion of some additional-functional [110;117;135]. In this work, we propose the use of MRPs in List-Mode MAP reconstruction algorithm, to perform robust and automatic edge preservation. There are several possible ways to take account of any image degrading effects in list-mode image reconstruction methods. However, system matrix factorization is very popular and suitable method to include these effects into the system modeling [23]. We may decompose system matrix P, into $P = WG$, where G represents system geometric model, and W could be a diagonal matrix, having terms w_{ij}, including variations due to attenuation and normalization etc. With this factorization, the reconstruction algorithm will become [154],

$$x_j^{k+1} = \frac{x_j^k}{\sum_{i=1}^{lors} w_{ii} p_{ij}} \sum_{i=1}^{i=M} \frac{p_{i_l j} \cdot \mathbf{1}}{\sum_{j'=1}^{N} p_{i_l j'} x_j^k} \tag{6.3}$$

Here, w_{ii} is a diagonal matrix and may contain attenuation or normalization correction terms on its diagonal. It may also include other effects such as crystal penetration effects; however, that would reduce its sparseness a lot and will burden the computational resources.

6.4   List-Mode Impulse Response Function

In previous chapters, we discussed LIR expression to evaluate local resolution properties of histogram data acquisition mode. Though, in case of list-mode data, this expression may be evaluated from abio-initio as in [178], our experience with the following expression, given in equation (6.4), has shown its approximate validity for list-mode data.

Another reason, to use the same function, is to have better experience of its implementation and to reuse our developed code for implementation and analysis.

$$l^j = \left[H^t diag \left\{ \frac{c_{i_l}^2}{y_{i_l}} \right\} H + \beta \ddot{R}(f) \right]^{-1} H^t diag \left\{ \frac{c_{i_l}^2}{y_{i_l}} \right\} H e^j \tag{6.4}$$

We used this expression, in previous chapters, for histogram data and there are few points to be considered for its implementation with the list-mode data. At first we have to decide for correct formulation of the variance term $diag \left\{ \frac{c_{i_l}^2}{y_{i_l}} \right\} |_{i=1,\dots,M \text{ and } l=1,\dots,LORs}$ in list-mode case, where c_{i_l}'s are the attenuation correction terms for the $l-th$ LOR along which the $i-th$ event occurred and, similarly, y_{i_l} are the measurements in the sinogram space converted from the event list by approximating measurement mean along $l-th$ LOR and for $i-th$ event. If no attenuation correction is applied and data are such that value of $y_{i_l} \cong 1$ or we use a large number of LORs so that in each LOR we have approximately one event collected, then the variance term may be ignored, the response function would simply be expected to behave almost stationary and a major cause of the non-uniformity would vanish. However, in case of our data, we need to include variance term along the LOR, because our data have events along each LOR much larger than 1. The form of our implemented Impulse Response Function is,

$$l^j = \left[H^t diag \left\{ \frac{1}{y_i} \right\} H + \beta \ddot{R}(f) \right]^{-1} H^t diag \left\{ \frac{1}{y_i} \right\} H e^j \tag{6.5}$$

Secondly, heart of the expression, is the term $H^t diag \left\{ \frac{1}{y_i} \right\} H$, which needs to be evaluated event by event for list-mode data and not by LOR, as in sinogram data. However, this form of the term also suggests that, if we convert list-mode data into sinogram, the same algorithm which was applied to histogram mode can also be used to evaluate this expression. Hessian of the prior term $\ddot{R}(f)$ can be obtained by choosing a specific prior distribution. We used both QPs and MRPs in our analysis of the impulse response function for list mode data.

6.5 Impulse Response Evaluation

In the following sections, we present our results for an implementation of LIR with different priors in LM-MAP reconstruction methods. Impulse response function given in

equation (6.5) is a linear system of equations; hence, we opted for second choice mentioned above and used Conjugate Gradient (CG) method to obtain impulse responses.

6.5.1 Implementation of QPs and MRPs

Impulses at three specified points have been shown with induced resolution in FWHM in pixels in Figure 6.3, which displays impulse responses for QPs. In cold disc, resolution is better as compared to the resolution in the hot disc where it is poor. Higher activity has an over smoothing effect which broadens the impulses in the higher count region. Also, obtained values are non-uniform at the three locations, which mean non-uniform reconstructed resolution. Spatial activity distribution has produced this effect, through, an anisotropic smoothing.
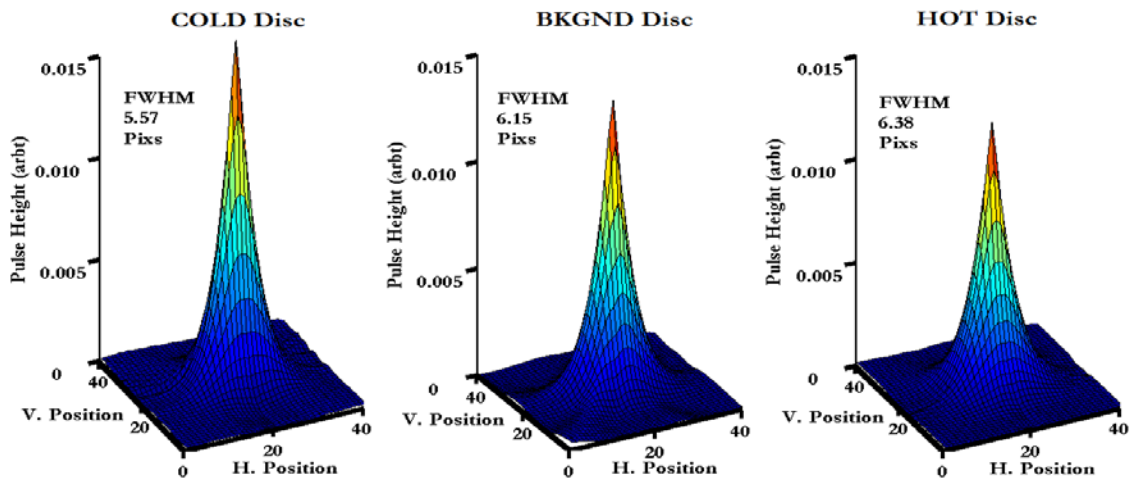
Figure 6.3: This image shows results of an implementation of LIR with QPs at the three specified points inside our phantom. The impulses show that with QPs, reconstructed resolution is non-uniform at the three points which presents space-variance and effect of activity variation.

Similarly, Figure 6.4 shows results for MRPs for the same β value of 0.01 as for QPs and responses are thinner as compared to QPs. Non-linear response in case of QPs at the three locations has also been corrected as the responses are almost similar in height. Reconstructed resolution is still non-uniform, however, non-uniformity is lesser as compared to QPs and heavier smoothing in the high count region has also been recovered with reconstructed resolution getting better.

These results confirm that the recovered resolution or reconstructed resolution has almost same trend in list-mode data reconstruction algorithms, as it has in case of histogram mode, however, with an improvement in its non-uniform distribution. Induced

resolution is better with MRPs as compared to QPs and the responses are thinner which indicate lesser variation with MRPs and supports our hypothesis.
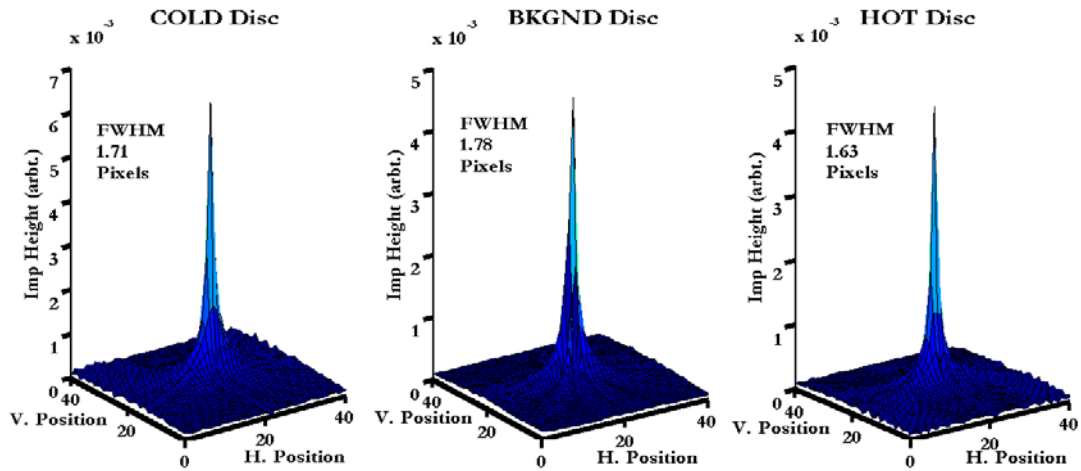
Figure 6.4: This image shows results of an implementation of LIR with MRPs at the three specified points inside our phantom. The impulses show that with MRPs, reconstructed resolution is non-uniform at the three points however non-uniformity is much lesser as compared to the QPs, especially at the high activity point where the QPs have their worse behavior.

6.5.2 Modified Quadratic Priors (ModQPs)

Modified priors have been presented in Chapter 4 for the recovery of non-uniform resolution. These priors were based on certainty method, where local smoothing is controlled by weighting the response according to the local certainty. In histogram mode, a weighting factor is calculated by normalized forward projection of the local measurement certainty. In list-mode data, we use histogramed data in form of a sinogram to evaluate that correction term. Impulse responses evaluated using ModQPs are shown in Figure 6.5.

This figure indicates that non-linear response, due to anisotropic smoothing produced by QPs, has been recovered with ModQPs. We found that the response is sensitive to the parameter value and it is very difficult to optimize hyper-parameter in case of ModQPs. We needed to select a very low value of 1.0×10^{-4} for reasonably reconstructed resolution values, because smoothing behavior was much sensitive to this value and responses got spread much faster with a small increase in the parameter value. This is certainly due to the addition of the correction term to the prior term in the LIR expression. It should be noted that with very large number of LORs, it is not straight forward to include this correction term to the response because in that case the measurement term may become unity or less than unity.
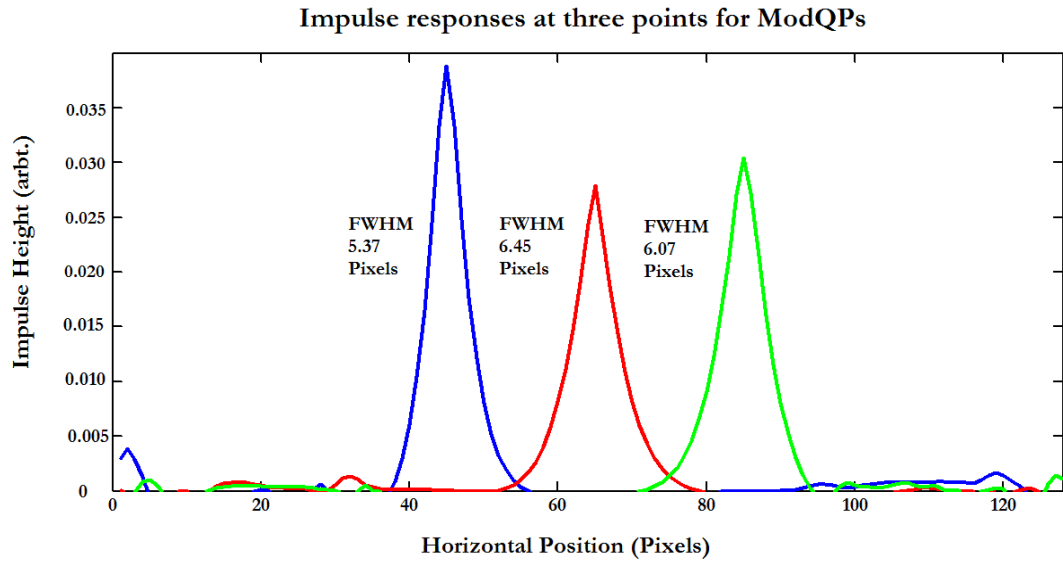
Figure 6.5: Impulse responses at three locations for ModQPs with a parameter value of 1.0×10^{-4}.

6.5.3 Combined Priors (CPs)

QPs and MRPs have different response in recovering the induced or reconstructed resolution. This suggests an idea to use a combination of these priors. As given by equation (4.7), both of the priors may be added together using two different β values to adjust their weight accordingly to the LIR function. Another possible way is to make one parameter value dependent on the other and use only a single value to control both. However, tuning of these parameter values will be a problem and it is better to use only a single value with both the priors. A combined prior gives us a chance to use properties of both the priors, such as smoothing behavior of QPs and edge preserving characteristics of MRPs, at the same time. Figure 6.6 presents our results for an implementation of CPs in LIR expression with a parameter value of 0.01. This figure presents a horizontal profile through an accumulative image obtained by adding the three response images.

This figure indicates that resolution is non-uniform and heavier smoothing is evident in high count region. However, the reconstructed resolution is better as compared to the QPs alone. Some non-linearity, edge effect and anisotropic smoothing are present which may be due to the median operation of MRPs. This may extend up to better resolution control of the resolution properties using MRPs with QPs.

Impulse responses at three locations for CPs
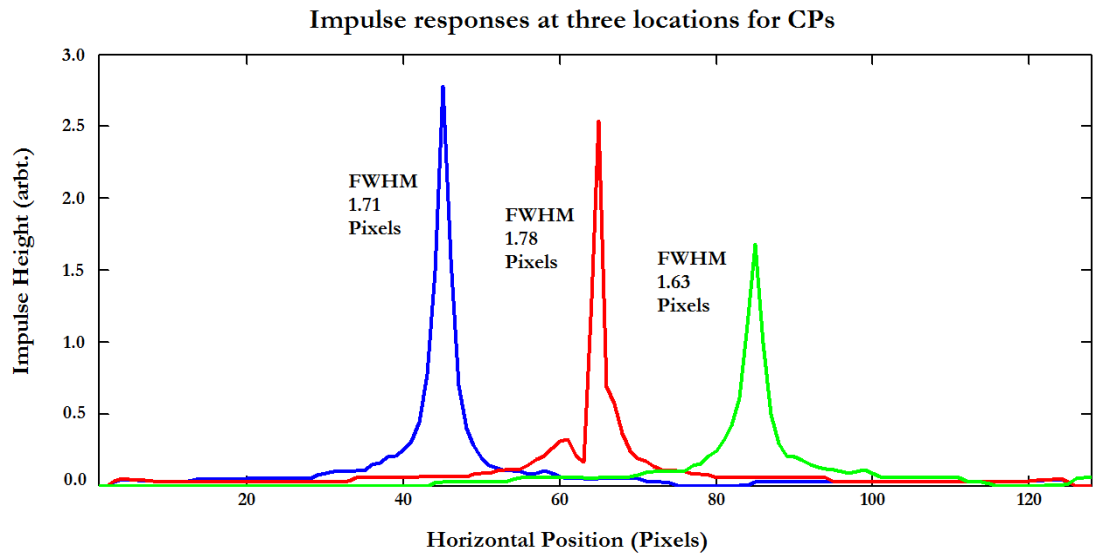
Figure 6.6: Impulse responses at three specified locations with resolution given in FWHM in pixels for CPs using single parameter value.

6.6   Impulse Response Symmetry

We analyzed contour maps for each evaluated impulse using Matlab contour function (countour()) to assess symmetry of the smoothness produced by various priors in the response function. Three contours, evaluated at 99%, 75%, and 50% of the peak value inside each impulse response, were drawn. These contour maps show that the responses are almost symmetric, though this symmetry is slightly better for median priors as compared to the quadratic priors.

Symmetry contours are much broadened out for QPs as compared to MRPs and CPs. This signifies the effect of heavier smoothing in case of QPs, which reduces a lot with MRPs and CPs. For MRPs, smoothness works as a subset of mono-tonicity and broadening of the response mainly depends on the size of the median window and not on the prior function, hence, these contour maps are not so broad. For CPs, it seems to be due the combined effect of median and quadratic operation of both the priors, which reduced the final smoothing effect. Vertical and horizontal broadening is also reduced with the last two priors as compared to the QPs which marks a better symmetry obtained. MRPs induce the least broadening effect in the response as compared to the QPs against the removal of undesirable noise hence the above mentioned results are expected. Another factor which influences smoothness is the empirical parameter and, luckily, MRPs are not that sensitive by the value of this parameter as compared to the QPs.
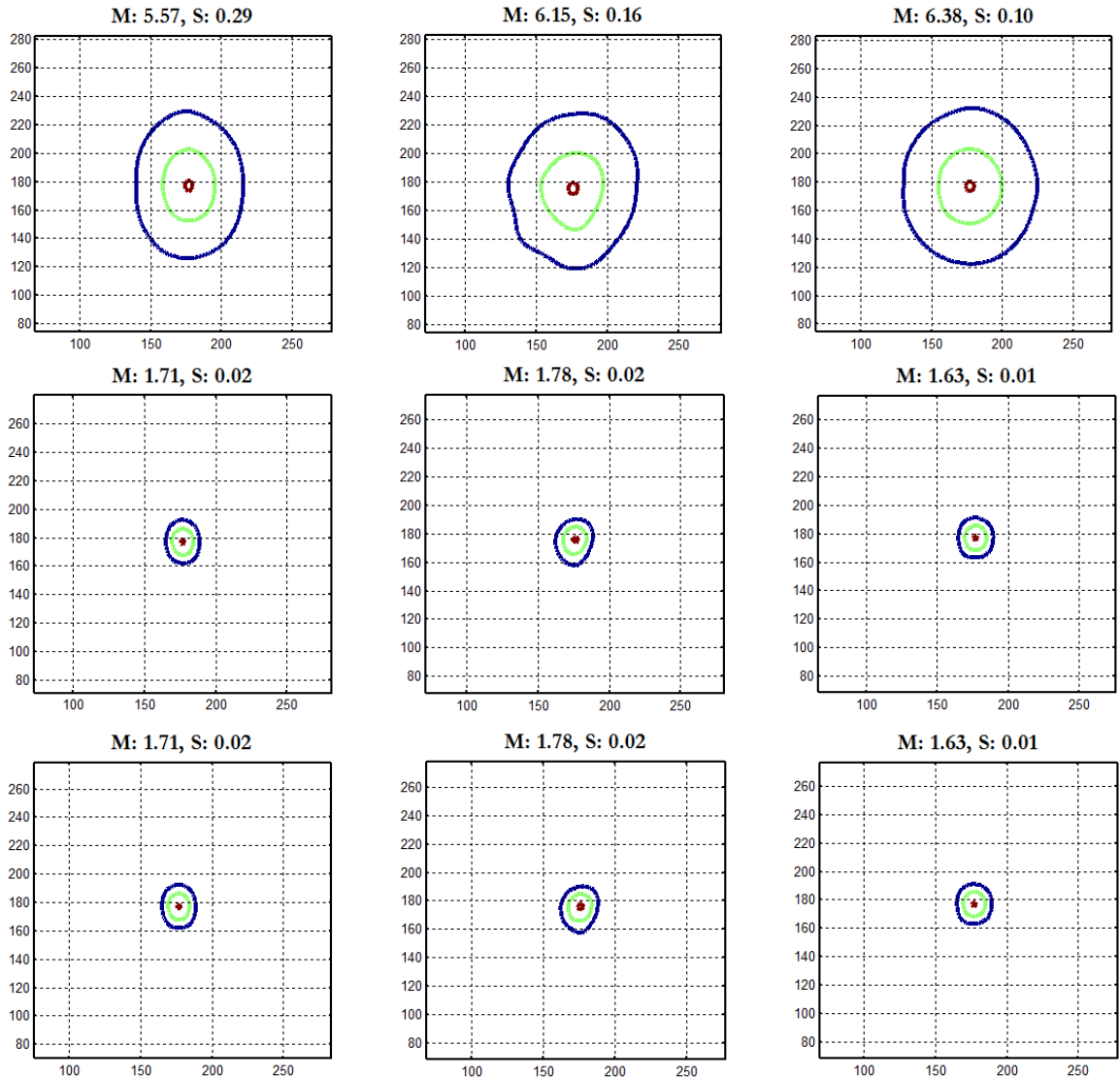
Figure 6.7: Contour maps at the location of the impulses (from left to right: Cold disc, Background disc and Hot disc) to present symmetry and smoothing in case of different priors. Values at the top of the image show mean reconstructed resolution and variance of the contour radius around 360°. It should be noted that the axis values are not the true values but interpolated values in order to present the contours smoothly.

6.7   Noise Performance

Figure 6.8, elaborates results for noisy data reconstructed by list mode MAP reconstruction algorithm including various priors. Noisy list mode data were generated using normally distributed random numbers (by srand() function of c++ with timer object to seed it) to create a list of 500,000 events and 30 different realizations were obtained. These noisy lists were reconstructed using QPs, MRPs and CPs in MAP estimators for list-mode reconstruction and their mean and variance images are shown in the figure below.
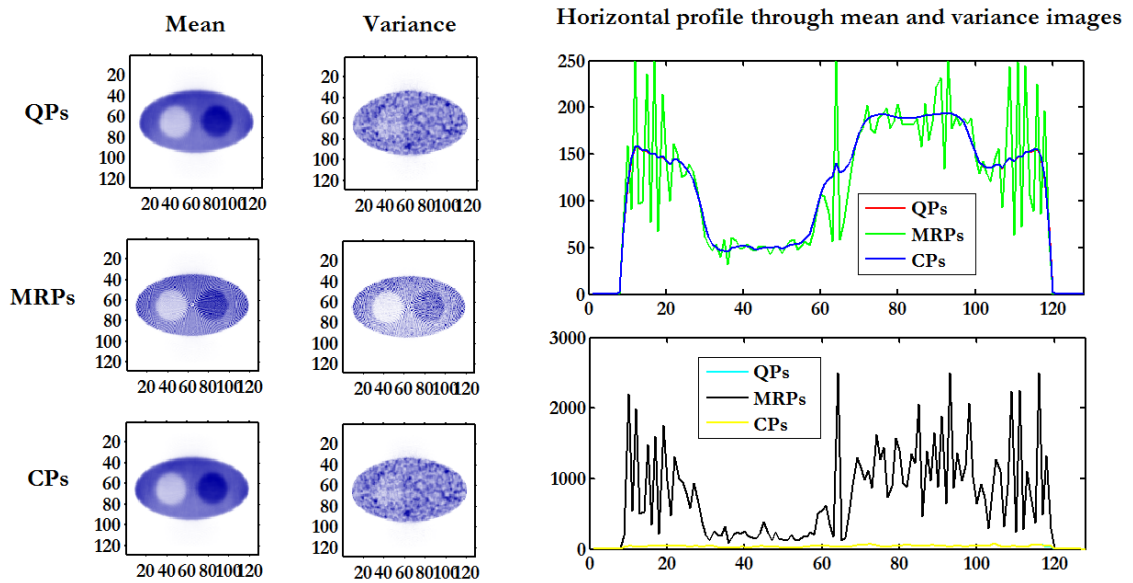
Figure 6.8: Mean and Variance images and horizontal profiles through them for different prior functions for 30 different noisy realizations of list mode event lists. Images were reconstructed using QPs, MRPs and CPs with a parameter value of 1.0 x 10^{-3}.

Mean images show a strong smoothing effect of QPs and CPs while images are not so heavily smoothed out by MRPs, which is clearly an indication of low smoothing behavior. However, mean and variance profiles through MRPs are highly noisy and speak out for nonlinear behavior of MRPs, which seems to be stronger in case of list-mode data as compared to the histogram data due to noisy nature of list-mode data. Hence, CPs may be helpful in this situation to adjust blurring (QPs) and sharpness (MRPs) in list mode data reconstruction.

6.8   Summary

We discussed resolution characteristics of list-mode reconstruction methods in this chapter, by analyzing LIR functions at various spatial locations inside the FOV, with MAP estimators to compare various priors. Standard QPs and MRPs produce images with non-uniform resolution characteristics, however, this variation in resolution is a consequence of various image degrading effects and, is not as strong as in case of histogram reconstruction methods. The recovered resolution depends on the activity concentration and its spatial distribution across the spatial span of a particular image region. Modified priors based on MRPs, produce images with better recovered resolution, whereas, combined priors produce images with resolution properties in between of QPs and MRPs as summarized in Figure 6.11. Modified quadratic and median priors are much less sensitive to the hyper-parameter value, which is similar to the results in the previous chapter. We only analyzed

results for those parameter values, where quadratic and median priors have almost matched resolution at the centre of the image.

CHAPTER 7

Conclusions and Future Work

7.1   Conclusions

Tomographic imaging systems provide us with an ability to quantify distribution of object properties in-vitro, however, their output response depends on accurate modeling of the physics of emission and detection processes, geometry of the system and reconstruction algorithm used. Reconstructed image resolution and noise in the resultant image define its quality and ability to quantify its various properties. Accurate modeling is required to optimize system resolution capabilities; however, due to spatially non-uniform image degrading effects reconstructed resolution is spatially non-uniform across the field of view. Even with accurate data modeling to optimize resolution, tomographic image reconstruction problem is an ill-posed problem in its mathematical formulation [6;11;14;23;28;31;52;76;195]. There is always a compromise between resolution and noise, hence acquisition and detection models only cannot provide an optimized result. Modeling of the object properties and noise processes is required to achieve a best bias variance trade off. Analytical reconstruction methods, such as FBP, have limited ability to model imaging physics because they follow line integral model [78;151;191]. Iterative reconstruction methods can easily model imaging physics and object properties and lead to images with better resolution and noise characteristics [17;118;120]. Iterative methods, such as MLEM, model acquisition and detection processes and lead to overly noisy images, with increasing iteration number, because of ill-conditioning of the problem due to noise and incomplete data. Statistical iterative reconstruction methods, for example MAP methods, can include model of the object properties to better condition the problem and to reduce the reconstruction based noise. These object models are generally formed as prior distribution functions and are applied as constraints on the final solution image explicitly [29;50;66;111;117;148].

Two types of prior distribution functions, namely smoothing priors and edge preserving priors, are commonly applied for computational simplicity and to capture local

empirical image properties. Smoothing priors, such as QPs, attract the final image towards it locally smoother version, which reduces noise, however, over smoothes high count regions, such as edges at the same time and produce shape distortions. They bear anisotropic smoothing behavior due to implicit non-uniform data weightings, non-uniform object activity levels, object size and image estimator characteristics etc., and result in highly asymmetric responses [26;29;129;138]. Imaging system's response, for MAP or PLEM estimators, depends on the Hessian of the prior function and, luckily for simple QPs, it becomes independent of the object and is not prone to abrupt activity changes inside the object. Absence of a universal method to tune the regularization parameter is an added complexity and response of the system with smoothing priors is highly sensitive to the value of this parameter [129;168;190]. Alternatively, edge preserving priors can be used, where edge preservation can be enhanced with non-quadratic prior functions. These priors use an additional empirical parameter to change behavior of the prior near the edges. Unfortunately, non-quadratic priors make the objective function non-convex, add data dependency and increase ill-conditioning of the problem. Similarly, empirical definition of edge height introduces a bias and reconstructed resolution is non-uniform and asymmetric across the FOV, because of spatially non-uniform physical and detector based effects [135].

Another class of edge preserving priors, based on MRPs and TV priors, works on local mono-tonicity or image regularity based image descriptions, including smoothness as a subset. These priors have a theoretical pitfall that their derivatives are not defined analytically. However, heuristics definitions are available for their derivatives and work well for reconstruction purposes. MRPs based priors use median in a local neighborhood to penalize pixel values and drag the final image towards its locally mono-tonic version. Median follows the edge so edge preservation becomes robust. Unfortunately, these priors too, increase ill-conditioning of the problem and response function becomes dependent on the object values through the median or TV operations. Hence, estimators based on these priors take longer to converge as compared to the smoothing priors [108;110;112;114;116;117;134;135;149;150;201].

We observed that reconstructed resolution depends lesser on the hyper-parameter values and more on the size of the median filter window, in case of MRPs as locally monotonic changes smaller than the root images pass through the filter unaltered. However, if more weight is given to both of these priors, i.e. MRPs and TV priors, patchy edge artifacts dominate the resultant images, which is severe in case of TV priors. This seems to be due to monotonic and regularity behavior of MRPs and TV priors. MRPs have several advantages over QPs and other non-quadratic priors, such as automatic edge preservation, reconstruction of the smooth regions at the same time, reduction of noise,

and requirement of only one parameter and lesser sensitivity to the parameter value. Based on these observations, we proposed several MRPs based prior functions, in this work, for the purpose of image reconstruction from simulated and real scanner data and have shown their ability to recover non-uniform resolution and PVE and have compared them with QPs and TV priors [107;110;139].

Our initial reconstruction results, with thorax chest phantom using different algorithms, show that MRPs have more matching noise performance to MLEM algorithm in terms of MAE, percentage bias and Variance as compared to the other algorithms. QPs have lesser MSE values, which is due to higher smoothing effect of these priors. Reconstructed resolution properties were studied in terms of uniformity, linearity, symmetry and parameter sensitivity and our results show that MRPs performed better than QPs. This is because MRPs produce images by penalizing pixel values with least blurring induced. Implementation of QPs and MRPs in LIR expression indicates that resolution is more uniform, linear and has more symmetric responses for MRPs. The recovered resolution is better in case of MRPs as compared to QPs.

Response (LIR) of MAP estimators with smoothness priors becomes spatially non-uniform, nonlinear and asymmetric. Local certainty based methods for QPs have been proposed to correct for these problems. We proposed an alternate prior based correction with MRPs in place of certainty based correction. Instead of evaluating a correction term based on the local certainty, this method uses nonlinearity of MRPs to work as a local correction factor for the recovery of non-uniform resolution response. Our results reveal that, this method recovers for non-uniformity, nonlinearity and asymmetry of the local response, with additional benefits of edge preservation and lower sensitivity to the hyper-parameter values. Implementation of MRPs, with certainty based correction term, does not show much improvement over the simple MRPs results. However, we proposed a hybrid type of priors, combining both QPs and MRPs, which lead to a better control of the final reconstructed resolution. In CPs, locally smooth version of the final image is attracted by QPs, whereas MRPs try to favor local mono-tonicity, producing an image influenced by both of the priors. Different weights can be assigned to both priors, however, their tuning may be a problem and it is better to use a single parameter value for both. This is theoretically feasible because both the priors work on pixels in the same neighborhood. Implementation of MRPs with real data shows that they produce less smoothness as compared to QPs. Noisy data of the holes phantom, reconstructed with MRPs, depicted lower MAE as compared to QPs and TV priors, for three different count levels. We have also developed analytical expressions, for iteration based noise propagation, for MAP algorithm using MRPs and validated our theoretical expressions using Monte-Carlo method for noisy data. Our results

for mean and variance images indicate that MRPs produce less smoothing and smaller error as compared to QPs and TV priors.

We also used our proposed priors in two very popular PVC methods and compared their activity recovery performance with QPs. Results indicate that there is a spill-over effect from high count regions into lower activity regions surrounding them. Modeling of image degrading effects is critical for the correction of PVE, because, without inclusion of these effects into the model, recovered activities were highly underestimated. MRPs performed better as compared to QPs and are less sensitive to the hyper-parameter values for noisy data, whereas object size strongly affects the results. We assumed a separable PSF for statistical PVC methods, which worked well for MRPs and QPs, however, both GTM and statistical PVC methods get influenced by segmentation and registration errors. For large sized objects, all the priors performed almost similar, whereas, for small sized objects, our proposed MRPs performed better than QPs. Error in the recovered activity concentration increases with increasing size of the object, which indicates higher variance in the recovered values. This could be due to large spatial domain covered by large sized objects and, hence, larger variations in the recovered values.

We used certain assumptions for our experimental design and the most prominent assumption was that pixels are square and pixel size is equal to the size of a single detector or sinogram bin. This assumption is a very simple, however, very general one. We used a very simple system model including only the geometric system and attenuation modeling, whereas, other effects were simply ignored. This is, however, justifiable because our work was mainly a comparison of various priors and inclusion of the effects was certainly going to worsen the results of all the priors almost equally. We have also used a mix of object sizes and activity levels to observe their influence on the final reconstructed resolution and activity recovery performance. An implementation of LIR, including various priors, with list-mode data is presented, in this work, for the first time, as of our knowledge. QPs and MRPs produce images with non-uniform resolution properties, whereas, MRPs are less sensitive to the parameter value. Modified QPs recover nonlinearity in the response and CPs perform well for list-mode data, too, and MRPs have shown lower smoothing behavior with noisy data.

Considering all above, we conclude that MRPs have lower smoothing behavior, better edge preservation and lower sensitivity to the parameter value as compared to the commonly used QPs. In our view, the myth of not using nonlinear and non-quadratic prior functions for the purpose of uniform resolution properties is not correct and we have seen that nonlinear behavior of MRPs can be used as a correction factor. *This work presents that MRPs induce lesser spatial variations in the system response as compared to the standard*

QPs in terms of non-uniformity, nonlinearity and parameter sensitivity. They can also be modified in order to recover, for non-uniform spatial resolution and for better activity recovery performance.

7.2   Future Work

Following may be some further extensions of the work presented in this thesis;

1. We used CG method, an iterative solver, to solve LIR expression and even for a modest size of the image matrix and sinogram, convergence of the expression is very slow. Also, for comprehensive analysis and comparison, one may need to evaluate LIR for each individual pixel. This is very time consuming computational task and development of fast calculation methods, to reduce required computational time to carry out an exhaustive evaluation, will be helpful.

2. Spatially non-uniform resolution is a consequence of various image degrading effects, which need to be modeled accurately to optimize resolution; however, it overburdens system resources. We studied effects of non-uniform attenuation, whereas, inclusion of all other effects for accurate system model can be a further extension of this work.

3. We used constant spatial weighting factors to evaluate our prior functions in a small neighborhood and applied nonlinearity of MRPs to recover for non-uniform resolution. Methods have been proposed to evaluate spatially varying weights, which will ultimately generate a spatially varying prior function and may combat for local changes. A possible further extension could be the derivation of space-variant penalty coefficients to obtain images with almost uniform resolution properties.

4. Inclusion of MRPs in MAP algorithms means to reduce noise with minimum level of smoothing. It needs to be verified that how sensitive are the median priors to very small changes in data that may be due to noise and not the signal itself.

5. Instead of obtaining an arbitrary uniform resolution, we are frequently more interested in some user defined resolution characteristics. A possible extension of this work could be to design penalty coefficients for some user defined resolution response.

6. List-mode data contains redundant information about any particular event which could be useful to recover for PVE. Development of a PVC method for list-mode data can be a possible extension of our work.

7. We carried out a comparison of resolution properties of different priors using 2D data. This work can be extended to 3D reconstruction methods as new scanners and imaging systems work in 3D to take advantage of extra contrast gained.

8. Most of the results presented in this thesis are based on simulated PET data. We proposed several new median based priors to compensate for non-uniform resolution characteristic of MAP or penalized-likelihood tomographic image reconstruction methods. Though, few results with real data have been evaluated, further validation with an exhaustive real data analysis may be an extension of the work.

9. Future analysis can be extended to other modalities such as SPECT, CT or MRI, where, there are some additional problems involved (depth dependent resolution in case of SPECT).

APPENDIX A

This Appendix presents few routines coded to simulate and process the data and analyze various results.

A.1   Calculation of Mean and Variance – Theoretical Formulae

This matlab routine calculates mean image using theoretical formula given by equation (4.12) for QPs and a similar routine can be used for MRPs.

```
clear all

%Load ak
    Load the reconstructed image at 1st iteration as "ak".

%Make matrix R
    Load matrix R as "mat_R" for QPs as given by equation ().

%Load H
    Load system matrix H as mat_h

%Load f
    Load true phantom image as "ph".

%Matrix to filter the image
h = [0 -0.25 0;-0.25 1 -0.25; 0 -0.25 0];

%Log of the image matrix
ak = log(f);

%Calculate "log(ak)" at ith iteration
for i=1:30
    tic
        AA = ak;
        BB = log(mat_h' * ((mat_h*ph)./(mat_h*exp(ak))));
        CC = log(s' + 0.0005 * (mat_R*exp(ak)));
        ak = real(AA + BB - CC);
    toc
end

%Recover image from "log(ak)"
img = reshape(exp(ak), 64, 64);
ph=reshape(ph, 64, 64);
```

The following matlab routine calculates variance using theoretical formula given by equation (4.13) for QPs. We need to change the for-loop only as follows where we need to use sparse matrix functions even for a 64 x 64 image size.

```matlab
for i=1:30
tic
    %% Calculate Variance Image
    AA = sparse(diag(1./s)*mat_h' *diag(1./(mat_h*exp(ak)))*mat_h*diag(exp(ak)));
    BB = sparse(diag(1./s)*mat_h' *diag(1./(mat_h*exp(ak))));
    CC = sparse((0.0005.* mat_R)*diag(1./(s'+0.0005.*mat_R* exp(ak))));
    U = BB +(CC-AA)*U;
    %%End of Variance Image

    % Calculation of Mean Image
    AA = sparse(ak);
    BB = sparse(log(mat_h' * ((mat_h * ph)./ (mat_h * exp(ak)))));
    CC = sparse(log(s' + 0.0005 * (mat_R * exp(ak))));
    ak = sparse(real(AA + BB - CC));
    % End of mean image calculations
toc
end

%Covariance matrix
cov = (exp(ak) .^2) .* (U.^2 * (mat_h * ph));
img = reshape(cov, 64, 64);
```

A.2   Image reconstruction routine

This matlab routine reconstructs an image from sinogram data as input using various MAP algorithms. Sys_ele_v2_new(i, sys) is a sub function to evaluate system matrix elements using line intersection length model, following Siddon's algorithm, for the $i-th$ LOR. This routine is freely available on Mathworks FileExchange webpage under a heading of "PET System Matrix".

```matlab
function [rec_img, rms] = ImageReconstruction(sys, sino, algo, iter, beta, neighb)
% FUNCTION REC_IMG = IMAGERECONSTRUCTION(SINO, ALGO, ITER, BETA)
%
% This function reconstructs and image using line intersection length
% system model and different regularized and unregularized reconstruction
% methods.
%
% sys - is a system structure to define PET system variables
% sino - is the sinogram to be reconstructed
% algo - is the algorithm such as MLEM, PLEMQP, PLEMMP
% iter - is number of iterations to be used
% beta - such as value of beta to be used etc.
% neigh - neighbourhood for MPs a vector [3 3], [5 5], [7 7] or [9 9]
%
% Munir AHMAD
% 06-NOV-2010
%
if length(neighb) ~= 2
    disp('Array neighb should be 2D..');
    return
end

sz = size(sino);

img = zeros(sys.hpixels, sys.vpixels);

sino_vec = reshape(sino, sys.nangles * sys.trays, 1);
solx = ones(sys.hpixels * sys.vpixels, 1);
sj = zeros(sys.hpixels * sys.vpixels, 1);
bq = zeros(sys.hpixels * sys.vpixels, 1);
```

```matlab
switch algo

    case 'MLEM'      % in case of mlem algoithm

        for i=0:sys.nangles * sys.trays - 1
            out = sys_ele_v2_new(int16(i), sys);
            ind = sub2ind(size(img), out(:, 2) + 1, out(:, 1) + 1);
            sj(ind) = sj(ind) + out(:, 3);
        end
        fprintf(1, '\nAlgorithm is MLEM\n');
        fprintf(1, 'Iteration finished is   0');
        for it = 1:iter
            for i=0:(sys.nangles * sys.trays) - 1
                out = sys_ele_v2_new(int16(i), sys);
                ind = sub2ind(size(img), out(:, 2) + 1, out(:, 1) + 1);
                if sj(ind) ~= 0
                    sum1 = sum(solx(ind) .* (out(:, 3) ./ sj(ind)));
                end
                if sum1 ~= 0
                    bq(ind)=bq(ind)+(out(:,3)./sj(ind)).*(sino_vec(i + 1)./sum1);
                end
            end
            solx = solx .* bq;
            bq(:)=0;
            rms(it) = norm(solx) / (sqrt(length(solx)))';   % calculates rms error
            if (it < 10)
                fprintf(1, '\b\b');
            elseif (it < 100)
                fprintf(1, '\b\b\b');
            elseif (it < 1000)
                fprintf(1, '\b\b\b\b');
            end
            fprintf(1, ' %d', it);

        end
        fprintf(1, '\nCalculation finished and reconstructed image returned\n');

    case 'PLEMQP'

        h = [0 -1 0;-1 4 -1; 0 -1 0];

        for i=0:sys.nangles * sys.trays - 1
            out = sys_ele_v2_new(int16(i), sys);
            ind = sub2ind(size(img), out(:, 2) + 1, out(:, 1) + 1);
            sj(ind) = sj(ind) + out(:, 3);
        end
        fprintf(1, '\nAlgorithm is PLEM QPs\n');
        fprintf(1, 'with beta values as %f   \n', beta);
        fprintf(1, 'Iteration finished is   0');
        for it = 1:iter
            for i=0:sys.nangles * sys.trays - 1
                out = sys_ele_v2_new(int16(i), sys);
                ind = sub2ind(size(img), out(:, 2) + 1, out(:, 1) + 1);
                if sj(ind) ~= 0
                    sum1 = sum(solx(ind) .* (out(:, 3) ./ sj(ind)));
                end
                if sum1 ~= 0
                    bq(ind) = bq(ind)+(out(:,3)./sj(ind)).*(sino_vec(i + 1)./sum1);
                end
            end
            solx = solx .* bq;
            solx = reshape(solx, 128, 128);
            h1 = (1 + beta .* imfilter(solx, h, 0, 'corr', 'same') ./ 4);
            solx = solx ./ h1;
            solx = reshape(solx, 16384, 1);
            bq(:)=0;
            rms(it) = norm(solx) / (sqrt(length(solx)))';   % calculates rms error

            if (it < 10)
                fprintf(1, '\b\b');
            elseif (it < 100)
                fprintf(1, '\b\b\b');
            elseif (it < 1000)
                fprintf(1, '\b\b\b\b');
            end
            fprintf(1, ' %d', it);
```

```matlab
            end

            fprintf(1, '\nCalculations finished and reconstructed image returned\n');

    case 'PLEMMP'

            for i=0:sys.nangles * sys.trays - 1
                out = sys_ele_v2_new(int16(i), sys);
                ind = sub2ind(size(img), out(:, 2) + 1, out(:, 1) + 1);
                sj(ind) = sj(ind) + out(:, 3);
            end
            fprintf(1, '\nAlgorithm is PLEM MPs\n');
            fprintf(1, 'with beta values as %f   \n', beta);
            fprintf(1, 'Iteration finished is   0');
            for it = 1:iter
                for i=0:(sys.nangles * sys.trays) - 1
                    out = sys_ele_v2_new(int16(i), sys);
                    ind = sub2ind(size(img), out(:, 2) + 1, out(:, 1) + 1);
                    if sj(ind) ~= 0
                        sum1 = sum(solx(ind) .* (out(:, 3) ./ sj(ind)));
                    end
                    if sum1 ~= 0
                        bq(ind) = bq(ind) + (out(:, 3)./sj(ind)).*(sino_vec(i + 1)./
sum1);
                    end
                end
                solx = solx .* bq;
                z1 = reshape(solx, sys.hpixels, sys.vpixels); z1 = z1';
                z1 = medfilt2(z1, neighb);
                z1 = reshape(z1', sys.hpixels * sys.vpixels, 1);
                z2 = solx - z1; z1(z1==0)=1;
                z1 = z2 ./ z1;
                h = (1 + beta .* z1);
                solx = solx ./ h;
                bq(:) = 0;
                rms(it) = norm(solx) / (sqrt(length(solx)))';   % calculates rms error
                if (it < 10)
                    fprintf(1, '\b\b');
                elseif (it < 100)
                    fprintf(1, '\b\b\b');
                elseif (it < 1000)
                    fprintf(1, '\b\b\b\b');
                end
                fprintf(1, ' %d', it);

                rec_img = reshape(solx, sys.hpixels, sys.vpixels);

            end

            fprintf(1, '\nCalculations finished and reconstructed image returned\n');

    case 'PLEMTV'

            eta = 5.0e-5;

            for i=0:sys.nangles * sys.trays - 1
                out = sys_ele_v2_new(int16(i), sys);
                ind = sub2ind(size(img), out(:, 2) + 1, out(:, 1) + 1);
                sj(ind) = sj(ind) + out(:, 3);
            end
            fprintf(1, '\nAlgorithm is PLEM TV\n');
            fprintf(1, 'with beta values as %f   \n', beta);
            fprintf(1, 'Iteration finished is   0');
            for it = 1:iter
                for i=0:(sys.nangles * sys.trays) - 1
                    out = sys_ele_v2_new(int16(i), sys);
                    ind = sub2ind(size(img), out(:, 2) + 1, out(:, 1) + 1);
                    if sj(ind) ~= 0
                        sum1 = sum(solx(ind) .* (out(:, 3) ./ sj(ind)));
                    end
                    if sum1 ~= 0
                        bq(ind) = bq(ind) + (out(:,3)./sj(ind)).*(sino_vec(i +
1)./sum1);
                    end
                end
                solx = solx .* bq;
```

```matlab
        %Change these lines to implement TV Regularization
        z1 = reshape(solx, sys.hpixels, sys.vpixels); z1 = z1';
        z2 = padarray(z1, [1 1], 'replicate', 'pre');
        z3 = (z1(1:end, 1:end) - z2(1:end-1, 2:end)).^2;
        z4 = (z1(1:end, 1:end) - z2(2:end, 1:end-1)).^2;
        z5 = (2 .* z1(1:end, 1:end)) - z2(1:end-1, 2:end) - z2(2:end, 1:end-1);
        CF = (z5 ./ sqrt(z3 + z4 + eta));
        z1 = reshape(CF', sys.hpixels * sys.vpixels, 1);
        z1 = z1 .* solx;
        h = (1 + beta .* z1);
        solx = solx ./ h;

        bq(:) = 0;
        rms(it) = norm(solx) / (sqrt(length(solx)))';   % calculates rms error
        if (it < 10)
            fprintf(1, '\b\b');
        elseif (it < 100)
            fprintf(1, '\b\b\b');
        elseif (it < 1000)
            fprintf(1, '\b\b\b\b');
        end
        fprintf(1, ' %d', it);

        rec_img = reshape(solx, sys.hpixels, sys.vpixels);

    end

    fprintf(1, '\nCalculations finished and reconstructed image returned\n');

end
```

A.3   Calculation of H^{t}DH for LIR

This C++ routine calculates matrix H^{t}DH embedded in LIR expression to evaluate local impulse response at a given location. Note that this matrix is not sparse and for 128 x 128 image matrix size and 128 x 128 sinogram size huge memory was required, hence, this matrix has been calculated in two different parts which were separately saved in to different files. Also, dynamic memory was used to temporarily hold the variables of huge size. This routine was run on a Dual Core 1800 MHz system having 6 GB of RAM.

```
///////// read COLOUMN MAJOR system matrix file ///////

Load sparse system matrix in coloumn major format using a structure variable

//////// system matrix file read ////////////

////////// Load sinogram file ////////////////////

Load attenuated sinogram file.

////////// end of sinogram reading ///////////

////////// Load sinogram file ////////////////////

Load attenuation factors file

////////// end of sinogram reading ///////////

////////// Calculate AtD part 1 ////////////////////
```

```
ud = new SSysMatUSNew [8384];

for (i=0; i<8384; i++){                    // for all Coloumns of At

        ud[i].nz = 0;

        for (j=0; j<trows; j++){

                sum = 0.0;
                for (k=0; k<sc[i].nz; k++){
                        for (l=0; l<sc[j].nz; l++){
                                if (sc[i].rc[k] == sc[j].rc[l]){
sum = sum + (sc[i].val[k] * (1.0 / __max(sino[sc[j].rc[l]], 10)) * sc[j].val[l]);
                                }
                        }
                }
                if (sum != 0){
                        // write data to matrix dad
                        ud[i].rc[ud[i].nz] = j;
                        ud[i].val[ud[i].nz] = float(sum);
                        ud[i].nz += 1;
                }
        }
        cout << i << "  " << ud[i].nz << "  " << float(sum) << endl;
}
//Decomment to visualize the output
//cout << i << "  " << ud[i].nz << "  " << float(sum) << endl;

}

Save part one of the matrix to the file 1

delete [] ud;  //delete heap memory

}
```

Similar code can be used to calculate part 2 of this matrix and save it into another file.

A.4   Local Impulse Response Evaluation

This C++ routine was used to calculate LIR for MRPs using H^{t}DH in two different parts and uses Conjugate Gradient method for the solution of the linear system.

```
///////// read system matrix file part two ///////
        ud = new SSysMatUSNew [8384]; //Declare memory space
        Load Part one of the matrix HtDH

/// Get Col_b of AtDA matrix or get AtDAej for jth pixel
for (i=0; i<8384; i++){  // for all rows of At
        for (j=0; j<ud[i].nz; j++){
                if (ud[i].rc[j] == col_num){
                                col_b[i] = ud[i].val[j];
                        r[i]     = ud[i].val[j];
                        p[i]     = ud[i].val[j];
                }
        }
}
delete [] ud;          // Delete Part 1 of the matrix in Heap

///////// end of calculate of matrix dad ////

///////// read system matrix file part two ///////
        ud = new SSysMatUSNew [8000];        // Declare memory space
        Load Part one of the matrix HtDH

////////// calculate coloumn of dad ////////////////////
```

```
for (i=0; i<8000; i++){  // for all rows of AtDA
        for (j=0; j<ud1[i].nz; j++){
                if (ud1[i].rc[j] == col_num){
                        col_b[i + 8384] = ud1[i].val[j];
                        r[i + 8384] = ud1[i].val[j];
                        p[i + 8384] = ud1[i].val[j];
                }
        }
}
delete [] ud1;          // Delete Part 2 of the matrix in Heap

////////////// Start of conjugate gradient method ////////////

for (iter=0; iter<200; iter++){   // start of iteration for CG
        //////// Calculate Median Image of the impulse response ///////
        med_array(hpixels, vpixels, sx, medians);

        ///////// read system matrix file part one ///////
        ud = new SSysMatUSNew [8384];
        Load Part one of the matrix HtDH again

        ////////////// Add penalty term for MRP here /////////////////
        for (i=0; i<8384; i++){
                flag1 = 1;
                for (j=0; j<ud[i].nz; j++){
                        if (i==ud[i].rc[j]){
                                flag1 = 0;
                                if (medians[i] != 0){
                                        ud[i].val[j] = ud[i].val[j] + bt /
medians[i];
                                }
                        }
                }
                if ((flag1) & (medians[i]!= 0)){
                        ud[i].nz += 1;
                        ud[i].rc[ud[i].nz] = i;
                        ud[i].val[ud[i].nz] = bt / medians[i];
                }
        }
        ///////////// End of penalty term addition ////////////

        ////////// calculate column from AtDA /////////////////////
        for (i=0; i<8384; i++){  // for all rows of At
                sum = 0;
                        for (j=0; j<ud[i].nz; j++){
                        sum = sum + ud[i].val[j] * p[ud[i].rc[j]];
                }
                q[i] = sum;
                }
        ///////// end of calculate of matrix dad ////

        Similarly calculate q[i] for part 2 of the matrix

        ////// end of q vector calculation ////////////

        sum = 0;
        for (i=0; i<trows; i++){
                sum = sum + r[i] * r[i];
        }
        rho0 = sum;

        /////// Calculation of RHO1 Parameter /////////
        sum = 0;
        for (i=0; i<trows; i++){
                sum = sum + p[i] * q[i];
        }
        if (sum != 0){
                alpha = rho0 / sum;
        }
        else{
                alpha = 0;
        }

        for (i=0; i<trows; i++){
                r[i] = r[i] - alpha * q[i];
        }
```

```
        for (i=0; i<trows; i++){
                sx[i] = sx[i] + alpha * p[i];
        }

        sum = 0;
        for (i=0; i<trows; i++){
                sum = sum + r[i] * r[i];
        }

        //End for loop if error is less than epsilon
        rho1 = sum;
        if (sqrt(rho1) < 1e-8)
                break;

        beta = rho1 / rho0;
        for (i=0; i<trows; i++){
                p[i] = r[i] + beta * p[i];
        }
cout << "End of iteration " << iter << " with error sum (norm_rk) : " <<
sqrt(rho1) << endl << endl;

}  // end of CG
```

This routine writes the evaluated impulse image in a file for further processing. Similar code was used to evaluate impulse response for QPs.

A.5   Simulation of Phantom and Sinogram data

The script given below was used to generate a phantom image having one ellipse and two circular regions with different activity weightings and sizes inside the phantom image. The main phantom image spanned 128 by 128 pixels.

```
%Loop through all pixels and generate weight proportional to activity
for i=1:128
    for j=1:128
        if(((i-cx3)/a3)^2+((j-cy3)/b3)^2) < 1 %If pixel is in the main disk
            if(((i-cx1)/a1)^2+((j-cy1)/b1)^2) < 1 %If pixel is in left disk
                ph(i, j) = 1.0;
            elseif(((i-cx2)/a2)^2+((j-cy2)/b2)^2) < 1 %If pixel is in right disk
                ph(i, j) = 3.0;
            else
                ph(i, j) = 2.0; %If pixel is in back disk
            end
        end
    end
end
```

The following script was used to generate attenuation map image from the same phantom, but having different weighting according to the attenuation coefficients in various image regions.

```
%Loop through all pixels and generate attenuation map image
for i=1:128
    for j=1:128
        if(((i-cx3)/a3)^2+((j-cy3)/b3)^2) < 1 %If pixel is in the main disk
```

```matlab
            if(((i-cx1)/a1)^2+((j-cy1)/b1)^2) < 1 %If pixel is in left disk
                atten_ph(i, j) = 0.003;
            elseif(((i-cx2)/a2)^2+((j-cy2)/b2)^2) < 1 %If pixel is in right disk
                atten_ph(i, j) = 0.013;
            else
                atten_ph(i, j) = 0.0096; %If pixel is in back disk
            end
        end
    end
end

%Call the sinogram making routine
sino_main = make_sino(sys, ph); sino_main(sino_main < 1.0e-10) = 0;

%Attenuated sinogram including activity and attenuation
sino_attenuated = sino_main .* exp(-sino_atten_fact);
```

Following function represents code to generate or simulate sinogram from a structure named "sys" holding system parameters and "img" variable holding the phantom to create sinogram data.

```matlab
function sino = make_sino(sys, img)

    img_vec = reshape(img, size(img,1)*size(img,2), 1);
    j1 = 0; k = 0;
    sj = zeros(sys.trays * sys.nangles, 1);

    for i=0:(sys.trays * sys.nangles ) - 1
        out = sys_ele_v2_new(int16(i), sys);
        ind = sub2ind(size(img), out(:, 2) + 1, out(:, 1) + 1);
        sj(ind) = sj(ind) + out(:, 3);
    end

    % loop to make sinpgram
    for i=0:(sys.trays * sys.nangles ) - 1

      out = sys_ele_v2_new(int16(i), sys); %call routine for one LOR path
      if (out(1, 1) ~= - 1) && (out(1, 2) ~= - 1) && (out(1, 3) ~= - 2)
            ind = sub2ind(size(img), out(:,2)+1, out(:,1)+1);
                % Turn indices of intersected pixels to a vector
            if ((sys.trays / sys.hpixels) == 2)
                ray = mod(i, sys.trays) + 1;
                j = int16((ray) * 0.5 ./ sys.ddet);
                  if j == j1
                sino(k)=sino(k)+sum(img_vec(ind).*(out(:,3)./sj(ind)));
                 else
                    k = k + 1;
                 sino(k) = sum(img_vec(ind) .* (out(:, 3) ./ sj(ind)));
                 end
                 j1 = j;
            elseif ((sys.trays / sys.hpixels) == 1)
                k = k + 1;
                sino(k) = sum(img_vec(ind) .* (out(:, 3) ./ sj(ind)));
                if mod(k, size(img, 1)) == 0
                    sino_ind = [k-size(img,1)+1:1:k];
                    %sino(sino_ind) = smoothts(sino(sino_ind), 'g', 32, 0.7071);
                    %Blurr the sinogram in radial direction
                    sino(sino_ind) =
smoothts(sino(sino_ind),'g',size(img,1),1.4142);
                    %sino(sino_ind) = smoothts(sino(sino_ind), 'g', 128, 2.1213);
                end
            end
        end
    end
    sino = reshape(sino, size(img,1), size(img,2));
end
```

A.6 Partial Volume Correction (GTM)

This code evaluates GTM method using reconstructed image and ROIs defined on the same image. It is assumed that the image variables "im", "roi1", "roi2", "roi3", hold the image and various ROIs images for their reconstructed and true segmented versions.

```matlab
%%% Reshape rec image to vec
im = reshape(im, 1, 16384);

%%%% Reshape measured ROIs ************
true_rois(1, :) = reshape(roi1, 1, 16384);
true_rois(2, :) = reshape(roi2, 1, 16384);
true_rois(3, :) = reshape(roi3, 1, 16384);

%Calculate average counts in rois
avg_counts = sum((true_rois .* repmat(im, 3, 1)), 2)./[nnz(roi1); nnz(roi2);
nnz(roi3)];

%%%% Reshape true ROIs ************
rec_roi1(rec_roi1<1.0e-5) = 0;           % Zero those pixel less than half of the
peak value
rec_roi2(rec_roi2<1.0e-5) = 0;
rec_roi3(rec_roi3<1.0e-5) = 0;
rec_rois(1, :) = reshape(rec_roi1, 1, 16384);
rec_rois(2, :) = reshape(rec_roi2, 1, 16384);
rec_rois(3, :) = reshape(rec_roi3, 1, 16384);

%%%% Calculate wij ************
mat_w(1, 1) = sum(true_rois(1, :) .* rec_rois(1, :)) / nnz(roi1);
mat_w(2, 1) = sum(true_rois(1, :) .* rec_rois(2, :)) / nnz(roi1);
mat_w(3, 1) = sum(true_rois(1, :) .* rec_rois(3, :)) / nnz(roi1);
mat_w(1, 2) = sum(true_rois(2, :) .* rec_rois(1, :)) / nnz(roi2);
mat_w(2, 2) = sum(true_rois(2, :) .* rec_rois(2, :)) / nnz(roi2);
mat_w(3, 2) = sum(true_rois(2, :) .* rec_rois(3, :)) / nnz(roi2);
mat_w(1, 3) = sum(true_rois(3, :) .* rec_rois(1, :)) / nnz(roi3);
mat_w(2, 3) = sum(true_rois(3, :) .* rec_rois(2, :)) / nnz(roi3);
mat_w(3, 3) = sum(true_rois(3, :) .* rec_rois(3, :)) / nnz(roi3);

%%%%%%%Calculate mean measured activity in each region %%%%%
m_A(1)= (sum(true_rois(1, :) .* im)) ./ nnz(roi1);
m_A(2)= (sum(true_rois(2, :) .* im)) ./ nnz(roi2);
m_A(3)= (sum(true_rois(3, :) .* im)) ./ nnz(roi3);

%%%%%%%Calculate variance in each roi %%%%%%%%%%%%%%%%%%%%%
m_V(1)= (var(true_rois(1, :) .* im)) ./ nnz(roi1);
m_V(2)= (var(true_rois(2, :) .* im)) ./ nnz(roi2);
m_V(3)= (var(true_rois(3, :) .* im)) ./ nnz(roi3);

%%%%%%%% EValuate true activity by GTM inversion %%%%%%%%%
t_A = inv(mat_w') * m_A';

%%%%%%%%% Evaluate variance by GTM inversion %%%%%%%%%%
t_V = inv((mat_w').^2) * m_V';
t_V = [[0 0 0 ]', t_V, m_V'];
barvalues(:,:,i) = [t_A'; m_A]';
```

APPENDIX B

[P1]   Ahmad M. and Todd-Pokropek A., "Evaluation of Resolution Properties of Median Priors in List-Mode Reconstruction Methods for PET", *IEEE Nuclear Science Symposium Conference Record*, 2009 [23].

[P2]   Ahmad A. and Todd-Pokropek A., "Comparison of Noise Performance for Penalized-Likelihood Image Reconstruction Methods with Uniform Resolution Estimators", *IEEE Nuclear Science Symposium Conference Record*, Oct. 19-25, 2008.

[P3]   Ahmad M. and Todd-Pokropek A., "Median based Priors for Non-Uniform Resolution Compensation in Tomographic Image Reconstruction", *Modeling and Simulation (MS 2008)*, 26-28 May, Canada 2008.

[P4]   Ahmad M. and Todd-Pokropek A., "Non-uniform resolution compensation in tomographic image reconstruction methods using median based priors", *IEEE Nuclear Science Symposium Conference Record*, Vol. 6, Issue, Oct. 26-Nov. 3, Page(s):4447 – 4451, 2007.

[P5]   Ahmad M. and Todd-Pokropek A., "Non-uniform Resolution Recovery Using Median Priors in Tomographic Image Reconstruction Methods", *Lecture Notes in Computer Science (LNCS)*, Volume 4673/2007, Pages 270-277, August 2007.

[P6]   Ahmad M. and Todd-Pokropek A., "Partial Volume Correction using Median Priors in Penalized-Likelihood Image Reconstruction Methods", *IEEE Nuclear Science Symposium Conference Record,* Vol. 4, Issue Oct. 29 -Nov. 1, Page(s):2099 – 2102, 2006.

[P7]   Ahmad M. and Todd Pokropek A., "Partial Volume Correction, using median priors in penalized-likelihood image reconstruction methods", presented at *Imaging 2006 conference*, Stockholm, Sweden, 27-30 June 2006

[P8]   Ahmad M. and Todd Pokropek A., "Impulse response investigations of median and quadratic priors in penalized-likelihood image reconstruction methods", presented at *(2006) 11th Symposium on Radiation Measurements and Applications (SORMA)*, University of Michigan, Ann Arbor, USA, 23-28 May 2006.

References

(1) Kearfott K. J., Votaw J. R. The Basics of Positron Emission Tomographic (PET) Imaging. In: Emran A., editor. *Chemists Views of Imaging Centers*. 1995 Springer US.

(2) Bendreim B., Townsend D. The theory and Practice of 3D PET. *Springer*; 1998.

(3) Sharir T., Ben-Haim S., Merzon K., Prochorov V., Dickman D., Ben-Haim S., Berman D. S. High-speed myocardial perfusion imaging initial clinical comparison with conventional dual detector anger camera imaging. *JACC Card Img* 2008;1(2):156-63.

(4) Muehllehner G., Karp J. Positron emission tomography. *Phys. Med. Biol* 2006;51(13):R117-R137.

(5) Karuta B., Lecomte R. Effect of detector weighting functions on the point spread function of high-resolution PET tomographs. *IEEE Trans. Med. Img.* 1992;11(3):379-85.

(6) Thielemans K. Scatter estimation and motion correction in PET. IEEE Nucl. Sci. Symp. Med. Img. Conf.; 2005.: p. 1745-7.

(7) Bronnikov A. V. Approximate reconstruction of attenuation map in SPECT imaging. *IEEE Trans. Nucl. Sci.* 1995;42:1483-8.

(8) James S., Phelps M. E. Physics in nuclear medicine. Philadelphia: Saunders; 1987.

(9) Lowry A., Taylor D. N. Improvements in image contrast and quantification using scatter subtraction in SPECT. *Br. J. Radiol* 1986;59:728.

(10) Jaszczak R. J., Greer K. L., Floyd C. E., Harris C. C., Coleman R. E. Improved SPECT quantification using compensation for scattered photons. *J. Nucl. Med.* 1984;25(8):893-900.

(11) Hermansen F., Spinks T. J., Camici P. G., Lammertsma A. A. Calculation of single detector efficiencies and extension of the normalization sinogram in PET. *Phys. Med. Biol* 1997;42(6):1143-54.

(12) Reist H. W., Stadelmann O., Kleeb W. Study on the stability of the calibration and normalization in PET and the influence of drifts on the accuracy of quantification. *Eur. J. Nuc. Med* 1989;15:732-5.

(13) Holmes T. J., Snyder D. L., Ficke D. C. A statistical analysis of count normalization methods used in positron-emission tomography. *IEEE Trans. Nucl. Sci.* 1984;31(1):521-5.

(14) Hogg D., Thielemans K., Spink T. J. The derivation of detector efficiencies in PET from single photon blank scans. IEEE Nuc.Sci.Symp.Med.Im.Conf.; 2003.: p. 2206-9.

(15) Bradley R. S., Thorniley M. S. A review of attenuation correction techniques for tissue fluorescence. *J Royal Soc. Interf.* 2006;3(6):1-13.

(16) Fessler J. A. Hybrid Poisson/polynomial objective functions for tomographic image reconstruction from transmission scans. *IEEE Trans. Img. Proc.* 1995;4(10):1439-50.

(17) Lang K., Carson R. Reconstruction algorithms for emission and transmission tomography. *J. Comp. Assisted Tomo.* 1984;8(2):306-16.

(18) Xia J. Q., Georgia D. T., Joseph Y. L., Carey E. F. On the development of a Gaussian noise mdoel for scatter compensation. Proceedings of SPIE; 2007.: p. 6510M.

(19) Ollinger J. Model-based scatter correction for fully 3D PET. *Phys. Med. Biol* 1996;41(1):153-76.

References

(20) Hoffman E. J., Huang S. C., Phelps M. E., Kuhl D. E. Quantitation in positron emission computed tomography: 4 Effects of accidental coincidences. *J. Comp. Assisted Tomo.* 1981;5(3):391-400.

(21) Strigl M., Martinez M. J., Zach C., Ziegler S. I., Hahn K. Performance evaluation of the PET sub-systems of two PET/CT imagers according to NEMA standard NU 2-2001. *Z Med Phys* 2006;16(1):83-91.

(22) Kennedy A. J., Israel O., Frankel A., Bar-shalom R., Azhari H. Super-resolution in PET imaging. *IEEE Trans. Med. Img.* 2006;25:137-47.

(23) Mumcuoglu E. U., Leahy R. M., Cherry S. R., Hoffman E. Accurate geometric and physical response modeling for statistical image reconstruction in high resolution PET. *IEEE Trans. Med. Img.* 1997;3:1569-73.

(24) Fessler J. A., Rogers W. L. Spatial resolution properties of penalized-likelihood image reconstruction methods: Space-invariant tomographs. *IEEE Trans. Img. Proc.* 1996;5(9):1346-58.

(25) Liow J. S., Strother S. C., Rehm K., Gottenberg D. A. Improved resolution for PET volume imaging through three-dimensional iterative reconstruction. *J Nucl Med* 1997;10(38):1623-31.

(26) Fessler J. A., Rogers L. Uniform quadratic penalties cause non-uniform image resolution. IEEE Nucl. Sci. Symp. Med. Img. Conf.; 1994.: p. 1915-9.

(27) Mok S., Wang C., Chen J., Liu R. Peformance evaluation of the high resolution small animal PET scanner. *Biomed. Engg. Appl. Basis Comm.* 2003;15:143-9.

(28) Selivanov V. V., Picard Y., Cadorette J., Rodrigue S., Lecomte R. Detector response models for statistical iterative image reconstruction in high resolution PET. *IEEE Trans. Nucl. Sci.* 2000;47(3):1168-75.

(29) Stayman J. W., Fessler J. A. Compensation for non-uniform resolution using penalized-likelihood reconstruction in space-variant imaging systems. *IEEE Trans. Med. Img.* 2004;23(3):269-80.

(30) Munir Ahmad, Andrew Todd-Pokropek. Non-uniform resolution compensation in tomographic image reconstruction methods using median based priors. IEEE Nuc.Sci.Symp.Med.Im.Conf..: p. 4447-51.

(31) Ahmad M., Todd-pokropek A. Partial Volume Correction using Median Priors in Penalized-Likelihood Image Reconstruction Methods. IEEE Nuc. Sci. Symp. Conf.; 2006.: p. 2099-102.

(32) Reilhac A., Rousset O. G., Comtat C., Frouin V., Gregoire M. C., Evans A. C. A correction algorithm for partial volume effects in 3D PET imaging: principles and validation. IEEE Nulc.Sci.Symp.Conf.; 2000.: p. 1862-8.

(33) Meltzer C. C., Kinahan P. E., Green P. J., icholas T. E., omtat C., antwell M. N., in M. P., rice J. C. Correction of PET data for partial volume effects in human cerebral cortex by MR imaging. *J Comp. Assist. Tomo* 1999;40(12):2053-6.

(34) Labbe C., Koepp M., Ashburner J., Spinks T., Rihardson M., Duncan J., Cunningham V. Absolute PET quantification with correction for partial volume effects within cerebral structures. *Quant. Func. Br. Imag. PET* 1998;59-66.

(35) Müller-Gärtner H. W., Links J. M., Prince J. L., Bryan R. N., McVeigh E., Leal J. P., Davatzikos C., Frost J. J. Measurement of radiotracer concentration in brain gray matter using positron emission tomography: MRI-based correction for partial volume effects. *J Cereb Blood Flow Metab.* 1992;12(4):571-83.

(36) Srinivas S., Dhurairaj T., Bural B., Surtian S., Alavi A. A recovery coefficient method for partial volume correction of PET images. *J. Nucl. Med.* 2006;47:387.

(37) Frouin V., Comtat C., Reilhac A., Gregoire M. C. Correction of Partial-Volume Effect for PET Striatal Imaging: Fast Implementation and Study of Robustness. *J Nucl Med* 2002;43(12):1715-26.

(38) Ma Y., Rousset O. G., Evans C. A Generalized Methodology For Partial Volume Correction In Emission Tomography. IEEE Nulc.Sci.Symp.Conf.; 1998.

References

(39) Koole M., Van-de-Walle R., Van Laere K., Dapos M., Asseler Y., Vandenberghe S., Lemahieu I., Dierckx R. A. Studying the quantification of FBP SPECT images with a correction for partial volume effects. *IEEE Trans. Nucl. Sci.* 2002;49(1):69-73.

(40) Plewes D. B., Dean P. B. The influence of partial volume averaging on sphere detectability in computed tomography. *Phys. Med. Biol* 1981;26(5):913-9.

(41) Rousset O. G., Ma Y., Evans A. C. Correction for partial volume effects in PET. *J. Nucl. Med.* 1998;38:904-11.

(42) Aston J. A., Cunningham V. J., Asselin M. C., Hammers A., Evans A. C., Gunn R. N. Positron emission tomography partial volume correction: estimation and algorithms. *J Cereb Blood Flow Metab.* 2002;22:1019-34.

(43) Ter-Pogossian M. M., Phelps M. E., Hoffman J. A positron-emission transaxial tomograph for nuclear imaging (PET). *Radiology* 1975;114(1):89-98.

(44) Sabbatini R. M. E. The PET Scan: A New Window Into the Brain. *Brain Mind Elec. Magaz. Neuro.* 1997.

(45) Radon J. On the determination of functions from their integrals along certain manifold. *IEEE Trans. Med. Imag.* 1917;5(4):170-6.

(46) Engl H. W., Hanke M., Neubauer A. Regularization of inverse problems. Dordrecht: Kluwer Press; 1996.

(47) Baker J. R., Budinger T. F., Heusman R. H. Generalized approach to inverse problems in tomography: Image reconstruction for spatially variant systems using natural pixels". *Critical Rev. Biomed. Engg.* 1992;20:47-71.

(48) Tikhonov A. On the stability of inverse problems. *Dokl. Akad. Nauk. SSSR* 1943;39:195-200.

(49) Titarenko V., Bradley R., Martin C., Withers P. J., Titarenko S. Regularization methods for inverse problems in x-ray tomography. Proceedings of the SPIE; 2010.: p. 78040Z-10.

(50) Qi J., Leahy R. M. A Theoretical Study of the Contrast Recovery and Variance of MAP Reconstructions From PET Data. *IEEE Trans. Med. Img.* 1999;18(4):293-305.

(51) Virador P. R. G., Moses W. W., Huesman R. H. Reconstruction in PET cameras with irregular sampling and depth of interaction capability. *IEEE Trans. Nucl. Sci.* 1998;45(2):1225-30.

(52) Kao C., Pan X., Chen C. Accurate image reconstruction using DOI information and its implications for the development of compact PET systems. *IEEE Trans. Nucl. Sci.* 2000;47(4-2):1551-60.

(53) Siddon R. L. Fast calculation of the exact radiological path for a three-dimensional CT array. *Med. Phys.* 1985;12(2):252-5.

(54) Shin-Chung L. B. Strip and line path integrals with a square pixel matrix: a unified theory for computational CT projections. *IEEE Trans. Med. Img.* 1988;4:355-63.

(55) Moehrs S., Defrise M., Belcari N., uerra A. D., artoli A., abbri S., anetti G. Multi-ray-based system matrix generation for 3D PET reconstruction. *Phys. Med. Biol* 2008;53(23):6925-45.

(56) Herman G. T., Meyer L. B. Algebraic reconstruction techniques can be made computationally efficient [positron emission tomography application]. *IEEE Trans. Med. Img.* 1993;12(3):600-9.

(57) Zhao H., Reader J. A. Fast projection algorithm for voxel arrays with object dependent boundaries. IEEE Nuc.Sci.Symp.Conf.; 2002.: p. 1490-4.

(58) Christiaens M., Sutter B. D., Bosschere K. D., Campenhout J. V., Lemahieu I. A fast, cache-aware algorithm for the calculation of radiological paths exploiting subword parallelism. *J. Sys. Arch.* 1999;45:781-90.

References

(59) Jacob P., Sundermann E., Sutter B. D., Chritiaens M., Lemhein I. A fast algorithm to calculate the exact radiological path through a pixel or voxel space. *J. Comp. Inform. Tech.* 1998;6:89-94.

(60) Frese T., Rouze N. C., Bouman C. A., Sauer K., Hutchins G. D. Quantitative comparison of FBP, EM, and Bayesian reconstruction algorithms for the IndyPET scanner. *IEEE Trans. Med. Img.* 2003;22(2):258-76.

(61) Panin V. Y., Kehren F., Rothfuss H., Hu D., Michel C., Casey M. E. PET reconstruction with system matrix derived from point source measurements. IEEE Nuc. Sci. Symp. Med. Img. Conf.; 2004 Oct 16.: p. 2483-7.

(62) Lage E., Vaquero J. J., Sisniega A., Espana S., Tapias G., Abella M., Rodriguez-Ruano A., Ortuno J. E., Udias A., Desco M. Design and performance evaluation of a coplanar multimodality scanner for rodent imaging. *Phys. Med. Biol* 2009;54(18):5427-41.

(63) Kontaxakis G., Strauss L. G., Thireou T., Ledesma-Carbayo M. J., Santos A., Pavlopoulos S. A., Dimitrakopoulou-Strauss A. Iterative image reconstruction for clinical PET using ordered subsets, median root prior, and a web-based interface. *Mol Imaging Biol* 2002;4(3):219-31.

(64) Johnson C. A., Yuchen Y., Carson R. E., Martino R. L., Daube-Witherspoon M. E. A system for the 3D reconstruction of retracted-septa PET data using the EM algorithm. IEEE Nuc. Sci. Symp. Med. Img. Conf.; 2005 Oct 30.: p. 1325-9.

(65) Qi J., Leahy R. M., Cherry S. R., Chatziioannou A., Farquhar T. H. High-resolution 3D Bayesian image reconstruction using the microPET small-animal scanner. *Phys. Med. Biol* 1998;43(4):1001-13.

(66) Bertero M., Lantari H., Zanni L. Iterative image reconstruction: a point of view. InterdisciplinaryWorkshop on Mathematical Methods in Biomedical Imaging and Intensity-Modulated RadiationTherapy (IMRT); 2007.: p. 1-25.

(67) Bertero M., Poggio T. A., Torre V. Ill-posed problems in early vision. *Proceedings of the IEEE* 1988;76(8):869-89.

(68) Engl H. W., Kugler P. Nonlinear Inverse Problems: Theoretical Aspects and Some Industrial Applications. 6 ed. Springer Berlin Heidelberg; 2005.

(69) Tarantola A. Inverse problems theory and methods for Model Parameter Estimation. Paris, France: SIAM; 2004.

(70) Hadamard J. Lectures on Cauchy's problem in linear partial differential equations. New Haven Yale University Press; 1923.

(71) Tikhonov A., Arsenun V. Solution of Ill-Posed Problems. Washington DC: Winston and Sons; 1977.

(72) Dai W. Approach to Solve Ill-posed Inverse Problem in Image Reconstruction from Projections. 2009.

(73) Rakha M. A. On the Moore-Penrose generalized inverse matrix. *Appl. Math. Comp.* 2004;158(1):185-200.

(74) Tikhonov A. Solution of incorrectly formulated problems and the regularization method. *Soviet Math. Doklady* 1963;4:1035-8.

(75) Tikhonov A., Arsenin V. Solutions of ill-posed problems. New York: John Willy & Sons; 1977.

(76) Mumcuoglu E. U., Leahy R. M., Cherry S. R. Bayesian reconstruction of PET images: methodology and performance analysis. *Phys. Med. Biol* 1996;41(9):1777-807.

(77) Geman S., McClure D. Bayesian image analysis: An application to single photon emission tomography. Proc.Statistical Computation Section, Amer.Statistical Assoc.; 1985.: p. 12-8.

References

(78) Tsui B. M. W., Frey E. C. Analytic Image Reconstruction Methods in Emission Computed Tomography. In: Zaidi H., editor. *Quantitative Analysis in Nuclear Medicine Imaging*. 2006 Springer US.

(79) Herman G. T. A note on exact image reconstruction from a limited number of projections. *J Vis. Comm. Img Repres.* 2009;20(1):65-7.

(80) Novikov R. An inversion formula for the attenuated x-ray transformation. *Ark. Mat.* 2000.

(81) Tretiak O., Metz C. The exponential Radon transform. *SIAM J. App. Math.* 1980;39(2):341.

(82) Natterer F. Inversion of the attenuated Radon transform. *Inv. Prob.* 2001;17:113-9.

(83) Shneiberg L. Some inversion formulas in the single photon emission computed tomography. *Applic. Analy.* 1994;53(3-4):221-31.

(84) Zeng G. L., Gullberg G. T. Iterative and analytical reconstruction algorithms for varying-focal-length cone-beam projections. *Phys. Med. Biol* 1998;43(4):811-21.

(85) Kak A. C., Slaney M. Prinicples of Computerized Tomographic Imaging. IEEE Press; 1979.

(86) Mersereau R. M. Direct fourier transform techniques in 3-D image reconstruction. *Comp Biol Med* 1976;6(4):247-IN4.

(87) Hewei, G., Li, Z., Yuxiang, X., Chen, Z., and Jianping, C. An Improved Form of Linogram Algorithm for Image Reconstruction. *Nuclear Science, IEEE Transactions on* 2008;55(1):552-559.

(88) Shepp L. A., Logan B. F. The Fourier reconstruction of a head section. *IEEE Trans. Nucl. Sci.* 1974;21:21-43.

(89) Tianfang L., Jiangsheng Y., Junhai W., Zhengrong L. Inversion of the attenuated Radon transform for non-parallel geometries. IEEE Nuc. Sci. Symp. Med. Img. Conf.; 2004 Oct 16.: p. 2525-9.

(90) Wang C. X., Snyder W. E., Bilbro G., Santago P. Performance evaluation of filtered backprojection reconstruction and iterative reconstruction methods for PET images. *Comp Biol Med* 1998;28(1):13-25.

(91) Shepp L. A., Verdi Y. Maximum Likelihood reconstruction for emission tomography. *IEEE Trans. Med. Img.* 1982;1(2):113-22.

(92) Censor Y., Eggermont P. B., Gordon D. Strong underrefaxation in Kaczmarz's method far inconsistent systems. *Numer. Meth.* 1983;41:83-92.

(93) Alessio A. M., Kinnahan P., Lewellem T. Improved quantitaion of PET/CT image reconstruction with system modeling and anatomical priors. Proceedings of SPIE; 2005.: p. 695-703.

(94) Alessio A. M., Kinahan P. E., Lewellen T. K. Modeling and incorporation of system response functions in 3-D whole body PET. *IEEE Trans. Med. Img.* 2006;25(7):828-37.

(95) Snyder D. L., Miller M. I. The use of sieves to stabilize images produced with the EM algorithm for emission tomography. *IEEE Trans. Nucl. Sci.* 1985;32(5):3864-71.

(96) Fessler J. A. Penalized weighted least-squares image reconstruction for positron emission tomography. *IEEE Trans. Med. Img.* 1994;13(2):290-300.

(97) Fessler JA. Iterative methods for image reconstruction. *EECS* Department, the university of Michigan; 2006.

(98) Ahn A. Convergent Algorithms for Statistical Image Reconstruction in Emission Tomography [PhD]. USA: The University of Michigen; 2004.

(99) Gordon R., Bender R., Herman G. Algebraic reconstruction techniques for three-dimensional electron microscopy and x-ray photohgraphy. *J. Theor. Biol.* 1970;29:471-81.

References

(100) Fessler J. A., Booth S. D. Conjugate-gradient preconditioning methods for shift-variant PET image reconstruction. *IEEE Trans. Img. Proc.* 1999;8(5):688-99.

(101) Chinn G., Huang S. C. A fast preconditioned conjugate gradient algorithm for regularized WLS reconstruction for PET. IEEE Nuc. Sci. Symp. Med. Img. Conf.; 1995.: p. 1297-301.

(102) Snyder D. L., Miller I., Thomas J., Politte G. Noise and edge artifacts in maximum-likelihood reconstructions for emission tomography. *IEEE Trans. Med. Img.* 1987;6(3):228-38.

(103) Glatting G., Wuchenauer M., Reske S. N. Iterative reconstruction for attenuation correction in positron emission tomography: Maximum likelihood for transmission and blank scan. *Med. Phys.* 1999;26(9):1838-42.

(104) Veklerov E., Llacer J. Stopping rule for the MLE algorithm based on statistical hypothesis testing. *IEEE Trans. Med. Img.* 1987;6(4):313-9.

(105) Green P. J. On the use of the EM algorithm for penalized likelihood estimation. *J. Roy. Statist. Soc. , B* 1990;52(3):443-52.

(106) Barrett H., Wilson W., Tsui B. M. W. Noise properties of the EM algorithm: I. Theory. *Phys. Med. Biol* 1994;39(5):833-46.

(107) Alenius S. On noise reduction in iterative image reconstruction algorithms for emission tomography: Median root prior [PhD]. Italy: Tampere University of Technolog; 1999.

(108) Daniel F. Y., Fessler J. A. Edge-Preserving Tomographic Reconstruction with Nonlocal Regularization. *IEEE Trans. Med. Img.* 2002;21(2):159-73.

(109) Idier J., Muhammad-Djafari A., Demoment G., Demoment N. G. Regularization methods and inverse problems: An information theory standpoint. Intern. Conf. on Inverse Problems in Eng.; 1996. Le Croisic.

(110) Ing-Tsung Hsiao, A.Rangarajan, and G.Gindi. A new convex edge-preserving median prior with applications to tomography. *IEEE Trans. Med. Imag.* 2003;22(5):580-585.

(111) Hebert T. J., Leahy R. M. Statistic-based MAP image reconstruction from Poisson data using Gibbs priors. *IEEE Trans. Sig. Proc.* 1992;40(9):2290-303.

(112) Tang J., Nett B. E., Chen G. H. Performance comparison between total variation (TV)-based compressed sensing and statistical iterative reconstruction algorithms. *Phys. Med. Biol* 2009;54(19):5781-804.

(113) Sidky E. Y., Pan X. Image reconstruction in circular cone-beam computed tomography by constrained, total-variation minimization. *Phys. Med. Biol* 2008;53(7):4777-807.

(114) Rudin L. I., Osher S., Fatemi E. Nonlinear total variation based noise removal algorithms. *Physica D: Nonlinear Phenomena* 1992;60(1â€"4):259-68.

(115) Donoho D. L. Compressed sensing. *IEEE Trans Info Theor.* 2006;52(4):1289-306.

(116) Persson M., Bone D., Elmqvist H. Total variation norm for three-dimensional iterative reconstruction in limited view angle tomography. *Phys. Med. Biol* 2001;46(3):853-66.

(117) Bouman C., Sauer K. A generalized Gaussian image model for edge-preserving MAP estimation. *IEEE Trans. Img. Proc.* 1993;2(3):296-310.

(118) Yavuz M., Fessler J. A. Penalized-likelihood estimators and noise analysis for randoms pre-corrected PET transmission scans. *IEEE Trans. Med. Img.* 1999;18(8):665-74.

(119) Bouman C., Sauer K. A unified approach to statistical tomography using coordinate descent optimization. *IEEE Trans. Img. Proc.* 1996;5(3):480-92.

(120) Lange K. Convergence of EM image reconstruction algorithms with Gibbs smoothing. _IEEE Trans. Med. Img._ 1991;9(4):439-46.

(121) Geman S., Geman D. Stochastic relaxation, Gibbs distributions, and the Bayesian restoration of images. _IEEE Trans Patt Analy Mach Intel._ 1984;PAMI-6:721-41.

(122) Leahy R. M., Qi. J. Statistical approaches in quantitative positron emissions tomography. _Stat. Comp._ 2000;10(2):147-65.

(123) Kenneth M Henson. Bayesian and related methods in image reconstruction from incomplete data. Orlando: Academic; 1987.

(124) Marroquin J., Mitter J., Poggo T. Probabilistic solution of ill-posed problems in computational vision. _J. Amer. Stat. Assoc._ 1987;82(397):76-89.

(125) Jeffs B. D., Gardiner A. H. Markov random field image prior models for map reconstruction of magnetoencephalogram images. Signals, Systems & Computers, 1998. Conference Record of the Thirty-Second Asilomar Conference on; 1998.: p. 314-8.

(126) Nunez J., Llacer J. A fast Bayesian reconstruction algorithm for emission tomography with entropy prior converging to feasible images. _IEEE Trans. Med. Img._ 1990;9(2):159-71.

(127) Huber P. J. Robust statistics. New York: _Wiley_; 1981.

(128) Alenius S., Ruotsalainen U., Astola J. Using local median as the location of the prior distribution in iterative emission tomography image reconstruction. _IEEE Trans. Nucl. Sci._ 1998;45(6):3097-104.

(129) Stayman J. A., Fessler J. A. Regularization for uniform spatial resolution properties in penalized-likelihood image reconstruction. _IEEE Trans. Med. Img._ 2000;19(6):601-15.

(130) Usman M., Hero A. O., Fessler J. A. Uniform CR bound: implementation issues and applications. IEEE Nuc. Sci. Symp. Med. Img. Conf.; 2005 Oct 30.: p. 1443-7.

(131) Wilson D. W., Tsui B. M. W., Barrett H. H. Noise properties of the EM algorithm: II. Monte Carlo simulations. _Phys. Med. Biol_ 1994;39(72):847-72.

(132) Ahn S., Leahy R. M. Analysis of resolution and noise properties of non-quadratically regularized image reconstruction methods for PET. _IEEE Trans. Med. Img._ 2008;27(3):413-24.

(133) Usman M., Hero A. O., Fessler J. A., Rogers W. L. Bias-variance tradeoffs analysis using uniform CR bound for image reconstruction. IEEE Nulc.Sci.Symp.Conf.Rec.; 1994.

(134) Delaney A. H., Bresler Y. Globally convergent edge-preserving regularized reconstruction: an application to limited-angle tomography. _IEEE Trans. Img. Proc._ 1998;7(2):204-21.

(135) Charbonnier P., Blanc-Feraud L., Aubert G., Barlaud M. Deterministic edge-preserving regularization in computed imaging. _IEEE Trans. Img. Proc._ 1997;6(2).

(136) Matej S., Fessler J. A., Kazantsev I. G. Iterative tomographic image reconstruction using Fourier-based forward and back-projectors. _IEEE Trans. Med. Imag._ 2004;23(4):401-12.

(137) Ing-Tsung Hsiao, P.Khurd, M.Rangarajan, and G.Gindi. An overview of fast convergent ordered-subsets reconstruction methods for emission tomography based on the incremental EM algorithm . _Nucl. Inst. & meth. Phys. Rese. A_ 2006;569:429-433.

(138) Stayman J. W., Fessler J. A. Penalty design for uniform spatial resolution in 3D Penalized-Likelihood image reconstruction. Intern.Meeting Fully 3D Img.Recon.Radio.Nucl.Med.; 1999.: p. 361-4.

(139) Mustafovic S., Thielemans K. Additive and multiplicative versions of the maximum a posteriori algorithm with median root prior. IEEE Nuc.Sci.Symp.Med.Img.Conf..: p. 1783-5.

References

(140) Bettinardi V., Pagani E., Gilardi E. C., Alenius S., Thielemans K., Teras M., Fazio F. Implementation and evaluation of a 3D one-step late reconstruction algorithm for 3D positron emission tomography brain studies using median root prior. *Eur. J. Nucl. Med. Mol. Imag.* 2002;29:7-18.

(141) Buvat I., Soret M., Hapdey S., Riddeil C., Benali H., Di-Paola R. Respective importance of scatter, attenuation, collimator response and partial volume effect corrections for accurate quantification in ^{123}I dopamine receptor imaging. IEEE Nuc. Sci. Symp. Conf.; 2000.: p. 13-5-13/19.

(142) Young D., Tsui B. M. W., Frey E. C. Model-based compensation for quantitative 123I brain SPECT imaging. *Phys. Med. Biol* 2006;51:1269-82.

(143) Fazio F., Perani D. Importance of partial volume correction in brain PET studies. *J Nucl Med* 2000;41(11):1849-`850.

(144) Kinahan P. E., Karp J. S. Figures of merit for comparing reconstruction algorithms with a volume-imaging PET scanner. *Phys. Med. Biol* 1994;39:631-42.

(145) Rosenthal M. S., Cullom J., Hawkins W., Moore S. C., Tsui B. M. W., Yester M. Quantitative SPECT Imaging: A Review and Recommendations by the Focus Committee of the Society of Nuclear Medicine Computer and Instrumentation Council. *J Nucl Med* 2009;36(8):1489-513.

(146) Zhong Q. The convolution back projection algorithm based on windows function. Granular Computing, 2005 IEEE International Conference on; 2005.: p. 626-9.

(147) Hebert T. J. Statistical stopping criteria for iterative maximum likelihood reconstruction of emission images. *Phys. Med. Biol* 1990;35(9):1221-32.

(148) Nuyts J., Fessler J. A. A penalized-likelihood image reconstruction method for emission tomography, compared to postsmoothed maximum-likelihood with matched spatial resolution. *IEEE Trans. Med. Img.* 2003;22:1042-52.

(149) Babacan S. D., Molina R., Katsaggelos A. K. Total variation super resolution using a variational approach. Image Processing, 2008. ICIP 2008. 15th IEEE International Conference on; 2008.: p. 641-4.

(150) Yuying L., Santosa F. A computational algorithm for minimizing total variation in image restoration. *IEEE Trans. Img. Proc.* 1996;5(6):987-95.

(151) Bruyant P. P. Analytic and iterative reconstruction algorithms in SPECT. *J Nucl Med* 2002;43(10):1343-58.

(152) Leaf-Lensmire K. J., Stearns C. W., Colsher J. G. PET transmission scanning with a variable speed orbiting rod source. IEEE Nuc.Sci.Symp.Med.Im.Conf.; 1992.: p. 979-81.

(153) Phelps M. E., Hoffman E. J., Mullani A., Ter-Pogossian M. Application of annihilation coincidence detection to transaxial reconstruction tomography. *J Nucl Med* 1975;16(3):210-24.

(154) Rahmim A. Statistical List-mode Image Reconstruction and Motion Compensation Techniques in High-Resolution Positron Emission Tomography (PET) [PhD]. Canada: The University of British Coloumbia; 2005.

(155) Reader A. J., Erlandson K., Flower A., Ott J. Fast Accurate Iterative Reconstruction for Low-Statistics Positron Volume Imaging. *Phys. Med. Biol* 1998;43:166-9.

(156) Macovski A. Medical imaging systems. New Jersey: *Prentice-Hall*; 1983.

(157) Yair C., Zenios S. A. Parallel Optimization: Theory, Algorithms, and Applications. Oxford University Press; 1998.

(158) Hudson H. M., Larkin S. Accelerated image reconstruction using ordered subsets of porjection data. *IEEE Trans. Med. Img.* 1994;13(4):601-9.

References

(159) Rahmim A., Ruth T. J., Sossi V. Study of a convergent subsetized list-mode EM reconstruction algorithm. IEEE Nulc.Sci.Symp.Conf.; 2004.: p. 3978-82.

(160) Ing-Tsung Hsiao, A.Rangarajan, P.Khurd, and G.Gindi. An accelerated convergent ordered subsets algorithm for emission tomography. *Phys. Med. Biol* 2004;49:2145-2156.

(161) Kaufman L. Implementing and accelerating the EM algorithm for Positron Emission Tomography. *IEEE Trans. Nucl. Med* 1987;MI-6:37-51.

(162) Lang K., Hunter.D.R., Yang I. Optimization using surrogate functions. *J. Compu. Graph. Stat.* 2000;2:175-98.

(163) Fessler J. A., Hero A. O. Space-alternating generalized Expectation-Maximization algorithm. *IEEE Trans Sign. Proc* 1994;42(10):2664-77.

(164) Lang K., Carson R. EM reconstruction algorithms for emissionn and transmission tomography. *J Comp. Assist. Tomo* 1984;8:306-16.

(165) Alenius S., Ruotsalainen L. Generalization of median root prior reconstruction. *IEEE Trans. Med. Img.* 2002;21(11):1413-20.

(166) Fessler J. A. Mean and variance of implicitly defined biased estimators (such as penalized maximum likelihood): Applications to tomography. *IEEE Trans. Img. Proc.* 1996;5(3):493-506.

(167) Nuyts J. On Estimating the Variance of Smoothed MLEM Images. IEEE Nuc.Sci.Symp.Conf.; 2001.: p. 1414-8.

(168) Fessler J. A. Approximate variance images for penalized-likelihood image reconstruction. IEEE Nuc. Sci. Symp. Med. Img. Conf.; 1997.

(169) Soret M., Bacharach S. L., Buvat I. Partial-volume effect in PET tumor imaging. *J. Nucl. Med.* 2007;48(6):932-45.

(170) Baete K., Nuyts J., Van K. L. Evaluation of anatomy basedreconstruction for partial volume correction in brain FDG PET. *Neuro.* 2004;23:305-17.

(171) Links J. M., Zupbieta J. K., Meltzer C. C., Stump M. J., Frost J. J. Influence of spatially heterogeneous background activity on "hot object" quantitation in brain emission computed tomography. *J Comp. Assist. Tomo* 1996;20(4):680-7.

(172) Meltzer C. C., Kinahan P. E., Greer P. J., Thomas N. E., Comtat C., Cantwell M. N., Lin M. P., Price J. C. Comparative evaluation of MR-Based Partial-Volume Correction Schemes for PET. *J. Nucl. Med.* 1999;40(12):2053-6.

(173) Wells K., Chiverton K., Partridge M., Barry M., Kadhem M., Ott B. The partial volume effect in PET/SPECT and Benford's law. IEEE Nulc.Sci.Symp.Conf.; 2005.: p. 5 pp.

(174) Tohka U., Reilhac A. Deconvolution-based partial volume correction in Raclopride-PET and Monte Carlo comparison to MR-based method. *Neuro.* 2007;39(4):038.

(175) Byrne C. L. Likelihood Maximization for *List-Mode* Emission Tomographic Image Reconstruction. *IEEE Trans. Med. Img.* 2001;20(10):1084-92.

(176) Barrett H. H., White T., Parra L. C. List-mode likelihood. *J Opt. Soc. Amer.* 1997;14:2914-23.

(177) Bouwens L., de Walle V., Gifford H., King M. A., Lemahieu I., Dierckx A. LMIRA: list-mode iterative reconstruction algorithm for SPECT. *IEEE Trans. Nucl. Sci.* 2000;4:1364-70.

(178) Parra L., Barrett H. H. List-mode likelihood: EM algorithm and image quality estimation demonstrated on 2-D PET. *IEEE Trans. Med. Img.* 1998;17(2):228-35.

(179) Bouwens L., de Walle V., Gifford H., King M. A., Lemahieu I., Dierckx A. Resolution recovery for list mode reconstruction in SPECT. *Phys. Med. Biol* 2001;46(8):2239-53.

References

(180) Virador P. R., Moses W. W., Heusman R. H., Qi J. 3D reconstruction in PET cameras with irregular sampling and depth of interaction. *IEEE Trans. Nucl. Sci.* 2001;NS-48:1524-9.

(181) Rahmim A., Lenox M., Reader A. J., Michel C., Burbar Z., Ruth T. J., Sossi V. Statistical list-mode image reconstruction for the high resolution research tomograph. *Phys. Med. Biol* 2004;49:4239-58.

(182) Rahmim A., Dinelle K., Cheng J. C., Shilov M. A., Segars W. P., Rousset O. G., Tsui B. M. W., Wong D. F., Sossi V. Accurate event driven motion compensation incSorporating all detected events. IEEE Nulc.Sci.Symp.Conf.; 2006.: p. 3331-8.

(183) Snyder D. L., Politte D. G. Image-Reconstruction from List-Mode Data in an Emission Tomography System Having Time-of-Flight Measurements. *IEEE Trans. Nucl. Sci.* 1983;30(3):1843-9.

(184) Ahmad M., Todd-pokropek A. Evaluation of resolution properties of median priors in list-mode reconstruction methods for PET. IEEE Nuc. Sci. Symp. Med. Img. Conf.; 2009 Oct 24.: p. 2853-6.

(185) Hiroyuki Kudo, H. Analytical image r econstruction methods for medical tomography - recent advances and a new unique result -. *Math. Aspects Imag. Proc. Comp. Vis.* 2006;1-2.

(186) Nuyts J., K.Baete K., Baque D., Dupont P. Comparison between MAP and post-processed ML for image reconstruction in emission tomography when anatomical knowedge is available. IEEE Nulc.Sci.Symp.Conf.; 2003.: p. 2007-11.

(187) Mondal P. P., Rajan K. Image reconstruction by conditional entropy maximisation for PET system. *IEE Proc. Vis. Img. Sig, Proc.* 2004;151(5):345-52.

(188) Maria A. Introduction to modeling and simulation. Proceedings of the Winter Simulation Conference; 1997.: p. 7-13.

(189) Banks L., Carson J. S., Nelson B. L. Discrete-Event System Simulation. IInd ed. Prentice Hall; 1996.

(190) Calvetti D., Morigi S., Reichel L., Sgallari F. Tikhonov regularization and the L-curve for large discrete ill-posed problems. *J Comput. Appl. Math.* 2000;123(12):423-46.

(191) Kinahan P. E., Defrise M., Clackdoyle R. Chapter 20 - Analytic Image Reconstruction Methods. San Diego: Academic Press; 2004.

(192) Townsend D. W. Positron Emission Tomography/Computed Tomography. *Sem Nucl Med* 2008;38(3):152-66.

(193) Lewitt R. M. Alternatives to voxels for image representation in iterative reconstruction algorithms. *Phys. Med. Biol* 1992;37(3):705-16.

(194) Devaney A. J. A filtered backpropagation algorithm for diffraction tomography. *Ultras. Img.* 1982;4(4):336-50.

(195) Quanzheng L., Asma E., Jinyi Q., Bading J. R., Leahy R. M. Accurate estimation of the Fisher information matrix for the PET image reconstruction problem. IEEE Nuc. Sci. Symp. Med. Img. Conf.; 2003 Oct 19.: p. 2012-6.

(196) Seo Y., Mari C., Hasegawa B. H. Technological Development and Advances in Single-Photon Emission Computed Tomography/Computed Tomography. *Sem Nucl Med* 2008;38(3):177-98.

(197) Wang W., Gindi G. Noise analysis of MAP-EM algorithms for emission tomography. *Phys. Med. Biol* 1997;42(11):2215-32.

(198) Yong, D., Tsui, B. M. W., and Frey, E. C. Partial volume effect compensation for quantitative brain SPECT imaging. *Medical Imaging, IEEE Transactions on* 2005;24(8):969-976.

(199) Rahmim A., Lenox M., Reader A. J., Michel C., Burbar Z., Ruth T. J., Sossi V. Weighted Iterative List-Mode Reconstruction for the High Resolution Research Tomograph. Intern.Meeting Fully 3D Img.Recon.Radio.Nucl.Med.; 2003.

References

(200)   Tang J., Zhang L., Chen Z., Xing Y., Cheng J. A BPF-type algorithm for CT with a curved PI detector. *Phys. Med. Biol* 2006;51(16):N287-N293.

(201)   Silverman B. W., Jennison C., Stander J., Brown T. C. The specification of edge penalties for regular and irregular pixel images. *IEEE Trans Patt Analy Mach Intel.* 1990;12(10):1017-24.